Annex IV: Modes of Variability

Coordinating Lead Authors:
Christophe Cassou (France), Annalisa Cherchi (Italy), Yu Kosaka (Japan)

Lead Authors:
Susanna Corti (Italy), Francois Engelbrecht (South Africa), June-Yi Lee (Republic of Korea), Amanda Maycock (United Kingdom), Shayne McGregor (Australia), Olaf Morgenstern (New Zealand/Germany), Hyacinth C. Nnamchi (Nigeria, Germany/Nigeria), Juan A. Rivera (Argentina), Blair Trewin (Australia)

Contributing Author:
Adam S. Phillips (United States of America)

This Annex should be cited as:
IPCC, 2021: Annex IV: Modes of Variability [Cassou, C., A. Cherchi, Y. Kosaka (eds.)]. In: *Climate Change 2021: The Physical Science Basis. Contribution of Working Group I to the Sixth Assessment Report of the Intergovernmental Panel on Climate Change* [Masson-Delmotte, V., P. Zhai, A. Pirani, S. L. Connors, C. Péan, S. Berger, N. Caud, Y. Chen, L. Goldfarb, M. I. Gomis, M. Huang, K. Leitzell, E. Lonnoy, J.B.R. Matthews, T. K. Maycock, T. Waterfield, O. Yelekçi, R. Yu and B. Zhou (eds.)]. Cambridge University Press. In Press.

Date: August 2021

This document is subject to copy-editing, corrigenda and trickle backs.

ACCEPTED VERSION SUBJECT TO FINAL EDITING

Table of Contents

AIV.1 Introduction 4
AIV.2 The main modes of climate variability assessed in AR6 5
AIV.2.1 North Atlantic Oscillation and Northern Annular Mode 5
AIV.2.1.1 Definition of the mode 5
AIV.2.1.2 Teleconnections and regional influence 7
AIV.2.1.3 Available proxy-based reconstruction 8
AIV.2.2 Southern Annular Mode 9
AIV.2.2.1 Definition of the mode 9
AIV.2.2.2 Teleconnections and regional influence 10
AIV.2.2.3 Available proxy-based reconstruction 11
AIV.2.3 El Niño-Southern Oscillation 11
AIV.2.3.1 Definition of the mode 11
AIV.2.3.2 Teleconnections and regional influence 13
AIV.2.3.3 Available proxy-based reconstruction 14
AIV.2.4 Indian Ocean Basin and Dipole Modes 14
AIV.2.4.1 Definition of the mode 14
AIV.2.4.2 Teleconnections and regional influence 16
AIV.2.4.3 Available proxy-based reconstruction 17
AIV.2.5 Atlantic Meridional and Zonal Modes 17
AIV.2.5.1 Definition of the mode 17
AIV.2.5.2 Teleconnections and regional influence 19
AIV.2.5.3 Available proxy-based reconstruction 20
AIV.2.6 Pacific Decadal Variability 20
AIV.2.6.1 Definition of the mode 20
AIV.2.6.2 Teleconnections and regional influence 22
AIV.2.6.3 Available proxy-based reconstruction 23
AIV.2.7 Atlantic Multidecadal Variability 23
AIV.2.7.1 Definition of the mode 23
AIV.2.7.2 Teleconnections and regional influence 25
AIV.2.7.3 Available proxy-based reconstruction 26

ACCEPTED VERSION SUBJECT TO FINAL EDITING

AIV.2.8 Madden-Julian Oscillation 26
AIV.2.8.1 Definition of the mode 26
AIV.2.8.2 Teleconnections and regional influence 28
References 29
Figures 50

ACCEPTED VERSION SUBJECT TO FINAL EDITING

AIV.1 Introduction

This Annex describes the fundamental features of the main modes of large-scale climate variability assessed across chapters in the AR6 WGI report. Modes are defined as recurrent space-time structures of variability of the climate system with intrinsic spatial patterns, seasonality and timescales. They can arise through the dynamical characteristics of the atmospheric circulation but also through coupling between the ocean and the atmosphere, with some interactions with land surfaces and sea ice. The variability of the climate system at ocean- or continental-basin scales, and in particular on seasonal-to-multidecadal timescales, can be described to a large extent by the occurrence and often combination of several modes of climate variability which lead to local impacts and remote responses through teleconnection processes on top of externally forced trends. More precisely, the concept of "teleconnection" refers to the ability of modes of variability to relate climate in remote regions through associated atmospheric or oceanic pathways. Regional climate variations are thus the complex outcome of local physical processes, such as thermodynamical and land-atmosphere feedback processes, and non-local large-scale phenomena.

Historically, modes have been identified based on evidence of correlations between regional climate variations at widely separated, mostly geographically fixed spatial locations. One of the oldest known space-time structured patterns of variability is the North Atlantic Oscillation (NAO, Section AIV.2.1), with some early description from seafaring activities available since several centuries ago (Stephenson et al., 2003). Similarly, empirical, albeit remarkably precise, documentation of trans-Pacific coherent variability in atmospheric and oceanic conditions can be traced back to the 19th century for the El Niño-Southern Oscillation (ENSO, Section AIV.2.3). The Southern Oscillation was named in 1924 and the first use of the name 'El Niño' to describe a climatic phenomenon appeared in South America in 1893 (see for instance Philander, 1983 for ENSO history). Since then, the increased spatial coverage of observations and the measurement of new climatic parameters have improved significantly. These advancements, along with the development of new theoretical background and statistical methods for combining different sources of information, have allowed substantial improvements in our understanding of the characteristic spatial scale of the coherent structures of variability as well as of the characteristic temporal expression of the modes.

There are several ways to document and describe the modes of climate variability based on more or less sophisticated statistical techniques and dynamical nature, interpretation and understanding of the variability (i.e., Feldstein and Franzke, 2017; Hannachi et al., 2017; Franzke et al., 2020; Ghil and Lucarini, 2020). The simplest method to evaluate the temporal evolution of a spatially coherent phenomenon is to take one or more spatial averages of a climate variable such as sea surface temperature (SST) or sea level pressure (SLP), as examples, within a latitude-longitude box. Another classical technique relies on principal component analysis (PCA), also known as empirical orthogonal function (EOF) analysis, to extract the patterns in the chosen climate variable with maximal spatial covariance. The method also extracts an associated climate index timeseries, i.e. principal component (PC), describing the temporal evolution tied to the spatial pattern. PCA/EOF is widely used with gridded datasets and model outputs. Correlation or regression maps between the climate index timeseries and other space-time variables, such as precipitation, temperature or wind, are then calculated to quantify the teleconnection patterns. Altogether, beyond their physical relevance, modes of climate variability and their teleconnection patterns provide a simplified representation of climate variation affecting weather, from regional (i.e. oceanic or continental scale) to worldwide scales (i.e. for some specific phenomena like ENSO), having important impacts on human activities and ecosystems. Modes are often associated with climatic impact-drivers (CIDs, as defined in Chapter 12, Section 12.1) including droughts, heavy rains, storms, heat waves and cold spells, affecting agriculture, water resources, availability and consumption of energy, fire risks, etc.

Many modes of variability are driven by internal climate processes and are a critical potential source of climate predictability on sub-seasonal to decadal timescales. It is essential to understand the physical processes behind the past evolution of the modes of climate variability in order to assess, with confidence, their future changes. External forcing may affect their temporal (occurrence, variance, seasonality, persistence etc.) or spatial properties and associated teleconnections.

Previous IPCC reports have described the observed and modelled behaviour of a large number of modes of

ACCEPTED VERSION SUBJECT TO FINAL EDITING

variability over the instrumental period and in a paleoclimate context. The projected evolution of those modes has been also documented based on future climate scenarios. In AR5, large-scale modes of variability and teleconnections were assessed in depth in Chapter 14, setting the physical basis of future regional climate changes contingent on global mean temperature increase. Modes were defined through so-called "indices of climate variability" in AR5 Chapter 2, dedicated to observed atmospheric and surface changes. Two boxes (AR5 Box 2.5 and AR5 Box 14.1) introduced the main concepts. AR4 had a similar structure, with a specific section on modes in the chapter dedicated to the observations (Chapter 3). In AR6, a different perspective has been adopted, as the modes are discussed in various chapters and assessed with respect to the specific objectives of each of them. Space-time past changes of the modes using proxy records and instrumental data are assessed in Chapter 2. Human influence on modes is assessed in Chapter 3 over the instrumental period, while their future changes are addressed in Chapter 4. Their influence at regional scale through large-scale teleconnection is assessed in Chapters10, 11, 12 and Atlas, while the contribution of the modes in past and future hydrological changes and related uncertainties are assessed in Chapter 8. Chapter 9 focuses on oceanic expression of the modes. The aim of this Annex is to set a common background for the assessment of the modes of climate variability and related regional climate anomalies for all the AR6 WG1 Chapters, and to provide this information for the readers of the report. In doing so, the Annex provides a more accessible summary of the main modes of variability allowing a more coherent assessment of this important aspect of the climate system.

The Annex summarizes the fundamental features of spatial structure, seasonality and teleconnections for a selection of modes of climate variability corresponding to those addressed in the report, namely: the NAO and Northern Annular Mode, the Southern Annular Mode, ENSO, the Indian Ocean Basin and Dipole Modes, the Atlantic Meridional and Zonal Modes, the Pacific Decadal Variability, the Atlantic Multidecadal Variability, and the Madden-Julian Oscillation. For each mode, the description follows a common structure, starting with a short definition of the mode (based on simple box-averaged indices and EOF) and related key physical mechanisms, then a description of the associated teleconnections (based on regression techniques), and when relevant, finishes with a short summary of paleoclimate reconstruction of the mode based on proxy-based records. An illustrative figure including patterns and timeseries is also provided for each mode.

AIV.2 The main modes of climate variability assessed in AR6

AIV.2.1 North Atlantic Oscillation and Northern Annular Mode

AIV.2.1.1 Definition of the mode

The North Atlantic Oscillation (NAO) is the leading mode of large-scale atmospheric variability in the North Atlantic basin. It is characterized by alternating (seesaw) variations in SLP between the Azores High in the subtropics and the Icelandic Low in the mid- to high latitudes, with some northward extension deep into the Arctic (Hurrell et al., 2003). The positive phase of the NAO corresponds to an anomalously strong Azores High and concomitant deepening of the Icelandic Low with some penetration in the subarctic basin (Greenland/Norwegian/Barents Sea), accompanied by a reinforced and northward shifted jet and storm track over a broad North Atlantic-European sector (Figure AIV.1a). The opposite, notwithstanding marginal spatial asymmetries, occurs for the negative phase.

The NAO is the main mode of climate variability over a broad North Atlantic-Europe region in all seasons (Hurrell and Deser, 2009) for intra-seasonal to multidecadal timescales, albeit with seasonally-dependent physical characteristics (fraction of explained variance, latitudinal shift and intensity of the related anomalous atmospheric circulation and SST fingerprint, etc.; Folland et al., 2009a; Woollings et al., 2015a). The phases of the NAO control a significant fraction of the variance of temperature and precipitation over the North Atlantic and surrounding continents and of the prevailing westerly winds and the related storm tracks (Woollings et al., 2014). It is also strongly related to the occurrence and intensity of blocking conditions especially over Greenland (Woollings et al., 2010; Davini et al., 2012) and controls a large part of the incidence of extremes (cold waves, very strong wind episodes related to explosive storminess, heavy precipitation events, etc.) over Europe (Matthews et al., 2014; Yiou et al., 2017) and eastern North America

ACCEPTED VERSION SUBJECT TO FINAL EDITING

(Durkee et al., 2008; Whan and Zwiers, 2017).

The NAO can be viewed as the regional expression of a hemispheric-scale mode of atmospheric variability that was identified in the late 1990s known as the Arctic Oscillation (AO; Thompson and Wallace, 1998) or Northern Annular Mode (NAM) (Thompson and Wallace, 2000a; Ambaum et al., 2001) to reflect the longitudinal scale that transcends the entire hemisphere. An additional centre of action is present for NAM over the North Pacific, albeit much weaker than its Atlantic counterpart, with a slackened Aleutian Low in the positive phase (Figure AIV.1b). The AO/NAM can be defined as the leading mode of variability across a range of atmospheric levels from the surface to the stratosphere (Baldwin and Dunkerton, 1999; Gerber et al., 2010). In the stratosphere, the AO/NAM corresponds to fluctuations in the strength of the boreal winter polar vortex over the Arctic. In the troposphere, the AO/NAM primarily corresponds to fluctuations in the position of the midlatitude westerly jet stream. Interactions between the stratospheric and tropospheric annular modes have been extensively studied and are important for the variability and predictability of the mode at intra-seasonal timescales (i.e. see Domeisen, 2019).

Despite the fact that NAM and NAO indices are strongly correlated (Figure AIV.1c), the debate on the relevance of the NAM as a mode of variability per se (Deser, 2000; Honda and Nakamura, 2001; Itoh, 2008) is not closed yet, despite progress in understanding the dynamical mechanisms linking the Pacific and Atlantic SLP cores on the basis of wave breaking theory that prevails at intra-seasonal timescales (e.g. Rivière and Drouard, 2015). Consequently, NAO and NAM are treated as indistinguishable in some studies (Feldstein and Franzke, 2006) while others still consider the NAO as a stand-alone mode even if associated circumpolar patterns exist (García-Serrano and Haarsma, 2017). In the latter case, the NAM is interpreted as a statistical artefact of two regional independent modes namely the NAO and the Pacific-North American pattern (Ambaum et al., 2001; Douville et al., 2017). Throughout the report, NAO and NAM are often considered as the same entity because the NAO explains most of the variance on the zonally-averaged hemispheric circulation and because the associated timeseries are highly correlated.

The NAO/NAM arise as large-scale signals primarily driven by internal atmospheric variability of midlatitude dynamics (e.g., Lorenz and Hartmann, 2003). By nature, these signals correspond to barotropic phenomena being partly controlled by eddy-mean flow interaction (Feldstein and Franzke, 2017). Their fingerprint can be found along the entire atmospheric column with maximum amplitude in the winter season when storminess is the most pronounced. In addition, the tropospheric NAO/NAM variability has been shown in boreal winter to be linked to the strength of the stratospheric polar vortex (Baldwin and Dunkerton, 1999) including sudden stratospheric warmings (Domeisen, 2019). On intra-seasonal timescales, downward propagation of associated geopotential height anomalies occurs from the lower stratosphere to the troposphere through wave-mean flow interaction resulting in some predictability at the surface for CIDs, through temperature, precipitation and wind anomalies at large spatial scales (e.g. Karpechko et al., 2017 over Europe).

The NAO/NAM includes a forced component arising from SST anomalies: key oceanic regions are identified but are dependent on the timescale of variability that is investigated (Baker et al., 2019). There is also growing evidence for the importance of cryosphere-atmosphere coupling to explain part of the observed variability of the NAO in response to recent Arctic sea-ice decline (Cohen et al., 2014), even if discrepancies remain in model estimates (Screen et al., 2018) and may not be stationary in time (Blackport and Screen, 2020). Finally, part of the NAO/NAM variability has also been documented to be influenced by external forcing such as volcanic eruptions (Swingedouw et al., 2017) and solar forcing (Ineson et al., 2011; Gray et al., 2016; Le Mouël et al., 2019) as well as anthropogenic factors (Gillett et al., 2003). However, internal variability is predominant and, because of signal-to-noise issues, very long observational records and large ensembles of climate simulations are needed to clearly evaluate the fraction of the forced component in the observed NAO/NAM, as assessed in detail in Sections 2.4.1.1 and 3.7.1. Sea ice-NAO/NAM coupling is comprehensively assessed in Cross-Chapter Box 10.1.

Given their equivalent barotropic structure, the NAO/NAM is usually defined from SLP fields or geopotential height anomalies at various levels (Fu et al., 2016). The NAO/NAM can be defined using pattern-based statistical techniques such as EOF or clustering techniques applied to seasonal gridded

ACCEPTED VERSION SUBJECT TO FINAL EDITING

atmospheric circulation fields (SLP or geopotential height anomalies) from observations or reanalysis data. The NAM pattern is traditionally defined as the leading EOF of pressure fields computed over the entire hemisphere, northward of 20ºN (Figure AIV.1b) and its related PC defines the NAM index (Figure AIV.1c). Similarly the NAO index can be defined as the PC of the leading EOF of the pressure field over the North Atlantic sector (Figure AIV.1a) or the temporal occurrence of the seasonal weather regimes extracted from clustering (Corti et al., 1999; Cassou et al., 2011; Hannachi et al., 2017).

An alternative and simpler estimate of the NAM/NAO uses differences in SLP between fixed locations. The NAM index can be calculated from the difference in normalized zonally averaged SLP between 35ºN and 65ºN (Li and Wang, 2003), which reflects the latitudinal fluctuation of the position and strength of the midlatitude westerlies at the hemispheric scale. Similarly, for the NAO, a weather station-based index is traditionally calculated as the difference of normalized SLP anomalies located in the Azores (Ponta Delgada) or continental Iberia (Lisbon/Gibraltar) minus those along the northern centre of action around Iceland (Stykkisholmur/Reykjavik) (Jones et al., 1997). Cornes et al. (2013) alternatively uses the Paris-London difference because of data availability back to the 17th century. The station-based NAO index is simple to compute, extends the longest over the instrumental period, and can be used year round, but caveats stand in its limitation to capture the seasonal latitudinal migration of the NAO variability pattern as well as potential shifts in the North Atlantic pressure centres of action at interannual to decadal timescales (Ulbrich and Christoph, 1999). Because it uses fixed locations, the index captures part of the variability that is not directly related to the latitudinal seesaw pressure balance and associated large-scale fluctuations of the zonal flow that characterize the NAO dynamics, and it also fails representing the spatial asymmetries between the positive and negative phases of the mode (Cassou et al., 2004).

The temporal correlation between the EOF and fixed latitude-based zonal NAM estimations is equal to 0.91 for December-January-February average and both are strongly correlated with the NAO indices (Figure AIV.1c). Correlations between all the NAO estimates are spatially and temporally very high in all the observational products over the modern reanalyses period (Gerber and Martineau, 2018); for instance, the correlation between the station-based and EOF-based NAO indices over 1959-2018 in boreal winter using JRA-55 is equal to 0.89 (Figure AIV.1c). EOF-based NAO and NAM indices are used in Section 3.7.1 for model evaluation. The fixed-latitude NAM index is used in Sections 2.4.1.1, 4.3.3.1, 4.4.3.1 and 4.5.3.1, and in Section 3.7.1 for attribution of past changes.

[START FIGURE AIV.1 HERE]

Figure AIV.1: The boreal wintertime NAO and NAM modes extracted as the leading EOF of December-January-February SLP anomalies over the North Atlantic-Europe Sector (20ºN-80ºN, 90ºW-30ºE, materialized by the red box, a) and the Northern Hemisphere (north of 20ºN, black domain, b), respectively, based on JRA-55 reanalysis over 1959-2019. (a,b) SLP anomalies regressed onto the leading principal component (PC) time series shown in (c). The NAO-PC is represented by red and blue bars, the NAM-PC by the black curve in (c); their variance explained is given in the legend. The NAO index based on weather stations (cyan dots in a) is given in cyan and the zonal-NAM index (latitude circles in b) is given in magenta. Correlation between each index and the NAO-PC timeseries is given in the legend. (d,e) Regression maps of blended SST and SAT over land from ERSST and BerkeleyEarth dataset, respectively, over for 1959-2019 (d) and of precipitation anomalies (e, shading based on GPCC for 1959-2016 and contours based on CMAP for 1979-2019 for every 0.1 mm/day). On maps, no-overlay indicates regions where the regressions are significant based on t-test accounting for false detection rate at 10% and crosses indicates no significance. Significance for CMAP precipitation is materialized by red contours in (e). All fields have been linearly detrended prior to computation.

[END FIGURE AIV.1 HERE]

AIV.2.1.2 Teleconnections and regional influence

Large-scale changes in the position and strength of the North Atlantic jet stream and storm tracks associated

ACCEPTED VERSION SUBJECT TO FINAL EDITING

with the NAO/NAM, as well as the related incidence in blocking episodes traditionally linked to extreme events, affect surface climate conditions over the entire North Atlantic and surrounding landmasses from daily to multidecadal timescales (Hurrell, 1995). Warmer and wetter weather over Northern Europe extending eastward in western Siberia with simultaneous cooler and drier conditions over a broad Mediterranean basin are distinct features of the positive boreal winter NAO/NAM (Figure AIV.1d,e). Over North America, regions around the Labrador Sea are significantly colder with excess sea-ice formation while milder conditions dominate the Great Plains forming altogether a typical quadripolar anomaly pattern for temperature linked to the winter NAO/NAM. The latter structure is tightly related to the latitudinal shift of the storm tracks that is particularly marked in precipitation over the ocean (Figure AIV.1e). More remotely, changes in North Atlantic storm track position and transient eddy activity associated with the positive (negative) phase of the NAO contribute downstream to negative (positive) SLP anomalies in north-eastern East Asia during boreal summer (Linderholm et al., 2011).

Related changes in both westerly winds at midlatitudes and trade winds in the tropics over the North Atlantic result in anomalous fluxes of sensible and latent heat at sea surface, which create ocean temperature anomalies that extend down to the base of the deep mixed layer during boreal winter (Deser and Timlin, 1997; Seager et al., 2000). The SST imprint of the NAO has a tripolar shape with positive anomalies at midlatitudes straddled by colder surface ocean in the subtropics and along the entire subpolar gyre (Figure AIV.1d). Weak feedbacks from SST on boreal winter NAO are found through forced Rossby wave mechanism (Baker et al., 2019) and local phenomena such as oceanic re-emergence in the North Atlantic Nordic seas (Cassou et al., 2007). Negative NAO phases are characterized by a wavier jet stream and a southward shift of storm tracks, which favours cold outbreaks over Northern Europe (Cattiaux et al., 2010) and reinforced storminess along the Mediterranean basin leading to heavy precipitation events (Sanchez-Gomez et al., 2008) and storm surge in southern Europe (Cid et al., 2016). Those are also often related to a collapse/split/displacement of the low-level stratospheric polar vortex and the occurrence of Stratospheric Sudden Warming (Sections 2.3.1.4.5 and 3.3.3.4). In boreal winter, NAM and NAO teleconnections are very similar over the Atlantic surrounding continents.

There is a strong seasonal asymmetry in observed NAO teleconnection patterns and NAO temporal evolution. Impacts over Europe are opposite between summer and winter months with dominant warmer and drier weather conditions over north-western Europe in summertime concurrently with wetter conditions over Southern Europe during positive NAO phases (Folland et al., 2009; Bladé et al., 2012). Extreme events (heat waves occurrence, droughts, etc.) are also linked to NAO phases (Cassou et al., 2005; Drouard et al., 2019) due to the related latitudinal shift of the North Atlantic storm tracks (Dong et al., 2013). Summer NAO trends also affect Arctic climate as assessed in Sections 3.4.1 and 9.4.1. The NAO is associated with storms or persistent mild wind period and dry/sunny spells affecting availability and power consumption (Jerez et al., 2013; Zubiate et al., 2017).

NAO fluctuations generate ocean responses due to altered buoyancy fluxes and wind stress anomalies (Barrier et al., 2014). Signatures of the NAO can be found in the gyre circulations (Marshall et al. 2001) and in the Atlantic Meridional Overturning Circulation (AMOC; Yeager and Danabasoglu, 2014), with a sea level imprint in observations (Han et al., 2017). The oceanic response is dependent on the timescale of the NAO variability (Delworth and Zeng, 2016) especially for AMOC in connection with the so-called Atlantic Multidecadal Variability (Section AIV.2.7). This is assessed in Section 9.2.3.1.

Implications of NAO/NAM variability in terms of observed and projected precipitation at a regional scale (Europe, Mediterranean basin, etc.) is comprehensively assessed in Sections 8.3.2.9, 8.4.2.9, and 8.5.2. NAO implications on extremes are assessed in Sections 11.3.1 and 11.4.1, and regional manifestations of NAM/NAO are further assessed in Sections Atlas.5, Atlas.7, Atlas.8 and Atlas.9 and Cross-Chapter Box Atlas.2.

AIV.2.1.3 Available proxy-based reconstruction

Sea level pressure records from Stykkisholmur, Akureyri, Reykjavik and from Gibraltar, Lisbon and Ponta

ACCEPTED VERSION SUBJECT TO FINAL EDITING

Delgada weather stations, all located close the NAO centres of action (i.e. Islandic Low and Azores high), allowed the reconstruction of the NAO index back to the mid-19th Century (Cropper et al., 2015; Hernández et al., 2020). The Paris-London sea level pressure difference used by Cornes et al. (2013) extends back to 1692, but it captures only part of the large-scale NAO phenomena because of the spatial proximity of the weather stations used. More reliable NAO reconstructions were recently developed based on the reconstruction of the sea level pressure field all over the North Atlantic and Europe (Delaygue et al., 2019; Mellado-Cano et al., 2019). Other long-term reconstructions involve proxy-based information from documents (Barriopedro et al., 2014), tree rings (Cook et al., 2019), ice cores (Sjolte et al., 2018), stalagmites (Baker et al., 2015), sediments (Faust et al., 2016) and a combination of multi-proxy information (Ortega et al., 2015), with large uncertainties due to diverse methodological approaches used for reconstruction (Michel et al., 2020) and disparate correlations between proxies and associated temporal resolution (Hernández et al., 2020). An additional difficulty for reconstruction lies on the fact that the spatial structure of North Atlantic variability might be time-scale dependent (Woollings et al., 2015). It is shown that on the shorter timescale (interannual), the NAO is dominated by variations in the latitude of the North Atlantic jet and storm track, whereas on the longer timescale (multidecadal and beyond) it represents changes in their strength instead. The two timescales also exhibit different regional impacts on temperature and precipitation and different relationships to sea surface temperatures, which makes proxy reconstructions of the NAO problematic.

Most of the reconstructed NAO/NAM indices describe the winter patterns of the last 500 years because the variability is the most pronounced and on larger-scale for that season (Luterbacher, 2001; Dezileau et al., 2011). Tree rings can however allow NAO boreal summer reconstruction back to the 16th century (Folland et al., 2009; Linderholm et al., 2009). Recent efforts to develop reconstructions of the NAO phases using pollen data (Mauri et al., 2014), speleothems (Ait Brahim et al., 2019) and lake sediments (Olsen et al., 2012) provide new evidence for multi-centennial NAO-type of variability along the Holocene (Hernández et al., 2020). A detailed description of the latest proxy-based reconstructions of the NAO and related conclusions placing the observations since the pre-industrial in a broader context of variability are given in Section 2.4.1.1.

AIV.2.2 Southern Annular Mode

AIV.2.2.1 Definition of the mode

The Southern Annular Mode (SAM), sometimes called the Antarctic Oscillation (AAO), is the leading mode of large-scale atmospheric circulation variability in the Southern Hemisphere extra tropics in all seasons and at intra-seasonal to multidecadal timescales, albeit with season-dependent physical characteristics such as fraction of explained variance, latitudinal shift and intensity of the related anomalous atmospheric circulation and SST fingerprint. It is characterized by synchronous SLP or geopotential height anomalies of opposite signs between the mid- and high latitudes, modulating the mean westerly winds near 50ºS. The SAM affects the frequency, strength, and position of cold fronts, and extratropical synoptic to mesoscale weather systems (Thompson and Wallace, 2000b; Manatsa et al., 2016; Mariani and Fletcher, 2016; Cerrone and Fusco, 2018). It controls a significant fraction of seasonal to multi-annual variance of the zonal mean precipitation in the Southern Hemisphere subtropics and extratropics (Kang et al., 2011). The SAM is also tightly linked to the fluctuations in the thermohaline properties of the Southern Ocean as well as its dynamics (Sen Gupta and England, 2006; Spence et al., 2014), and it modulates the Antarctic sea ice extent from interannual to multidecadal timescales (Ferreira et al., 2015).

Given its equivalent barotropic structure, the SAM is commonly quantified as the first EOF mode of extratropical geopotential height anomalies at various tropospheric levels or of SLP anomalies. However, it extends into the stratosphere, coupling lower and middle-atmosphere dynamics. As it essentially represents a meridional atmospheric mass transfer, an alternative definition is the difference in normalized zonal mean SLP at middle (40ºS) and high (65ºS) southern latitudes (Gong and Wang, 1999; Marshall, 2003). The polarity of the SAM is defined such that it is positive when pressure over Antarctica is anomalously low, and vice versa. While the SAM pattern is more zonally symmetric than its Northern Hemisphere counterpart (NAM, Section AIV.2.1), it does exhibit some asymmetries particularly in the midlatitude node over the

ACCEPTED VERSION SUBJECT TO FINAL EDITING

Pacific and Indian Ocean sectors (Fogt et al., 2012). Alternative interpretations of the SAM as a regional variability pattern in the South Pacific are also considered (Spensberger et al., 2020). The zonal asymmetries are present for all seasons, and illustrated in Figure AIV.2a for austral summer, to support the assessment in Section 3.7.2. A number of different SAM indices have been produced, and several are compared by Ho et al. (2012) and Barrucand et al. (2018), showing good agreement after the second half of the 20th century. Over the 1979-2019 period, the correlation between the EOF-based and zonal SLP-based indices for the summertime SAM reaches 0.94 (Figure AIV.2b).

During the positive phase of the SAM, the Antarctic air mass is isolated by an enhanced westerly jet that is located further south than during the negative phase. This leads to colder conditions over the entire continent and negative SST anomalies along the surrounding ocean (Figure AIV.2). During the opposite, negative phase, an equatorward displacement of the jet and related storm track brings low pressure systems toward the north with a strong effect on southern tip of South America (Mariani and Fletcher, 2016). The SAM is often used as a proxy for the location of the midlatitude westerly wind belt at seasonal to interannual timescales. However, Swart et al. (2015) noted that trends in the SAM and the Southern Hemisphere surface westerly jet are not directly interchangeable because multiple factors other than SAM can affect trends in the position, width and strength of the jet and surface wind.

The SAM is mainly driven by extratropical atmospheric dynamics, but its phase is affected by remote SST anomalies such as ENSO (Section AIV.2.3) and anthropogenic forcing as assessed in Section 3.7.2.

The EOF-based SAM index is used for model evaluation in Section 3.7.2. The fixed-latitude SAM index is used for the attribution assessment of the observed positive trend of the SAM that is maximum over the second half of the 20th century but reduced since about 2000 (Section 2.4.1.2) due to slackened ozone influence (Section 3.7.2). The fixed-latitude SAM index is also used in Sections 4.3.3.1, 4.4.3.1 and 4.5.3.1 to assess the future changes in Southern Hemispheric zonal circulation as a function of emissions scenarios and lead times.

[START FIGURE AIV.2 HERE]

Figure AIV.2: The austral summertime SAM extracted as the leading EOF of December-January-February SLP anomalies over the Southern Hemisphere (south of 20ºS, a) based on JRA-55 reanalysis over 1979-2019. (a) SLP anomalies regressed onto the leading principal component (PC) time series shown in (b); the variance explained is given in the legend in (b). The SAM-PC is represented by red and blue bars and the zonal-SAM index (latitude circles in a) is given in magenta. Correlation between the zonal SAM index and the SAM PC timeseries is given in the legend. (c, d) Regression maps of SST and SAT over land from ERSST and BerkeleyEarth dataset, respectively, over for 1979-2019 (d) and of precipitation anomalies (e, shading based on CMAP for 1979-2016 and contours based on GPCP for 1979-2019 for every 0.1 mm/day). On maps, no-overlay indicates regions where the regressions are significant based on *t*-test accounting for false detection rate at 10% and crosses indicates no significance. Significance for CMAP precipitation is materialized by red contours in (d). All fields have been linearly detrended prior computation.

[END FIGURE AIV.2 HERE]

AIV.2.2.2 Teleconnections and regional influence

Recent observational studies have enriched our understanding of the widespread influence of SAM variability on mean climate and related environmental parameters of the entire Southern Hemisphere extratropics (e.g. Holz et al., 2017; Jones et al., 2016; Kostov et al., 2017; Manatsa et al., 2013; Marshall et al., 2017; Raut et al., 2014; Waugh et al., 2013). The influence of the SAM extends over the midlatitude continental land masses with precipitation anomalies over Southern Australia (Cai and Watterson, 2002) and south-eastern South America (Silvestri and Vera, 2003) in link with the latitudinal migration and strength of the extratropical storm and mean westerly circulation. Consistently with NAM/NAO (Section AIV.2.1),

ACCEPTED VERSION SUBJECT TO FINAL EDITING

there is a strong seasonality in the teleconnection associated with SAM. In austral summer, during a positive phase of the SAM, drier conditions affect most of the southern Patagonia region and the southernmost tip of South America, while wetter conditions are found in South Africa and Madagascar, as well as in Southeast Australia where colder temperatures also prevail (Figure AIV.2c,d). Positive temperature anomalies are found in New Zealand, Tasmania and Southern tip of South America. These anomalies appear as the continental fingerprint of a warmer belt located around 40oS that is characterized by significant hemispheric-scale SST changes in consistence with the southern shift of the summertime storm track.

Moreover, several studies have described equatorward teleconnections linking the SAM to Asian precipitation across the equator (e.g., Liu et al., 2018; Prabhu et al., 2017). Coupling of seasonal stratospheric anomalies to the SAM can influence spring-time heat extremes in eastern Australia (Lim et al., 2019). Marshall et al. (2013) described a reversal in the relationship between the SAM and East Antarctic temperatures during austral summer/autumn in the first decade of the 21st century, due to regional variability of the pressure pattern associated with the zonal wavenumber 3. Other studies have analysed the temporal variability in the interactions between the SAM and ENSO at different timescales (e.g. Clem et al., 2016; Yu et al., 2015), being positive and significant during 1986-2014 (Vera and Osman, 2018).

Implications of SAM on observed and projected changes in water cycle and specific regional influences are assessed in Sections 8.3.2.9 and 8.4.2.9 and in Sections 12.4, Atlas.7 and Atlas.11, respectively.

AIV.2.2.3 Available proxy-based reconstruction

The regional influence of the SAM is recorded in tree rings (Holz et al., 2017; Dätwyler et al., 2018), lake sediments (Fletcher et al., 2018; Moreno et al., 2018), ice cores (Goodwin et al., 2004) and corals (Goodwin and Harvey, 2008) across the Southern Hemisphere extratropics. Multiproxy-based reconstructions of the SAM have been developed using temperature-sensitive proxy records that cover the last millennium (Villalba et al., 2012; Abram et al., 2014; Dätwyler et al., 2018). Villalba et al. (2012) used tree ring records to reconstruct the summertime SAM since 1409, while Abram et al. (2014) combined ice core records with tree ring data to derive a weighted composite-plus-scale reconstruction of the annual SAM index for the past millennium. Dätwyler et al. (2018) further included proxies from corals, speleothems and lake sediments using different stationarity criteria for the proxy record selection to build an austral summer SAM reconstruction. Hessl et al. (2017) compared three paleoclimatic reconstructions of the SAM, highlighting the need for additional proxy records over the Indian Ocean sector, to fully account for the annular structural properties of this mode of variability. Uncertainties also arise from the lack of proxy data related to cold season conditions, given that reconstructions relying on tree rings might be biased towards summertime thus accounting only for SAM austral summer variability (Hernández et al., 2020). Several studies attempted to reconstruct the SAM behaviour during the Holocene, inferred through changes in the Southern Hemisphere westerly wind belt, but uncertainties remain large without consensus in the SAM phases for most of the periods at multidecadal timescales (Hernández et al., 2020). These SAM reconstructions are assessed in Section 2.4.1.2 and compared with simulations in Section 3.7.2.

AIV.2.3 El Niño-Southern Oscillation

AIV.2.3.1 Definition of the mode

The El Niño-Southern Oscillation (ENSO) refers to the large-scale alternation between anomalous warming and cooling of central/eastern equatorial Pacific SSTs that coincide with changes in the overlaying winds and precipitation (Philander, 1990; Neelin et al., 1998; Wang, 2018). The main features of ENSO are displayed in Figure AIV.3. ENSO is the primary mode of tropical variability on interannual timescales and is considered as an internally occurring coupled ocean-atmosphere phenomenon. Whilst the ENSO phenomenon itself largely occurs in the tropical Pacific, it triggers climate teleconnections over the entire basin and in many other parts of the world (Figure AIV.3c,d). ENSO is consistently the main modulator of the global surface temperature at interannual timescales (Pan and Oort, 1983; Trenberth et al., 2002). ENSO

ACCEPTED VERSION SUBJECT TO FINAL EDITING

is the main source of climate predictability on seasonal to interannual timescales (Philander, 1990; Smith et al., 2012) and its status is consequently closely monitored by meteorological institutes around the globe. El Niño events are typically identified by warmer than normal central/eastern equatorial Pacific SSTs, negative SLP anomaly difference between the eastern and western portions of the tropical Pacific Ocean, anomalous westerly surface winds, and increases in cloudiness and precipitation over the central and eastern equatorial Pacific and adjacent land areas. By contrast, La Niña events are typically identified by cooler than normal central/eastern equatorial Pacific SSTs, positive surface pressure anomaly difference between the eastern and western portions of the tropical Pacific Ocean and anomalous easterly surface winds reflecting altogether an intensification of the climatological east-west thermal gradient across the equatorial Pacific Ocean.

ENSO has been monitored through a range of indices, which are based on SST or SLP anomalies during the instrumental period, and various proxies on longer timescales. Differences between indices and thresholds used to define the occurrence of an El Niño or La Niña event imply that no commonly accepted list of events and their magnitudes exists. The three most prominent (L'Heureux et al., 2017; Pepler, 2016) indices used to monitor ENSO are the averaged SST anomalies over the so-called NINO3 (5ºS-5ºN, 150ºW-90ºW) or NINO34 (5ºS-5ºN, 170ºW-120ºW) regions and the Southern Oscillation Index (SOI) based on the normalized SLP difference between Darwin and Tahiti (Troup, 1965). Decomposition into EOFs of the tropical SST is also used in the literature. Those indices are highly correlated, as shown in Figure AIV.3b. The correlation between NINO34 SST and EOF-SST index is about 0.97, and between NINO34 and SOI is about 0.89 over the 1959-2019 period.

SST anomalies from the NINO3 and NINO34 regions provide a direct measure of the events via its surface ocean fingerprint, while the SOI provides a measure in terms of atmospheric perturbation. Data are available back to 1876 for the SOI computation, whilst the uncertainty in SST-based indices, particularly those associated with the central equatorial Pacific, is large prior to the 1950s when the number of SST observations was much lower (Kennedy et al., 2019). The complexity of ENSO is at least partly demonstrated by the observed events, which are all different in the magnitude, spatial structure and/or seasonal timing. As a direct consequence, it is difficult to accurately represent ENSO with one single index. Over time, further indices have been introduced to monitor ENSO event evolution (i.e., Trans Niño Index – TNI, Trenberth and Stepaniak, 2001) and spatial structure (i.e., El Niño Modoki Index – EMI, Li et al., 2010). The limited length and quality of the observational records may further affect the choice of the index, whose relevance can depend on the specific application. The variety in ENSO indices also explains the non-universality in the qualification of ENSO status delivered by meteorological agencies responsible for operational monitoring, operational forecast and climate services for users.

A particular aspect of ENSO diversity is whether the event is centred in the eastern Pacific (EP events) or central Pacific (CP or "Modoki" events). This distinction is important as the type of event leads to different large-scale teleconnections and worldwide climatic impacts (e.g. Ashok et al., 2007; Ratnam et al., 2014; Capotondi et al., 2015; Timmermann et al., 2018; Taschetto et al., 2020). Differences can be significant at regional scale because of displaced source of diabatic heating associated with the position of the main SST anomalies. For instance, stronger precipitation teleconnections occur over Australia during CP than during EP events (Wang and Hendon 2007; Taschetto et al. 2009). It is noteworthy that central and eastern Pacific SST indices are more highly correlated with each other during La Niña than during El Niño events. This indicates that La Niña events have less geographic diversity than El Niño events (Kug and Ham, 2011) and that the CP/EP distinction is therefore more relevant for the latter. In the historical instrumental records, Banholzer and Donner (2014) found that CP events had a weaker influence on global surface temperature than EP events did.

However, the distinction between CP and EP events is not necessarily clearly defined, as different methods yield an inconsistent classification of the events, which implies that no robust consensus on the classification of CP or EP events is possible (Wiedermann et al. 2016). Furthermore, Giese and Ray (2011) found that the central longitude of peak SST anomalies associated with individual El Niño events had a distribution indistinguishable from a Gaussian distribution peaked at 140ºW, as opposed to a bimodal distribution implied by the EP/CP paradigm. There are also occasional "coastal Niño" events, such as those of 1925 (Takahashi and Martinez, 2019) or 2017 (Rodriguez-Marata et al., 2019), where abnormally warm waters are

ACCEPTED VERSION SUBJECT TO FINAL EDITING

confined to the South American coast. Even though these events are not conventionally classified as El Niños, they have some El Niño-like teleconnections in South America. Instrumental data have historically been of limited value in assessing the classification of events before 1955, because of the almost total lack of SST measurements in the western half of the NINO34 region (L'Heureux et al., 2013). It is not yet known whether newer SST data set versions, which benefit from improved data archives (Section 2.3.1.1), have reduced this uncertainty.

The description of ENSO in this Annex supports the assessments of Sections 2.4.2, 3.7.3, 4.3.3.2, 4.4.3.2 and 4.5.3.2. ENSO's influence on ocean circulation, heat transport and sea levels are assessed in Sections 9.2 and 9.6.

[START FIGURE AIV.3 HERE]

Figure AIV.3: The boreal wintertime ENSO mode defined by December-January-February SST anomalies averaged over the NINO34 region (5ºS-5ºN, 170ºW-120ºW, cyan box) or extracted as the leading EOF mode over the Tropical Pacific Ocean (the region denoted by the black box in a) for 1958-2019 using ERSSTv5. (a) SST anomalies regressed onto the NINO34 time series, which is shown in (b) as red and blue bars. Black curve in (b) represents the standardized leading principal component and the magenta curve stands for the SOI index. The percentage of explained variance of the leading EOF is given in the legend as well as the correlation between all indices and the NINO34 timeseries. (c) Same as (a) but for land SAT (shading; based on BerkeleyEarth) and 10-m level wind (arrows; based on JRA-55) anomalies over 1958-2018. (d) Same as (a) but for precipitation anomalies (shading based on GPCC for 1958-2016 and contours based on CMAP for 1979-2019 for every 0.5 mm/day). Magenta dots in (c,d) stands for the Darwin and Tahiti weather station used for the SOI computation. On maps, no-overlay indicates regions where the regressions are significant based on t-test accounting for false detection rate at 10% and crosses indicates no significance. Significance for CMAP precipitation is materialized by red contours in (d). All fields have been linearly detrended prior to computation.

[END FIGURE AIV.3 HERE]

AIV.2.3.2 Teleconnections and regional influence

ENSO has a broad range of teleconnections, both in and outside the Pacific region (Figure AIV.3c,d). Amongst the best-known teleconnections are the association of El Niño events with increased precipitation in the southwestern and southeastern United States, eastern Africa, coastal Ecuador and Peru, and northern Argentina, and with decreased precipitation in eastern Australia and the Maritime Continent, southern Africa, the Amazonian basin and much of the Indian subcontinent. A general reverse association is found during La Niña events although there are some asymmetries (Cai et al., 2010; Taschetto et al., 2020). ENSO also has a substantial impact on tropical cyclone occurrence (Wang and Chan, 2002; Chu, 2004; Kuleshov et al., 2008), with El Niño typically being associated with reduced tropical cyclone activity in the North Atlantic, and an eastward displacement of Northwest and South Pacific tropical cyclone genesis away from the Philippine Sea and the Australian continent and into the central Pacific. ENSO have been shown to control part of the interannual variability of fire, including wildfire and human-triggered fires, in many regions of the world including all the continents surrounding the Pacific (see for instance the devastating extreme fire emissions in Indonesia in 2015, Chisholm et al. 2016) but also remotely, e.g. over the Arctic (Monks et al., 2012).

Tropical climate impacts during ENSO events are largely driven by a reorganisation of the zonal Walker circulation that result from anomalous diabatic heating associated with deep atmospheric convection changes (e.g. Chiang and Sobel, 2002; Choi et al., 2015; Gill, 1980; Klein et al., 1999). The latter are also responsible for atmospheric teleconnections to higher latitudes (Yeh et al., 2018), acting as a source of forced large-scale Rossby waves (Hoskins and Karoly, 1981). Specific phases of the Pacific-North American (PNA) pattern (Horel and Wallace, 1981) and Pacific-South American (PSA) pattern (Karoly, 1989) are then favoured in the Northern and Southern Hemispheres, respectively, and are associated with shift and modulation of the

ACCEPTED VERSION SUBJECT TO FINAL EDITING

mean storm tracks. These teleconnections influence temperature and rainfall around the globe including extreme events (King et al., 2014). For instance, mild winter conditions dominate Alaska/Canada connected to the southeastward displacement and reinforcement of the Aleutian Low during El Niño, which generates anomalous southerlies and advects warmer air northward. By contrast, the anomalous cyclonic circulation favours cold outbreaks over the far-east Siberian region and Kamtchaka (Figure AIV.3c,d).

Being the dominant actor of variability at interannual timescale, ENSO is linked to many other modes of variability both in the tropics and midlatitudes, either in phase or with some seasonal lag. For instance, connection has been documented between EP ENSO events and SAM during austral summer (Ciasto et al., 2015). Relationship exists between ENSO and the NAO/NAM in boreal wintertime though various mechanisms such as stratosphere-troposphere coupling (Domeisen et al., 2015) and tropospheric pathways, including the eastward extension of the PNA during El Niño event and also through the alteration of the propagation of tropical Rossby wave trains from the Pacific to the Atlantic (Drouard et al., 2015). The tropical-extratropical teleconnection is not symmetrical with the phase of ENSO and nonstationary with considerable dependence on epochs being modulated by the inherent strong internal variability (Deser et al., 2017; Drouard and Cassou, 2019). In the Atlantic, relationship between ENSO and Atlantic Niño (Section AIV.2.5) is found in boreal spring (Tokinaga et al., 2019) while the South Atlantic Subtropical Dipole mode is mostly connected to ENSO in austral summer (Rodrigues et al., 2015).

Implications of ENSO in water cycle changes are further assessed in Sections 8.3.2.9 and 8.4.2.9. Association of ENSO with extremes and specific regional climate anomalies are assessed in Sections 11.4, 11.6, 11.7, 12.4, Atlas.4, Atlas.5, Atlas.6, Atlas.7, and Atlas.9 and Box 11.4.

AIV.2.3.3 Available proxy-based reconstruction

Model evidence suggests that ENSO characteristics vary on decadal to centennial timescales (e.g. Lewis and LeGrande, 2015; Deser et al., 2017), implying that a minimum of several hundred years of observations, which is much longer than the instrumental record, are required to determine the full natural range of ENSO complexity (Wittenberg, 2009). Thus, one way to understand if anthropogenic forcing has modulated ENSO is to understand ENSO behaviour prior to the observational record. Paleoclimate archives can be used to fill this gap as they provide quantitative estimates of ENSO behaviour during the pre-industrial era, while also providing information of ENSO characteristics under a variety of past natural climate background states controlled by external forcings. Extensive proxy-based studies, using a range of ENSO-sensitive records, have been carried out to assess the ENSO changes on various paleoclimate timescales, specifically the last few hundred years and back to the mid-Holocene (see Section 2.4.2).

Reconstructions of past ENSO behaviour traditionally merges information from multiple proxies that are considered sensitive to ENSO (Lu et al., 2018). This merging process may have multiple purposes, but is generally used to extend the reconstruction length and also to increase its signal to noise ratio. The resulting reconstructions can be broadly placed into two main categories: (i) those that utilise proxies in the central and eastern equatorial Pacific itself; and (ii) those that utilise proxies from other regions impacted through teleconnections, along with those that mix both categories. ENSO reconstructions from category (i) are considered to be a more accurate measure of ENSO behaviour. However, proxies from the central and eastern equatorial Pacific are generally rarer than those outside the region, due to the small number of land/reefs, and they also tend to be of shorter duration. Thus, the ideal case is a combination of both categories to get a robust quantitative estimates of ENSO behaviour in the past.

AIV.2.4 Indian Ocean Basin and Dipole Modes

AIV.2.4.1 Definition of the mode

The Indian Ocean basin (IOB) and Indian Ocean dipole (IOD) modes are the two dominant modes of interannual climate variability in the Indian Ocean. The IOB mode features the temporal alternation of basin-

ACCEPTED VERSION SUBJECT TO FINAL EDITING

wide warming and cooling of sea surface in the positive and negative phases, respectively (Figure AIV.4), while the IOD mode is characterized by a zonal dipole of SST anomalies in the tropics, with one lobe centred off Sumatra and Java and the other covering a large portion of the western basin (Figure AIV.5). The two modes mostly vary on interannual timescales and are both correlated positively with ENSO. In particular, the IOD tends to emerge during ENSO development from boreal summer to autumn (Stuecker et al., 2017), followed by the IOB which grows in ENSO peak season and persists for a few subsequent seasons (Tokinaga and Tanimoto, 2004).

The IOB mode is considered primarily as a response to ENSO associated with large-scale alteration of the Walker circulation, and thus matures in boreal spring, a season after the typical ENSO peak (Klein et al., 1999; Lau and Nath, 2000, 2003). By contrast, the Bjerknes feedback is key to the formation of the IOD. This feedback requires background surface easterlies and thermocline shallowing in the eastern part of the basin along the equator, and this condition sets in boreal spring and persists until autumn, then dissipating by early winter in association with climatological monsoon wind swing. The IOD mode therefore develops in boreal summer and reaches its maximum amplitude in autumn, then rapidly terminates before winter (Schott et al., 2009). Differently from the IOB, strong internal feedbacks enable the IOD mode to develop also without influence from ENSO, as noted for some specific events (Saji and Yamagata, 2003a; Meyers et al., 2007).

The IOB and IOD are identified as the first and second EOF modes, respectively, of monthly SST variability in the tropical Indian Ocean (Weare, 1979; Saji et al., 1999). The IOD can be extracted also as the first EOF of SST variability in boreal autumn, although the pattern depends on the analysis period (Pillai et al., 2019). The IOD mode has a subsurface signature and can be also calculated as the leading EOF mode of the 20ºC isotherm depth of the Indian Ocean seawater temperature (Saji et al., 2006). Apart from the EOF definitions, the Tropical Indian Ocean averaged SST (20ºS-20ºN, 40ºE-100ºE or 40ºE-120ºE) is often used as the IOB mode index (Figure AIV.4a). For March-April-May, its correlation with the leading PC of Indian Ocean SST (Figure AIV.4b) reaches 0.98. For the IOD, SST anomaly difference between the western (10ºS-10ºN, 50ºE-70ºE) and eastern (10ºS-0º, 90ºE-110ºE) equatorial Indian Ocean is a widely used index (Saji et al. 1999; Figure AIV.5). It is highly correlated (at 0.76) with the leading principal component of the Indian Ocean September-November SST when assessed over 1958-2019 (Figure AIV.5b).

The IOB (Han et al., 2014) and IOD (Ashok et al., 2004a; Tozuka et al., 2007) -like variability can also be identified at decadal timescales. The decadal IOB mode is defined as the leading EOF mode of linearly detrended monthly SST after decadal time filtering (Han et al., 2014; Dong and McPhaden, 2017). 10-year low pass filtered Indian Ocean basin-mean SST is an alternative index for the decadal IOB mode (Dong et al., 2016), with the global-mean SST subtracted in some cases as an estimation of the response component to radiative forcing (Huang et al., 2019). The decadal IOD mode can be extracted as the second EOF mode of 10-year low-pass filtered Indian Ocean SST in boreal autumn (Yang et al., 2017), while other studies use the 10-year low-pass filtered SST anomaly difference between the western and eastern equatorial Indian Ocean (Ashok et al., 2004a; Tozuka et al., 2007).

Paleo fluctuations of IOB and IOD as well as the changes over the instrumental record period are assessed in Section 2.4.3, while their model representations are assessed in Section 3.7.4. Future variations under global warming are assessed in Sections 4.4.3.3 (near-term) and 4.5.3.3 (mid- to long terms).

[START FIGURE AIV.4 HERE]

Figure AIV.4: The boreal springtime IOB mode defined by March-April-May SST anomalies averaged over the Indian Ocean (the region denoted by the cyan box in a) or extracted as the leading EOF mode over the same domain (black contour) for 1958-2019 using ERSSTv5. (a) SST anomalies regressed onto the IOB index timeseries shown in (b) in red and blue bars, while the black curve in (b) represents the leading principal component timeseries. Explained variance and correlation between indices are given in the legend in (b). (c) Same as (a) but for land SAT (shading; based on BerkeleyEarth) and 10-m level wind (arrows; based on JRA-55) anomalies for 1958-2018. (d) Same as (a) but for precipitation anomalies (shading based on GPCC for 1958-2016 and contours based on CMAP for 1979-2019 for

ACCEPTED VERSION SUBJECT TO FINAL EDITING

every 0.3 mm/day). On maps, no-overlay indicates regions where the regressions are significant based on t-test accounting for false detection rate at 10% and crosses indicates no significance. Significance for CMAP precipitation is materialized by red contours in (d). All fields have been linearly detrended prior to computation.

[END FIGURE AIV.4 HERE]

[START FIGURE AIV.5 HERE]

Figure AIV.5: The boreal autumn IOD mode defined by September-October-November standardized SST difference between the western (10ºS-10ºN, 50ºE-70ºE) and eastern (10ºS-0º, 90ºE-110ºE) equatorial Indian Ocean denoted by cyan boxes in (a) or extracted as the leading EOF mode over the Indian Ocean (the region denoted by black contour in a) over 1958-2019 using ERSSTv5. (a) SST anomalies regressed onto the IOD index timeseries shown in (b) in red and blue bars while the black curve represents the leading principal component timeseries. Explained variance and correlation between indices are given in the legend in (b). (c) Same as (a) but for land SAT (shading; based on BerkeleyEarth) and 10-m level wind (arrows; based on JRA-55) anomalies for 1958-2018. (d) Same as (a) but for precipitation anomalies (shading based on GPCC for 1958-2016 and contours based on CMAP for 1979-2019 for every 0.3 mm/day. On maps, no-overlay indicates regions where the regressions are significant based on t-test accounting for false detection rate at 10% and crosses indicates no significance. Significance for CMAP precipitation is materialized by red contours in (d). All fields have been linearly detrended prior to computation.

[END FIGURE AIV.5 HERE]

AIV.2.4.2 Teleconnections and regional influence

Since the IOB mode is tightly associated with ENSO, related climate anomalies can be viewed as part of ENSO's influence from boreal winter to subsequent spring. Still, the IOB mode plays an important role in modulating the ENSO influence on several regions. The positive phase of the IOB plays a major role in suppressing precipitation in the Maritime Continent from boreal winter to spring (Watanabe and Jin, 2002; Annamalai et al., 2005) and Northern Australia in austral summer (Taschetto et al., 2011) in concomitance with El Niño event (Figure AIV.3d). An anomalous surface anticyclone then forms over the Philippine Sea linked to the precipitation reduction in the tropical western Pacific and brings more precipitation to East Asia during El Niño winter and spring (Figure AIV.3d; Wang et al., 2000).

ENSO's equatorial Pacific SST anomalies typically dissipate by boreal summer, when the lingering IOB then plays the leading role in exerting climate anomalies in Asia and the Northwest Pacific (the Indian Ocean capacitor effect; Xie et al. 2009). The boreal summer IOB induces meridionally dipolar anomalies of precipitation and surface air temperature in Southeast and East Asia, with wetter and cooler summer in midlatitude East Asia and drier and warmer summer in Southeast Asia during positive IOB events (Kosaka et al., 2013; Wang et al., 2013). These conditions affect the occurrence of extremes such as heavy rainfall (often caused through atmospheric rivers; Kamae et al. 2017) and heat waves (Hu et al., 2012; Deng et al., 2019). The positive IOB suppresses summertime tropical cyclone formation in the Northwest Pacific (Du et al., 2011; Ueda et al., 2018), leading to a delayed onset of the typhoon season (Zhao et al., 2019). These regional influences are already present in the spring season (Figure AIV.4c,d) but tend to persist and even get reinforced due to the persistence of the IOB, while following the seasonal climatological displacement of tropical dynamics (monsoon etc.). In South Asia, tripolar precipitation anomalies form in boreal summer, with precipitation increase along the Western Ghats and in Bangladesh and decrease around the Ganges Delta during the positive IOB (Chowdary et al., 2013, 2019).

The IOD is associated with climate anomalies in broad regions (Figure AIV.5c,d). However, the related anomalies are interfered with influences from concomitant ENSO. The IOD affects rainfall in eastern Africa, South Asia, Indonesia and Australia (Figure AIV.5c,d). The IOD in the positive phase increases rainfall in eastern tropical Africa in boreal autumn to early winter (Figure AIV.5d), while the negative phase induces

ACCEPTED VERSION SUBJECT TO FINAL EDITING

the opposite anomalies. These anomalies are also found in association with ENSO (Figure AIV.3d), but the explained variance by IOD is larger (Saji and Yamagata, 2003b). Both positive IOD and El Niño events reduce precipitation and temperature over the entire Maritime Continent (Figure AIV.5c,d and Figure AIV.3c,d) because of strong low-level divergence coupled with upper-level convergence related to diminished convection, while the opposite anomalies are induced by negative IOD and La Niña episodes (Saji and Yamagata, 2003b). The positive phase of the IOD also decreases rainfall in western to south-eastern Australia (Ashok et al., 2003; Risbey et al., 2009) acting as preconditioning for fires (Cai et al., 2009). The rainfall anomalies cover the entire Australia when combined with simultaneous ENSO with the same polarity (Risbey et al., 2009). The IOD influences South Asian summer monsoon rainfall either directly through moisture transport over the western Indian Ocean or modification of the local Hadley cell (e.g., Ashok et al., 2001; Gadgil et al., 2004; Ashok and Saji, 2007; Behera and Ratnam, 2018), or indirectly in the framework of the tropospheric biennial oscillation (e.g., Meehl et al., 2003; Li et al., 2006; Webster and Hoyos, 2010). IOD and ENSO often interfere in their influence on the south Asian summer monsoon (e.g., Ashok et al., 2001, 2004b; Pepler et al., 2014; Crétat et al., 2017). Opposing influence of IOD and ENSO has been found on surface temperature in summertime Northeast Asia (Saji and Yamagata, 2003b).

Implications of these modes on water cycle changes and specific regional influences are further assessed in Sections 8.3.2.9 and 8.4.2.9 and in Sections 12.4, Atlas.5, Atlas.6, Atlas.7 and Cross-Chapter Box Atlas.2, respectively.

AIV.2.4.3 Available proxy-based reconstruction

Corals record interannual and longer variability in the Indian Ocean (Zinke et al., 2005, 2009). Several studies have developed IOD reconstructions based on oxygen isotope ratios from corals. These reconstructions include those based on samples from Kenya since 1887 (Kayanne et al., 2006), from the Mentawai Islands in western Indonesia for the last 6,500 years (Abram et al., 2007) and in combination with samples from Bali in southern Indonesia and the Seychelles since 1846 (Abram et al., 2008). Abram et al. (2020) developed a coral-based reconstruction of the IOD for the last millennium, albeit with some discontinuity. Niedermeyer et al. (2014) use isotope compositions in terrestrial plant wax to reconstruct rainfall changes over Northwest Sumatra, which is highly correlated with the IOD. Compared to the IOD, proxy-based IOB reconstruction is limited. Yet, Du et al. (2014) find that coral oxygen isotope records from the Seychelles are well correlated with the IOB, suggesting that they can be used as an IOB proxy. Evidence from other proxies that are potentially associated with the Indian Ocean variability is assessed in Section 2.4.3.

AIV.2.5 Atlantic Meridional and Zonal Modes

AIV.2.5.1 Definition of the mode

The Atlantic Zonal Mode (AZM), also commonly referred to as the Atlantic Niño, and the Atlantic Meridional Mode (AMM) are the two dominant modes of tropical Atlantic climate variability on interannual to decadal time scales. The AZM peaks during the boreal summer upwelling season with maximum SST anomalies in the eastern equatorial Atlantic and is commonly regarded as the Atlantic counterpart of the Pacific El Niño (Zebiak, 1993; Keenlyside and Latif, 2007; Lübbecke et al., 2018; Foltz et al., 2019). The AMM, which is more active on longer time scales, peaks during boreal spring and exhibits a cross-equatorial gradient of SST with opposite signs in the northern and southern portion of the Atlantic. Both modes are associated with changes in the Intertropical Convergence Zone (ITCZ) and related winds and exert a strong influence on the climate in adjacent and remote regions.

The AMM is thought to be primarily driven by air-sea heat fluxes and therefore thermodynamic in nature (Chang et al., 2000; Foltz and McPhaden, 2010), while various mechanisms for generating AZM events have been discussed. They mainly concern fluctuations in the wind field over the equatorial Atlantic. These wind stress anomalies can be excited by local SST changes, as part of Bjerknes feedback (i.e. weakening of trade

ACCEPTED VERSION SUBJECT TO FINAL EDITING

winds and thermocline slope adjustments via oceanic equatorial Kelvin wave propagation; Keenlyside and Latif, 2007; Deppenmeier et al., 2016). They can also be excited by meridional advection of temperature anomalies (Richter et al., 2013), generated remotely as a response to ENSO (Latif and Grötzner, 2000; Tokinaga et al., 2019) or to variations in the South Atlantic subtropical high (Lübbecke et al., 2014), or occur as stochastic wind variability (Richter et al., 2014). In contrast to previous mechanisms involving coupled atmosphere-ocean dynamics, Bellomo et al. (2015) and Nnamchi et al. (2015) suggested that a large part of the SST variability in the eastern equatorial Atlantic can be explained by thermodynamic feedbacks excited by stochastic atmospheric perturbations. A recent study based on observational and reanalysis products by Nnamchi et al. (2021) indicates that the seasonality of AZM is indeed largely controlled by the variability of the atmospheric diabatic heating. However, the balance between thermodynamic and dynamic processes determining SST variability in the equatorial Atlantic is subtle, and other studies (e.g. Jouanno et al., 2017; Dippe et al., 2018) conclude that, even if the thermodynamic component is not negligible, the dynamics is the dominant driver of the AZM.

The AZM and AMM represent the first and second EOF patterns of the tropical Atlantic variability identified using SST anomalies in this region (Figure AIV.6a and Figure AIV.7a). These modes may also be defined using box averages, with the AZM defined as SST anomalies averaged over the equatorial Atlantic region called ATL3 (3ºS-3ºS, 0º-20ºW), and the AMM defined as the difference between the SST anomalies averaged over the tropical North Atlantic and tropical South Atlantic (i.e. 5ºN-30ºN, 20ºW-60ºW minus 5ºN-20ºS, 5ºE-25ºW). In boreal summer, the ATL3 and the EOF-AZM PC are correlated at 0.87 during 1958-2019 (Figure AIV.6b). The correlation between the AMM-box index and the EOF-AMM PC is lower, i.e. 0.39 (Figure AIV.7b), but increases to 0.67 over 1900-2019.

For the AMM, the latitudinal polarity in SST anomalies is associated with wind gradient and flow from the cooler to the warmer hemisphere (Ruiz-Barradas et al., 2000; Chiang and Vimont, 2004; Lübbecke et al., 2018; Foltz et al., 2019; Figure AIV.7c). For the AZM, similarly to ENSO in the Pacific Ocean, anomalous westerlies lead to low-level convergence over warmer SST along the climatological cold tongue (Figure AIV.6c).

The temporal evolution of the Atlantic modes of variability and their model representation are assessed in Sections 2.4.4 and Section 3.7.5, respectively. Their near-term and long-term evolution is assessed in Sections 4.4.3.4 and 4.5.3.4, respectively.

[START FIGURE AIV.6 HERE]

Figure AIV.6: The boreal summertime AZM defined by June-July-August box-averaged SST anomalies over the ATL3 region (3ºS-3ºN, 0º-20ºW, cyan box in a) or estimated as the leading EOF over the tropical Atlantic Ocean (the region denoted by the black box in a) for 1958-2019 using ERSSTv5. (a) SST anomalies regressed onto the ATL3 time series, which is shown in (b) as red and blue bars, while the black curve represents the leading principal component timeseries. Explained variance and correlation between indices are given in the legend in (b). (c) Same as (a) but for land SAT and 10-m level wind (arrows; based on JRA-55 for 1958-2019) anomalies. (d) Same as (a) but for precipitation anomalies (shading based on GPCC for 1958-2016 and contours based on CMAP for 1979-2019 for every 0.2 mm/day). On maps, no-overlay indicates regions where the regressions are significant based on t-test accounting for false detection rate at 10% and crosses indicates no significance. Significance for CMAP precipitation is materialized by red contours in (d). All fields have been linearly detrended prior to computation.

[END FIGURE AIV.6 HERE]

[START FIGURE AIV.7 HERE]

Figure AIV.7: The boreal summertime AMM defined by June-July-August standardized SST difference between the north (5ºN-30ºN, 20ºW-60ºW) and south (5ºN-20ºS, 5ºE-25ºW) tropical Atlantic Ocean shown by the

ACCEPTED VERSION SUBJECT TO FINAL EDITING

cyan boxes in (a) or estimated as the leading EOF over the tropical Atlantic Ocean (the region denoted by the black box in a) for 1958-2019 using ERSSTv5. (a) SST anomalies regressed onto the AMM time series, which is shown in (b) as red and blue bars, while the black curve represents the leading principal component timeseries. Explained variance and correlation between indices are given in the legend in (b). (c) Same as (a) but for land SAT and 10-m level wind (arrows; based on JRA-55 for 1958-2019) anomalies. (d) Same as (a) but for precipitation anomalies (shading based on GPCC for 1958-2016 and contours based on CMAP for 1979-2019 for every 0.2 mm/day). On maps, no-overlay indicates regions where the regressions are significant based on t-test accounting for false detection rate at 10% and crosses indicates no significance. Significance for CMAP precipitation is materialized by red contours in (d). All fields have been linearly detrended prior to computation.

[END FIGURE AIV.7 HERE]

AIV.2.5.2 Teleconnections and regional influence

The tropical Atlantic variability has robust teleconnections with climate variability across the global tropics and beyond. There is evidence for two-way teleconnections between the tropical Atlantic and Pacific on interannual to decadal timescales such that the tropical Atlantic variability responds and feeds back to the Pacific ENSO (Section AIV.2.3) and Pacific Decadal Variability (Section AIV.2.6). A number of studies suggest the existence of a possible connection between the tropical North Atlantic and tropical Pacific variability (Wu et al., 2007; Ham et al., 2013a, 2013b; Wang et al., 2017b) at interannual timescales. This teleconnection appears to be modulated at decadal timescale by the AMV phases (Wang et al., 2017b) and it is also affected by global warming (Dong and Zhou, 2014).

The AZM-related boreal summer variability is linked with ENSO in the following boreal winter (Polo et al., 2008; Rodríguez-Fonseca et al., 2009; Ding et al., 2012; Keenlyside et al., 2013; Martín‐Rey et al., 2015; Cai et al., 2019). This relationship is strongest during negative AMV phases due to enhanced equatorial Atlantic variability (Martín-Rey et al., 2014, 2018; Polo et al., 2015). On the other hand, the persistence of SST anomalies during multi-year ENSO events affects the equatorial Atlantic variability through modifications of the Walker circulation (Tokinaga et al., 2019). An exhaustive analysis of the AZM characteristics and related teleconnections is given by Lübbecke et al. (2018b) and by Cabos et al. (2019).

The AZM affects the Indian summer monsoon (ISM), altering the ENSO-ISM connection (Kucharski et al., 2007, 2008; Wang et al., 2009; Barimalala et al., 2012, 2013; Kucharski and Joshi, 2017). Specifically, warm SST in the equatorial Atlantic leads to decreased monsoon rainfall over central India, and the opposite occurs for negative Atlantic SST anomalies via strengthening of the Somali Jet and low-level convergence (Kucharski et al., 2007, 2008; Pottapinjara et al., 2016). This relationship opens to predictive perspective of the ISM rainfall based on AZM phases (Sabeerali et al., 2019). In this framework, the AZM modulates SST variability in the Indian Ocean (Kajtar et al., 2017). The number of monsoon depressions over the Bay of Bengal increases during the cold phase of the AZM, which is remotely responsible for changes in low-level cyclonic vorticity and mid-tropospheric humidity (Pottapinjara et al., 2014). A relationship between AZM and the West African monsoon is documented as well, with reduction of rainfall over the Sahel and increase over Guinea (Losada et al., 2010). But the relationship with the Sahel shows significant changes across the 20th century (Joly and Voldoire, 2010; Losada et al., 2012), which is strongly indicative for non-stationarity of the teleconnection.

On the western side of the basin, a warm equatorial Atlantic delays the northward migration of the ITCZ and can thus influence rainfall over northeastern South America (Nobre and Srukla, 1996), even before the peak of the AZM (Losada et al., 2010; Mohino et al., 2011; Martín-Rey et al., 2018). When the Atlantic and Pacific basins act together, the response over northeastern South America is found to be strongly enhanced (Torralba et al., 2015). In the extratropics, the decaying phase of the AZM in boreal fall can modify the atmospheric circulation over Europe via a circum-global teleconnection pattern (Haarsma and Hazeleger, 2007; García-Serrano et al., 2011), and can remotely affect the NAO (Drévillon et al., 2003; Peng et al., 2005). AZM can also increase precipitation over southern Europe and the Mediterranean Sea during boreal summer through extra-tropical Rossby waves (Losada et al., 2012).

ACCEPTED VERSION SUBJECT TO FINAL EDITING

The fluctuation of the meridional SST gradient in the tropical Atlantic modulates the seasonal march of the ITCZ, thus influencing regional rainfall over northeast Brazil and Sahel (Hastenrath and Heller, 1977; Folland et al., 1986; Foltz et al., 2012). During a negative phase of the AMM, northerly wind anomalies are associated with a southward shift of the ITCZ (Cabos et al., 2019). During boreal spring, warmer SST over the tropical North Atlantic modulate winds over the western Indian Ocean and may strengthen the monsoon circulation over India, affecting the continental rainfall (Vittal et al., 2020). The AMM is also well known to affect the Atlantic hurricane activity (Vimont and Kossin, 2007; Patricola et al., 2014) and tropical cyclones over the western North Pacific (Zhang et al., 2017).

AIV.2.5.3 Available proxy-based reconstruction

Only a few paleo-reconstructions of AMM and AZM are available. Interhemispheric cross-equatorial SST gradients linked to changes in ITCZ locations characteristic of the AMM has been found during LGM, Heinrich Stadial 1 and the mid-Holocene (McGee et al., 2014). Similarly, the dipole-like SST pattern in the South Atlantic subtropics, which is related to the AZM (Lübbecke et al., 2018; Foltz et al., 2019), has been reconstructed with SST proxies from marine sediment cores during the past 12 kyr (Wainer et al., 2014).

Evidence from proxies associated with the AZM and AMM is assessed in Section 2.4.4.

AIV.2.6 Pacific Decadal Variability

AIV.2.6.1 Definition of the mode

The Pacific Decadal Variability (PDV) describes the large-scale fluctuations typically observed beyond ENSO timescales in a variety of instrumental records and proxy reconstructions over the entire Pacific Ocean and surrounding continents.

Historically, climate variability of the Pacific Ocean on timescales longer than 8-10 years has been described in terms of statistical modes, usually assessed through the decomposition into EOFs of the SST over oceanic sub-basins. The leading EOF mode of SST decadal variability in the extratropical North Pacific is called the Pacific Decadal Oscillation (PDO, Mantua et al., 1997; Mantua and Hare, 2002). The PDO is recognized to correspond to a collection of multiple processes (Newman et al., 2016). On interannual-to-decadal timescales, the PDO is thought to be driven by atmospheric forcing linked to stochastic changes in the Aleutian Low integrated by ocean mixed layer dynamics and related re-emergence processes, as well as to ENSO-forced teleconnections (Schneider and Cornuelle, 2005; Nidheesh et al., 2017). On decadal-to-interdecadal timescales, subpolar-subtropical gyre dynamics and related zonal advection of temperature anomalies in the Kuroshio-Oyashio extension and westward-propagating oceanic Rossby waves are thought to be key mechanisms (Qiu et al., 2007; Taguchi et al., 2007; Wills et al., 2019).

The PDO's South Pacific counterpart, called the South Pacific Decadal Oscillation (SPDO; Chen and Wallace 2015) is defined as the leading EOF mode of SST in the extratropical South Pacific. As for the PDO, the SPDO is thought to be driven by internal climate variability associated with extratropical atmospheric modes (e.g. SAM, Section AIV.2.2), ENSO teleconnections (Section AIV.2.3) and ocean dynamics through gyre circulation (Shakun and Shaman, 2009; Zhang et al., 2018).

In the tropical Pacific, while ENSO has a clear interannual spectral peak, decadal variability is also present with a similar spatial structure (Zhang et al., 1997), called tropical Pacific Decadal Variability (TPDV) or decadal ENSO. Relative occurrence of El Niño and La Niña events in a given decade correlates with the phase of the TPDV (Power and Colman, 2006).

Despite the PDO, SPDO and TPDV being considered to be physically distinct modes (Newman et al., 2016), they are highly correlated in observations (Chen and Wallace 2015) and they collectively constitute an equatorially symmetric pattern of basin-wide variability, often called the Interdecadal Pacific Oscillation

ACCEPTED VERSION SUBJECT TO FINAL EDITING

(IPO) (Power et al., 1999; Folland et al., 2002; Henley et al., 2015). There is evidence that ENSO and the TPDV drive the PDO and SPDO in the North and South Pacific through tropical-extratropical teleconnections and the "reddening" (i.e. selective retainment of decadal and longer variability) in the ocean, ensuring the synchronization of decadal variability in both hemispheres (Newman et al., 2016). Besides, positive feedbacks are suggested between the TPDV and the extratropical North Pacific through the Pacific Meridional Mode (Stuecker, 2018), which is the Pacific analogue of the AMM (Section AIV.2.5; Chiang and Vimont, 2004), and modulations of the shallow subtropical cell of the Pacific ocean circulation (Farneti et al., 2014).

Whether the IPO is a distinct mode of climate variability (Henley et al., 2017) or not (Tung et al., 2019) remains to be further assessed and clarified. However, since the PDO, SPDO, TPDV and IPO modes are highly correlated both spatially and temporally, they can be referred collectively as the Pacific Decadal Variability mode (PDV; Henley 2017b; Liu and Di Lorenzo 2018), similarly to the Atlantic (Section AIV.2.7). Besides, it is noteworthy that none of these modes are actually oscillations with clear spectral peaks in the instrumental period (Mann et al., 2020), which advocates for the use of the PDV acronym across the report.

De facto, there is no unique way to assess the PDV. It can be extracted from the IPO, defined as the leading EOF mode of decadal low-pass filtered SST variability over the entire Pacific to remove the overwhelming influence of ENSO at interannual timescales. Henley et al. (2015) introduced the tripole index (TPI) as the difference of SST anomalies between an equatorial Pacific domain (10ºS-10ºN, 170ºE-90ºW) and an average of midlatitude North (25ºN-45ºN, 140ºE-145ºW) and South (50º-15ºS, 150ºE-160ºW) Pacific domains (Figure AIV.8a). Section 2.4.5 describes the changes in the PDV phases over the instrumental record using a variety of SST products.

A positive phase of the PDV is characterized by warm conditions in the central-eastern tropical Pacific from the dateline to the coasts of the Americas, encircled to the west in the midlatitudes by negative SST anomalies forming a so-called horseshoe pattern. The pattern has a certain similarity with ENSO and related anomalous SST fingerprints through atmospheric teleconnections. However, the PDV features meridionally broader SST anomalies in the tropical Pacific extending to the subtropics compared to ENSO, and relatively stronger extratropical SST anomalies. Alternatively, the low-pass filtered SST regression on the PDO index defined as the leading principal component of SST (Mantua et al., 1997) or sea surface height (Di Lorenzo et al., 2008) over the extratropical North Pacific north of 20ºN are used in literature for PDV. Their corresponding spatial patterns are, by definition, weighted to the respective hemisphere of the Pacific. Figure AIV.8b provides evidence that they are all highly correlated to each other. The correlation value between TPI and the PDO index is equal to 0.76, and when low-pass filtered, it is greater than 0.9 for all the combination of indices.

In the following, and in Section 3.7.6 evaluating the model performance in reproducing PDV and assessing the human influence on the mode evolution, the TPI index is preferred. The latter definition is found to be less sensitive than classical EOF analysis to the possible interplay between internal processes that intrinsically drive the PDV (Wills et al., 2018) and the externally-forced SST response simulated in historical simulations. There is no unique way to remove the impact of the external forcing in the observations at decadal to multidecadal timescales, and the chosen method may have significant implications for the interpretation of the PDV expression during the instrumental era.

Since AR5, there has been considerable progress in the understanding of PDV itself but also in its critical role in modulating the evolution of observed global surface temperature (Cross-Chapter Box 3.1) as well as regional climate through teleconnections. On interannual time scales, ENSO is the leading internal driver of global surface tempeature variability (Section AIV.2.3). Since PDV encompasses decadal modulations of El Niño versus La Niña occurrences, PDV affects global surface tempeature on decadal timescales, with its positive and negative phases tied to higher and lower global surface tempeature, respectively. Indeed, studies identify PDV as the leading mode of variability associated with unforced decadal global surface tempeature fluctuations in observations and a majority of CMIP5 models (Brown et al., 2015; Dai et al., 2015), with additional influence from Atlantic Multidecadal Variability (AMV, Section AIV.2.7) (Tung and Zhou,

ACCEPTED VERSION SUBJECT TO FINAL EDITING

2013). PDV thus plays an important role in decadal acceleration and slowdown of global surface tempeature trends (Cross-Chapter Box 3.1). So far, little predictability has been found for decadal PDV, despite its global relevance and decadal prediction in the Pacific remains challenging with the current decadal forecast system (Section 4.4.3.5). Finally, there is an increasing body of evidence about the existence of a network of teleconnections related to decadal climate variability phenomena (Cassou et al., 2018; Cai et al., 2019). For instance, AMV has been hypothesized to influence in part the phase of the PDV (McGregor et al., 2014; Ruprich-Robert et al., 2017) and consistently, there is a significant negative correlation between PDV and AMV. Other studies suggest that the PDV may be the main driver of the decadal IOB and IOD modes (Section AIV.2.4), while influence from the Indian Ocean SST on PDV has been also suggested (Luo et al., 2012; Mochizuki et al., 2016).

The temporal evolution of PDV in the instrumental records and its model representation are assessed in Sections 2.4.5 and 3.7.6, respectively. Skill in predicting near-term temporal evolution of the PDV and mid- to long term PDV changes are assessed in Sections 4.4.3.5 and 4.5.3.5, respectively.

[START FIGURE AIV.8 HERE]

Figure AIV.8: The PDV based on TPI for 1900-2014 after 10-year low-pass filtering. (a) SST anomalies regressed onto TPI based on ERSSTv5. The cyan boxes indicate regions for the TPI definition. (b) Temporal evolution of the raw TPI (bars), the 10-year low-pass filtered TPI (cyan curve), the EOF-based PDO index (dashed black) and two estimations of the IPO EOF-based indices. In solid black, linear detrending is applied to annual data prior to the computation of the EOF of the low-pass filtered SST to remove the forced component in the SST field. In orange, the forced signal is estimated from CMIP5 historical simulations following Ting et al. (2009). The latter metric is used in CMIP6 DCPP-C sensitivity experiments (Boer et al. 2016). The correlation between the low-pass filtered TPI and all PDV indices is given in the legend. (c) Same as (a) but for land SAT (shading; based on BerkeleyEarth for 1900-2014) and 10-m level wind (arrows; based on JRA-55 for 1958-2014) anomalies. (d) Same as (a) but for precipitation anomalies (shading based on GPCC for 1900-2014). All are based on annual mean. On maps, no-overlay indicates regions where the regressions are significant based on t-test accounting for false detection rate at 10% and crosses indicates no significance.

[END FIGURE AIV.8 HERE]

AIV.2.6.2 Teleconnections and regional influence

Due to the similarity of the SST anomaly pattern with ENSO in the tropical Pacific, atmospheric teleconnections associated with the PDV are rather similar to those of ENSO but with a longer temporal expression. This includes the long-term alteration of the Walker circulation, the modification of the extratropical background driven by tropically-forced Rossby waves then favouring particular phases of the Pacific-North American (PNA) and Pacific-South American (PSA) patterns of atmospheric internal variability that are responsible for persistent influences over the continents (e.g. persistent drought over California and Australia, etc.). Those atmospheric patterns imprint a PDO-like and SPDO-like SST patterns with a reddening by the extratropical oceans, forming the pan-Pacific SST anomaly pattern of the PDV as described above (Newman et al., 2016; Henley, 2017; Liu and Di Lorenzo, 2018).

A positive phase of the PDV brings anomalously warm conditions in the northwestern corner of North America, with maximum loading over Alaska linked to reinforced and eastward displaced Aleutian Low and related anomalous southerlies (Figure AIV.8c). In contrast, concurrent cold conditions dominate far-eastern Siberia due to strengthened advection of Arctic air. The tail end of the storm track is strengthened leading to more precipitation along the Pacific coast of North America, especially in boreal winter. A positive PDV also induces a cooler and wetter climate in the southern part of the North American continent, with the wet anomalies being the most pronounced in boreal summer (Figure AIV.8d). The negative phase of the PDV is an important cause of droughts in the western and central United States (Dai, 2013). Besides the direct

ACCEPTED VERSION SUBJECT TO FINAL EDITING

influence of atmospheric teleconnections from the tropical branch of the mode, extratropical SST anomalies have been shown to modulate the amplitude of the precipitation anomalies in North America (Burgman and Jang, 2015).

In the tropics, a positive PDV is associated with warm and dry anomalies in the Maritime Continent and Amazon (Meehl and Teng, 2014; Figure AIV.8c,d). The Indian and African monsoons also tend to weaken (Meehl and Hu, 2006; Figure AIV.8d). Warm and dry anomalies also cover most of Australia while wet anomalies dominate in South America south of 15ºS. In particular, a positive PDV increases drought risk in Australia (Power et al., 1999; Vance et al., 2015). In the oceans, a positive PDV increases the occurrence of marine heat waves in the Bering Sea and subtropical Eastern Pacific, while a negative PDV increases ocean heat waves in the Kuroshio-Oyashio extension, Melanesia and over the tropical Indian Ocean (Holbrook et al., 2019). PDV also modulates tropical cyclone activity: a positive PDV increases tropical cyclone genesis over the Philippine Sea and the tropical eastern North Pacific and decreases it over the tropical North Atlantic and western South Pacific (Grant and Walsh, 2001; Liu and Chan, 2008; Li et al., 2015; Zhao et al., 2018, 2020). PDV, together with ENSO, have been shown to control part of the interannual to multidecadal wildfire variability, PDV-related persisting droughts and severe heatwave acting as preconditioning in many regions (see for instance Kitzberger et al., 2007; Ward et al., 2016).

Implications of PDV on water cycle changes are further assessed in Sections 8.3.2.4 and 8.4.2.4. Section 10.4 highlights the importance of PDV in regional climate change attribution, with an example in Section 10.6. Influence of PDV climate anomalies in specific regions, including extremes, are assessed in Sections 11.3, 11.4, 11.6, 11.7, Atlas.4, Atlas.5, Atlas.7 and Cross-Chapter Box Atlas.2. Its implications for ocean circulation and sea levels are assessed in Sections 9.2 and 9.6.

AIV.2.6.3 Available proxy-based reconstruction

PDV reconstructions have been developed with tree rings in North America and Asia (Biondi et al., 2001; D'Arrigo et al., 2001; Gedalof and Smith, 2001; MacDonald and Case, 2005; D'Arrigo and Wilson, 2006; D'Arrigo and Ummenhofer, 2015; Buckley et al., 2019), corals in the Pacific (Linsley et al., 2015; Williams et al., 2017) and Indian Ocean (Crueger et al., 2009), historical documents in China (Shen et al., 2006), ice cores (Vance et al., 2015), and multiproxy approaches (Verdon and Franks, 2006; Mann et al., 2009; McGregor et al., 2010) covering the past several centuries up to a millennium. Comparing 12 of these reconstructions, it has been found that respective correlations are generally low (Henley, 2017b), indicating large uncertainty in the PDV temporal history before instrumental records. On longer timescales, a variety of proxies consistently capture the variations of the Aleutian Low intensity throughout the Holocene, which can be used to reconstruct the PDV (see Section 2.4.5).

AIV.2.7 Atlantic Multidecadal Variability

AIV.2.7.1 Definition of the mode

The Atlantic Multidecadal Variability (AMV) describes the large-scale slow fluctuations observed from one decade to the next in a variety of instrumental records and proxy reconstructions over the entire North Atlantic Ocean and surrounding continents. Fingerprints of the AMV can be found at the surface ocean, which is characterized by swings in basin-scale SST anomalies reflecting the interaction with the atmosphere, with a nominal period in the order of 70 years (Deser et al., 2010). AMV markers can be also tracked at the subsurface ocean in terms of heat content and density anomalies. The latter have been traditionally linked to the low-frequency fluctuations in the Atlantic Meridional Overturning Circulation (AMOC) and related oceanic meridional heat/salinity transport and water masses formation through deep convection in the Subarctic Seas (Zhang, 2017).

The positive phase of the AMV is characterized by anomalous warming over the entire North Atlantic, with the strongest amplitude in the subpolar gyre and along sea-ice margin zones in the Labrador Sea and

ACCEPTED VERSION SUBJECT TO FINAL EDITING

Greenland/Barents Sea (approximately +0.5ºC) and in the subtropical North Atlantic basin to a lower extent (Figure AIV.9a). Concurrent, albeit weaker, anomalous cooling is found over the South Atlantic but also along the Pacific cold tongue sandwiched by warmer SST, a pattern reminiscent of the PDV (Section AIV.2.6). What stands out is the apparent inter-basin connectivity in AMV related SST anomalies, which is strongly indicative of the existence of a network of teleconnections linking neighbouring ocean basins, the tropics and the extra tropics, including Northern Hemisphere polar regions, and the oceans and land regions (Cassou et al., 2018). The AMV, together with the PDV, has been shown to modulate the observed time-evolving global surface temperature on multidecadal timescales since pre-industrial time (Cross-Chapter Box 3.1), whilst the level of their respective influence remains difficult to quantify because of their inter-connectivity (Tung and Zhou, 2013; Wu et al., 2019; Li et al., 2020).

The term "Atlantic Multidecadal Oscillation" (AMO) has been introduced in the literature (Kerr, 2000) and used in previous IPCC reports to describe this phenomenon and in particular to make the distinction with the so-called North Atlantic tripole pattern connected to the NAO (Section AIV.2.1) at interannual timescales (Enfield et al., 2001). However, since the observed slow variations of the North Atlantic SSTs consist of a broad band of low-frequency signals (Zhang, 2017; Sutton et al., 2018) rather than a single preferred timescale, as also confirmed from last-millennium reconstructions (e.g., Singh et al., 2018), the denomination "Atlantic Multidecadal Variability" wherein a distinct oscillatory timescale is less clearly implied, appears more appropriate to describe decadal climate variability phenomena as also suggested for the Pacific (Section AIV.2.6). The term AMV will be accordingly used subsequently and throughout the entire report.

The observed AMV is interpreted as the regional residual imprint in SST anomalies after removal of the externally-forced signal. There is no unique and preferred way to remove the impact of external forcing in observations. Linear detrending is used in the traditional definition of the AMV index, which corresponds to the average over the entire North Atlantic basin of the linearly detrended SST yearly anomalies on which a 10-year running mean is applied, as proposed by Enfield et al. (2001). To remove the residual nonlinear global-scale signal from the North Atlantic mean SST, different approaches have been proposed either based on observations applying specific statistics (e.g., Trenberth and Shea, 2006; Frajka-Williams et al., 2017; Frankignoul et al., 2017; Sutton et al., 2018; Yan et al., 2019) or based on model estimates of the externally-forced signal including both natural (solar and volcanoes) and anthropogenic (greenhouse gases and aerosols) influence assessed from historical simulations (Ting et al., 2009; Terray, 2012; Steinman et al., 2015; Tandon and Kushner, 2015). More specifically, in Trenberth and Shea (2006), the annual observed global-mean SST anomaly timeseries is subtracted from the observed annual North Atlantic spatially averaged timeseries to obtain the raw unfiltered AMV index. In Ting et al. (2009), a signal-to-noise maximizing EOF analysis is applied to global annual mean SSTs derived from the CMIP5 multi-model ensemble to extract an estimation of the forced component, which is a priori removed before computation of the AMV index, then defined as a low-frequency residual. The latter technique has been retained in the so-called CMIP6 DCPP-C sensitivity experiments (Boer et al., 2016) aimed at furthering a better understanding of the teleconnections associated with the AMV. The two latter indices are shown in Figure AIV.9b and compared to the traditional AMV index.

All AMV timeseries consistently show a few distinct phases over the approximately 120-year instrumental record, namely warm periods over 1930-1965 and since 1995, and cool periods between 1900 and 1925 and over 1965-1995 (Figure AIV.9b). The uncertainty introduced by the different definitions of the index is mainly related to the strength of the phase of the AMV and in particular the most recent ones, which are the most sensitive to the estimation of the externally-forced signal.

The temporal evolution of AMV in the instrumental records is assessed in Section 2.4.6. The transition between phases has been shown to involve various atmospheric and oceanic processes, leading to some predictability, but also influences from external forcing (both anthropogenic and natural), whose respective weight and interplay remain outstanding issues, as assessed in detail in Section 3.7.7 and Section 9.2.3.

ACCEPTED VERSION SUBJECT TO FINAL EDITING

[START FIGURE AIV.9 HERE]

Figure AIV.9: The AMV based on the AMV index defined from Trenberth and Shea (2006) for 1900-2014 after 10-year low-pass filtering. The index corresponds to the annual SST averaged over the North Atlantic domain (cyan box) minus near-global average [60ºN-60ºS]. (a) SST anomalies regressed onto the AMV index based on ERSSTv5. (b) The cyan curve indicates the 10-year low-pass filtered AMV index shown in bars. The orange curve stands for the AMV index used for the CMIP6 DCPP-C sensitivity experiments (Boer et al. 2016). (c) Same as (a) but for land SAT (shading; based on BerkeleyEarth for 1900-2014) and 10-m level wind (arrows; based on JRA-55 for 1958-2014) anomalies. (d) Same as (a) but for precipitation anomalies (shading based on GPCC for 1900-2014). All is based on annual mean. On maps, no-overlay indicates regions where the regressions are significant based on t-test accounting for false detection rate at 10% and crosses indicates no significance.

[END FIGURE AIV.9 HERE]

AIV.2.7.2 Teleconnections and regional influence

The important role of the AMV in observed low-frequency climate signals at a regional scale has been recognized for decades. The AMV is a key driver of temperature and precipitation anomalies along the North Atlantic surrounding continents but also remotely through global atmospheric teleconnections (e.g. monsoons). Considering AMV-induced regional influence is crucial because the AMV acts as a pronounced modulator of the impacts driven by external natural and anthropogenic forcings. For instance, the AMV can have a pronounced fingerprint in time-integrating processes, such as river flows, and could explain the largest fraction of observed variance in some specific local areas since the 1900s (e.g. Bonnet et al., 2020). It is thus a key phenomenon for regional-scale or process-based attribution of past observed climate variations as introduced in Cross-Chapter Box 1.4 and extensively developed in Section 10.4.1.

Positive AMV is associated with much warmer conditions over the north-western corner of the Atlantic, with marked positive anomalies on land around the Labrador Sea (Figure AIV.9c). There is a strong seasonality in the AMV teleconnection and this pattern is mostly explained by boreal winter atmospheric dynamics and a local reduction of sea-ice formation. There is a large-scale decrease of the wintertime midlatitude westerlies and, concurrently, a weakening of the trade winds in the North Atlantic tropical basin, which is reminiscent of a negative phase of the NAO (Peings and Magnusdottir, 2014; Gastineau and Frankignoul, 2015). Over Europe, AMV-related signals are weak on yearly average (Figure AIV.9c) but mask a pronounced seasonality of the teleconnection as well as some interplay between dynamical (i.e. atmospheric circulation) versus thermodynamical changes controlled by the AMV (O'Reilly et al., 2017; Ruprich-Robert et al., 2017, Qasmi et al. 2020). Summer tends to be warmer during positive AMV in Europe (Sutton and Dong, 2012; Nicolì et al., 2020) with constructive contribution of both dynamical and thermodynamical responses while destructive interference prevails in boreal winter leading to colder conditions with a reinforced occurrence of blocking (Rimbu et al., 2014; Davini et al., 2015) and a southward shift of the jet (Simpson et al., 2018). Anomalies are positive all year round over a broad Mediterranean region, including North Africa and the Middle East. Reduction of Arctic Sea Ice is also found during positive AMV with local warming extension over the adjacent polar land (Day et al., 2012; Yu et al., 2017; Castruccio et al., 2018).

In terms of precipitation (Figure AIV.9d), positive AMV is associated with a northward shift of the Atlantic ITCZ in response to changes in the meridional SST gradient with respect to the equator (Martin and Thorncroft, 2014; Friedman et al., 2017; Green et al., 2017). The AMV influence is the strongest in the boreal summer affecting the West African Monsoon, leading to reinforced Sahel rainfall, and wetter conditions in the Caribbean basin through the modulation of the occurrence of hurricanes (Dunstone et al., 2011; Hermanson et al., 2014). By contrast, dry conditions prevail in the Northeast Brazil and in the south-eastern corner of South America as well as in the Great Plains in North America. The signal of the positive AMV lead to an intensified precipitation and river runoff over Northern Eurasia (Nicolì et al., 2020) and controls the multidecadal variations in river flows over much of Europe (Boé and Habets, 2014; Hodgkins et al., 2017). Because of global teleconnections, especially in the tropics, the AMV also affects the other

ACCEPTED VERSION SUBJECT TO FINAL EDITING

monsoon systems with signals found over India, South East Asia, and the Maritime Continent and, more broadly, over the entire tropical Pacific (Chylek et al., 2014; Kucharski et al., 2016; Ruprich-Robert et al., 2017).

The weight of the AMV in observed low-frequency variations is assessed in detail in Section 10.4.2 for specific regional case studies, including the sectors listed above. Because of its long timescale due to persistent heat content anomalies, the AMV can be considered as a potential source of near-term climate predictability. Skill of the current decadal forecast systems in predicting the AMV temporal evolution and associated teleconnection at various lead time is assessed in Section 4.4.3.6, while long-term changes are assessed in Section 4.5.3.6.

AIV.2.7.3 Available proxy-based reconstruction

Paleoclimate reconstructions of AMV-related signals have been developed using terrestrial, marine and ice-core proxies. The AMV reconstruction in the last 1200 years by Wang et al. (2017a), using terrestrial proxy records, shows a clear broad band of enhanced spectral power at multidecadal timescales but no evidence of a distinct multidecadal or centennial spectral peak (Singh et al., 2018). This is largely consistent with the record of the instrumental period and with previous proxy-based studies (Gray et al., 2004; Mann et al., 2009) in the overlapping periods. Studies focusing on marine proxies also show persistent multidecadal variability over the last three centuries (Kilbourne et al., 2014; Svendsen et al., 2014; Moore et al., 2017). Multidecadal Arctic temperature variability related to the AMV is also evident in ice cores records over the last millennium (Chylek et al., 2011; Zhou et al., 2016) and beyond (Knudsen et al., 2011). High resolution sedimentary records from the Arctic were recently analyzed to reconstruct the AMV over the last 2900 years (Lapointe et al., 2020). However, this new reconstruction refers to the raw North Atlantic SST variability rather than to the residual of the Atlantic signal obtained after removal of the estimation of the external forcing influence. A multi-perspective assessment of the North Atlantic variability is thus necessary for understanding the origin of the AMV, its physics and its climatic implications over the paleoclimatic period.

The temporal evolution of the AMV is described and assessed in detail in Section 2.4.6.

AIV.2.8 Madden-Julian Oscillation

AIV.2.8.1 Definition of the mode

The Madden-Julian Oscillation (MJO) is the leading mode of tropical intra-seasonal variability with 20–90 days' timescale (Madden and Julian, 1994) and an important source of regional climate variability and predictability across the globe at subseasonal timescales from a week to months (Madden and Julian, 1994; Zhang, 2005; Vitart, 2017; Wheeler et al., 2017; Kim et al., 2018). It is characterized by planetary-scale disturbances (zonal wavenumber 1–3) of pressure, wind, clouds and rainfall moving predominantly eastward along the equator at average speed of 5 m s^{-1} (Roxy et al., 2019). More precisely, the MJO is characterized by alternating regions of suppressed and enhanced convection coupled to an anomalous zonal overturning circulation of the atmosphere (Zhang, 2005). The MJO is driven by internal ocean-atmosphere processes that occur all year round but exhibits prominent seasonality with more pronounced signals in boreal winter. During boreal summer, centres of convective activity associated with the MJO are shifted away from the equator to 10ºN–20ºN and propagate northward in the Asian monsoon region (Yasunari, 1980; Madden, 1986) in addition to eastward propagation, often called as the boreal summer intra-seasonal oscillation (BSISO; Madden, 1986; Kikuchi et al., 2012). Whereas the MJO is considered present in all seasons, albeit with weaker amplitude in boreal summer, the BSISO tends to prevail during boreal summer, with influences on monsoons, tropical cyclones and other water cycle aspects (Kikuchi et al., 2012; Lee et al., 2013).

The real-time multivariate MJO (RMM) index has been widely used to detect the MJO, based on the first two combined EOF modes of daily outgoing longwave radiation (OLR) and zonal winds at 850 and 200 hPa averaged over 15°N-15°S (Wheeler and Hendon, 2004). The OLR represents convective activity and zonal

ACCEPTED VERSION SUBJECT TO FINAL EDITING

winds at the lower and upper troposphere depict the overturning zonal circulation along the equator. The composite maps of convective activity and atmospheric circulation (Figure AIV.10a) and the phase diagram (Figure AIV.10b) based on eight phases constructed by the two PCs timeseries provide effective ways to understand and monitor spatial and temporal evolution of the MJO event. In general, the MJO disturbance are initiated in the equatorial western Indian Ocean and travel eastward mainly over the Indo-Pacific warm pool region. However dynamical fields in composite maps indicate that the MJO also propagates over climatological non-convective regions (e.g., the eastern Pacific, part of the tropical Atlantic) (Figure AIV.10a), then manifesting the planetary nature of the tropical intra-seasonal oscillation (Cassou, 2008). Each phase has a nominal persistence of about 7-8 days and the anti-clockwise rotation in this 2-dimensional diagram materializes the propagation of the MJO packets from west to east. Figure AIV.10b provides an example of that RMM index computed for the year 1997, with months highlighted in colours. When the value of the index lies in the centre of the diagram, the MJO is considered to be inactive; outside the circle, its distance from the centre quantifies the amplitude and spatial coherence of the MJO episode.

The evaluation of the MJO in climate models is done through phenomenological (Waliser et al., 2009) and process-oriented (Xavier, 2012) diagnostics. MJO simulation remains a challenge in both CMIP3 and CMIP5 models, even though overall improvements have been reported in the most recent model versions (Waliser et al., 2003; Lin et al., 2006; Sperber and Annamalai, 2008; Kim et al., 2009; Xavier et al., 2010; Jiang et al., 2016). Poor MJO simulation in coupled climate models has been attributed to many factors, including an insufficient build-up of atmospheric moisture for large-scale organized convection to occur (Kim et al., 2012; Mizuta et al., 2012), biases in models mean state (Inness et al., 2003; Hannah et al., 2015; Kim, 2017), coupling frequency with the ocean and representation of air-sea interactions (Bernie et al., 2008; DeMott et al., 2015). In CMIP5 simulations, the eastward propagation of boreal winter MJO convection from the Indian Ocean into the western Pacific (Hung et al., 2013) and the northward propagation during boreal summer (Sperber et al., 2013) are slightly better represented, even if major biases persist and still affect the monsoon systems. These improvements have been attributed to advances in parametrizing moist turbulence and convection (Hohenegger and Bretherton, 2011; Mapes and Neale, 2011; Del Genio et al., 2012; Kim et al., 2012; Hourdin et al., 2013), leading to greater MJO predictive skill of up to four weeks in operational subseasonal prediction centres (Vitart, 2014). Super-parametrized models (Benedict and Randall, 2009), global cloud system-resolving models (Miyakawa et al., 2014) and high-resolution global climate models with an improved seasonal cycle (Mizuta et al., 2012) have been shown to produce a more realistic simulation of the MJO. Progresses in the representation of the MJO across model generations are assessed in Section 1.5.4.6 and Section 8.3.2.9.1.

The assessment of changes in the MJO and related processes, mostly in terms of its implication for water cycle changes in the recent past and in future projections is provided in Sections 8.3.2.9 and 8.4.2.9, respectively. The MJO influence over south East Asia and Central and South America is further assessed in Sections Atlas.4, Atlas.5, Atlas.7, and Cross-Chapter Box Atlas.2.

[START FIGURE AIV.10 HERE]

Figure AIV.10: (a) The spatio-temporal properties of the MJO. Daily composites of Outgoing Longwave Radiation (OLR, W m^{-2}, shaded) anomalies and streamfunction anomalies at 300 hPa (STF, contours every 0.5 10^6 m^2 s^{-1}) for the 8 MJO phases in boreal winter (1st Dec. -31st March) based on NOAA interpolated satellite products and NCEP-NCAR reanalyzes over 1979-2019, respectively. Greenish (brownish) colours indicate enhanced (reduced) convective activity associated with wet (dry) conditions. Solid (dashed) contours show for positive (negative) STF anomalies which stand for anomalous anticyclonic circulation in the Northern (Southern) Hemisphere. (b) Phase diagram of the MJO constructed from the two leading principal components drawn from empirical orthogonal decomposition of combined wind@300hPa+OLR fields following Wheeler and Hendon (2004) for the winter 2007-2008 chosen as an example of active MJO years. (c) Schematic representation of MJO-related tropical—Northern Hemisphere interactions and teleconnections inferred from observational and numerical studies (adapted from Stan et al.(2017)). Because the interactions and teleconnections of the Southern Hemisphere are not as well understood but SAM, they are not included in the current schematic.

ACCEPTED VERSION SUBJECT TO FINAL EDITING

[END FIGURE AIV.10 HERE]

AIV.2.8.2 Teleconnections and regional influence

In AR5, the MJO has been described as a tropical phenomenon, yet with prominent impacts across the globe through teleconnections. The MJO exerts a strong influence on occurrences of extreme weather events in the tropics, including tropical cyclones, droughts, flooding, heat waves, fires, among others (Zhang, 2013), as well as those in the extratropics via teleconnections (Stan et al., 2017). This has opened new opportunities and scientific endeavours in the emerging field of sub-seasonal to seasonal forecasts of extremes (Vitart and Robertson, 2018) and for the development of new observational networks needed to initialize the forecast systems (Subramanian et al., 2019). The MJO can also impact the atmospheric composition, such as ozone, CO, CO_2, and aerosols (Tian et al., 2007, 2011; Li et al., 2010b; Lau et al., 2012).

The schematic in Figure AIV.10c shows the main regions of influence of the MJO. During boreal winter, the MJO fingerprint is mostly confined to the deep tropics with a zonal alternation of wet and dry zones depending on the MJO phase. For instance, in phase 4, enhanced rainfall is found over the Maritime Continent while suppression of convection is present over the central Pacific, northeast Brazil and equatorial Africa (Figure AIV.10a). The opposite is found during phase 8. Anomalous upper-level divergence in the deep tropics associated with altered convection and diabatic heating leads to anomalous vorticity in the subtropics (shown by streamfunction dipoles straddling the equator in Figure AIV.10a) acting as an efficient and primary source of teleconnections outside the tropics (L'Heureux and Higgins, 2008; Lin et al., 2009; Lukens et al., 2017). The extratropical influence of the MJO may occur via the excitation of forced tropospheric Rossby waves (Ferranti et al., 1990; Matthews et al., 2004; Cassou, 2008; Stan et al., 2017) that affect the climate variability over the North Pacific (Ferranti et al., 1990; Higgins and Mo, 1997), the North Atlantic (Ferranti et al., 1990; Cassou, 2008) and the Arctic (Zhou and Miller, 2005). For example, tropical convective heating associated with MJO phase 5 contributes to Arctic warming, while the opposite occurs for the MJO phase 1 (Yoo et al., 2011, 2012). Phase 2-3 of the MJO is clearly associated with the prevalence of the positive phase of the NAO with a 10 to 15-days lag after the MJO forcing. Stratospheric pathways are also reported to support tropical-extratropical teleconnections though the modified occurrence of sudden stratospheric warming (Liu et al., 2014; Garfinkel and Schwartz, 2017) with a 15 to 20-days delay leading to sub-seasonal predictability.

During boreal summer, the MJO/BSISO convective activities and related impacts propagate northward/northeastward over the Indian Ocean-South Asia region (Yasunari, 1980; Annamalai and Sperber, 2005) and northward/northwestward over the western North Pacific-East Asia region (Kemball-Cook and Wang, 2001; Lee et al., 2013). The MJO/BSISO significantly modulate occurrences of extreme rainfall and heat waves over Asia (Hsu et al., 2016, 2017; Chen and Zhai, 2017; Diao et al., 2018) and North America (Moon et al., 2013; Lee and Grotjahn, 2019). They also regulate tropical cyclone activities in Indian (Frank and Roundy, 2006), Pacific (Maloney and Hartmann, 2000; Diamond and Renwick, 2015; Zhao et al., 2015) and Atlantic (Klotzbach and Oliver, 2015) tropical oceans. They contribute to the intra-seasonal fluctuations of monsoons, including timing of its onset and termination during summer (Maloney and Shaman, 2008; Wheeler et al., 2009; Lee et al., 2013; Grimm, 2019) and its active/break phases (Pohl and Camberlin, 2006; Maloney and Shaman, 2008; Joseph et al., 2009; Lee et al., 2017).

ACCEPTED VERSION SUBJECT TO FINAL EDITING

References

Abram, N. J., Gagan, M. K., Cole, J. E., Hantoro, W. S., and Mudelsee, M. (2008). Recent intensification of tropical climate variability in the Indian Ocean. *Nat. Geosci.* 1, 849–853. doi:10.1038/ngeo357.

Abram, N. J., Gagan, M. K., Liu, Z., Hantoro, W. S., McCulloch, M. T., and Suwargadi, B. W. (2007). Seasonal characteristics of the Indian Ocean Dipole during the Holocene epoch. *Nature* 445, 299–302. doi:10.1038/nature05477.

Abram, N. J., Mulvaney, R., Vimeux, F., Phipps, S. J., Turner, J., and England, M. H. (2014). Evolution of the Southern Annular Mode during the past millennium. *Nat. Clim. Chang.* 4, 564–569. doi:10.1038/nclimate2235.

Abram, N. J., Wright, N. M., Ellis, B., Dixon, B. C., Wurtzel, J. B., England, M. H., et al. (2020). Coupling of Indo-Pacific climate variability over the last millennium. *Nature* 579, 385–392. doi:10.1038/s41586-020-2084-4.

Ait Brahim, Y., Wassenburg, J. A., Sha, L., Cruz, F. W., Deininger, M., Sifeddine, A., et al. (2019). North Atlantic Ice-Rafting, Ocean and Atmospheric Circulation During the Holocene: Insights From Western Mediterranean Speleothems. *Geophys. Res. Lett.* 46, 7614–7623. doi:10.1029/2019GL082405.

Ambaum, M. H. P., Hoskins, B. J., and Stephenson, D. B. (2001). Arctic Oscillation or North Atlantic Oscillation? *J. Clim.* 14, 3495–3507. doi:10.1175/1520-0442(2001)014<3495:AOONAO>2.0.CO;2.

Annamalai, H., Liu, P., and Xie, S.-P. (2005). Southwest Indian Ocean SST Variability: Its Local Effect and Remote Influence on Asian Monsoons*. *J. Clim.* 18, 4150–4167. doi:10.1175/JCLI3533.1.

Annamalai, H., and Sperber, K. R. (2005). Regional Heat Sources and the Active and Break Phases of Boreal Summer Intraseasonal (30–50 Day) Variability. *J. Atmos. Sci.* 62, 2726–2748. doi:10.1175/JAS3504.1.

Ashok, K., Behera, S. K., Rao, S. A., Weng, H., and Yamagata, T. (2007). El Niño Modoki and its possible teleconnection. *J. Geophys. Res. Ocean.* 112, C11007. doi:10.1029/2006JC003798.

Ashok, K., Chan, W.-L., Motoi, T., and Yamagata, T. (2004a). Decadal variability of the Indian Ocean dipole. *Geophys. Res. Lett.* 31, L24207. doi:10.1029/2004GL021345.

Ashok, K., Guan, Z., Saji, N. H., and Yamagata, T. (2004b). Individual and Combined Influences of ENSO and the Indian Ocean Dipole on the Indian Summer Monsoon. *J. Clim.* 17, 3141–3155. doi:10.1175/1520-0442(2004)017<3141:IACIOE>2.0.CO;2.

Ashok, K., Guan, Z., and Yamagata, T. (2001). Impact of the Indian Ocean dipole on the relationship between the Indian monsoon rainfall and ENSO. *Geophys. Res. Lett.* 28, 4499–4502. doi:10.1029/2001GL013294.

Ashok, K., Guan, Z., and Yamagata, T. (2003). Influence of the Indian Ocean Dipole on the Australian winter rainfall. *Geophys. Res. Lett.* 30, 1821. doi:10.1029/2003GL017926.

Ashok, K., and Saji, N. H. (2007). On the impacts of ENSO and Indian Ocean dipole events on sub-regional Indian summer monsoon rainfall. *Nat. Hazards* 42, 273–285. doi:10.1007/s11069-006-9091-0.

Baker, A., C. Hellstrom, J., Kelly, B. F. J., Mariethoz, G., and Trouet, V. (2015). A composite annual-resolution stalagmite record of North Atlantic climate over the last three millennia. *Sci. Rep.* 5, 10307. doi:10.1038/srep10307.

Baker, H. S., Woollings, T., Forest, C. E., and Allen, M. R. (2019). The Linear Sensitivity of the North Atlantic Oscillation and Eddy-Driven Jet to SSTs. *J. Clim.* 32, 6491–6511. doi:10.1175/JCLI-D-19-0038.1.

Baldwin, M. P., and Dunkerton, T. J. (1999). Propagation of the Arctic Oscillation from the stratosphere to the troposphere. *J. Geophys. Res. Atmos.* 104, 30937–30946. doi:10.1029/1999JD900445.

Banholzer, S., and Donner, S. The influence of different El Niño types on global average temperature. *Geophys. Res. Lett.* 41, 2093–2099. doi:10.1002/2014GL059520.

Barimalala, R., Bracco, A., and Kucharski, F. (2012). The representation of the South Tropical Atlantic teleconnection to the Indian Ocean in the AR4 coupled models. *Clim. Dyn.* 38, 1147–1166. doi:10.1007/s00382-011-1082-5.

Barimalala, R., Bracco, A., Kucharski, F., McCreary, J. P., and Crise, A. (2013). Arabian Sea ecosystem responses to the South Tropical Atlantic teleconnection. *J. Mar. Syst.* 117–118, 14–30. doi:10.1016/j.jmarsys.2013.03.002.

Barrier, N., Cassou, C., Deshayes, J., and Treguier, A.-M. (2014). Response of North Atlantic Ocean Circulation to Atmospheric Weather Regimes. *J. Phys. Oceanogr.* 44, 179–201. doi:10.1175/JPO-D-12-0217.1.

Barriopedro, D., Gallego, D., Alvarez-Castro, M. C., García-Herrera, R., Wheeler, D., Peña-Ortiz, C., et al. (2014). Witnessing North Atlantic westerlies variability from ships' logbooks (1685–2008). *Clim. Dyn.* 43, 939–955. doi:10.1007/s00382-013-1957-8.

Barrucand, M. G., Zitto, M. E., Piotrkowski, R., Canziani, P., and O'Neill, A. (2018). Historical SAM index time series: linear and nonlinear analysis. *Int. J. Climatol.* 38, e1091–e1106. doi:10.1002/joc.5435.

Behera, S. K., and Ratnam, J. V. (2018). Quasi-asymmetric response of the Indian summer monsoon rainfall to opposite phases of the IOD. *Sci. Rep.* 8, 123. doi:10.1038/s41598-017-18396-6.

ACCEPTED VERSION SUBJECT TO FINAL EDITING

Bellomo, K., Clement, A. C., Mauritsen, T., Rädel, G., and Stevens, B. (2015). The Influence of Cloud Feedbacks on Equatorial Atlantic Variability. *J. Clim.* 28, 2725–2744. doi:10.1175/JCLI-D-14-00495.1.

Benedict, J. J., and Randall, D. A. (2009). Structure of the Madden–Julian Oscillation in the Superparameterized CAM. *J. Atmos. Sci.* 66, 3277–3296. doi:10.1175/2009JAS3030.1.

Bernie, D. J., Guilyardi, E., Madec, G., Slingo, J. M., Woolnough, S. J., and Cole, J. (2008). Impact of resolving the diurnal cycle in an ocean–atmosphere GCM. Part 2: A diurnally coupled CGCM. *Clim. Dyn.* 31, 909–925. doi:10.1007/s00382-008-0429-z.

Biondi, F., Gershunov, A., and Cayan, D. R. (2001). North Pacific Decadal Climate Variability since 1661. *J. Clim.* 14, 5–10. doi:10.1175/1520-0442(2001)014<0005:NPDCVS>2.0.CO;2.

Blackport, R., and Screen, J. A. (2020). Weakened evidence for mid-latitude impacts of Arctic warming. *Nat. Clim. Chang.* 10, 1065–1066. doi:10.1038/s41558-020-00954-y.

Bladé, I., Liebmann, B., Fortuny, D., and van Oldenborgh, G. J. (2012). Observed and simulated impacts of the summer NAO in Europe: implications for projected drying in the Mediterranean region. *Clim. Dyn.* 39, 709–727. doi:10.1007/s00382-011-1195-x.

Boé, J., and Habets, F. (2014). Multi-decadal river flow variations in France. *Hydrol. Earth Syst. Sci.* 18, 691–708. doi:10.5194/hess-18-691-2014.

Boer, G. J., Smith, D. M., Cassou, C., Doblas-Reyes, F., Danabasoglu, G., Kirtman, B., et al. (2016). The Decadal Climate Prediction Project (DCPP) contribution to CMIP6. *Geosci. Model Dev.* 9, 3751–3777. doi:10.5194/gmd-9-3751-2016.

Bonnet, R., Boé, J., and Habets, F. (2020). Influence of multidecadal variability on high and low flows: the case of the Seine basin. *Hydrol. Earth Syst. Sci.* 24, 1611–1631. doi:10.5194/hess-24-1611-2020.

Brown, P. T., Li, W., and Xie, S.-P. (2015). Regions of significant influence on unforced global mean surface air temperature variability in climate models. *J. Geophys. Res. Atmos.* 120, 480–494. doi:10.1002/2014JD022576.

Buckley, B. M., Ummenhofer, C. C., D'Arrigo, R. D., Hansen, K. G., Truong, L. H., Le, C. L., et al. (2019). Interdecadal Pacific Oscillation reconstructed from trans-Pacific tree rings : 1350 – 2004 CE. *Clim. Dyn.* 53, 3181–3196. doi:10.1007/s00382-019-04694-4.

Burgman, R. J., and Jang, Y. (2015). Simulated U.S. drought response to interannual and decadal pacific SST variability. *J. Clim.* 28, 4688–4705. doi:10.1175/JCLI-D-14-00247.1.

Cabos, W., de la Vara, A., and Koseki, S. (2019). Tropical Atlantic Variability: Observations and Modeling. *Atmosphere (Basel).* 10, 502. doi:10.3390/atmos10090502.

Cai, W., Cowan, T., and Raupach, M. (2009). Positive Indian Ocean Dipole events precondition southeast Australia bushfires. *Geophys. Res. Lett.* 36, L19710. doi:10.1029/2009GL039902.

Cai, W., van Rensch, P., Cowan, T., and Sullivan, A. (2010). Asymmetry in ENSO Teleconnection with Regional Rainfall, Its Multidecadal Variability, and Impact. *J. Clim.* 23, 4944–4955. doi:10.1175/2010JCLI3501.1.

Cai, W., and Watterson, I. G. (2002). Modes of Interannual Variability of the Southern Hemisphere Circulation Simulated by the CSIRO Climate Model. *J. Clim.* 15, 1159–1174. doi:10.1175/1520-0442(2002)015<1159:MOIVOT>2.0.CO;2.

Cai, W., Wu, L., Lengaigne, M., Li, T., McGregor, S., Kug, J.-S., et al. (2019). Pantropical climate interactions. *Science (80-.).* 363, eaav4236. doi:10.1126/science.aav4236.

Capotondi, A., Wittenberg, A. T., Newman, M., Di Lorenzo, E., Yu, J.-Y., Braconnot, P., et al. (2015). Understanding ENSO Diversity. *Bull. Am. Meteorol. Soc.* 96, 921–938. doi:10.1175/BAMS-D-13-00117.1.

Cassou, C. (2008). Intraseasonal interaction between the Madden–Julian Oscillation and the North Atlantic Oscillation. *Nature* 455, 523–527. doi:10.1038/nature07286.

Cassou, C., Deser, C., and Alexander, M. A. (2007). Investigating the Impact of Reemerging Sea Surface Temperature Anomalies on the Winter Atmospheric Circulation over the North Atlantic. *J. Clim.* 20, 3510–3526. doi:10.1175/JCLI4202.1.

Cassou, C., Kushnir, Y., Hawkins, E., Pirani, A., Kucharski, F., Kang, I.-S., et al. (2018). Decadal Climate Variability and Predictability: Challenges and Opportunities. *Bull. Am. Meteorol. Soc.* 99, 479–490. doi:10.1175/BAMS-D-16-0286.1.

Cassou, C., Minvielle, M., Terray, L., and Périgaud, C. (2011). A statistical–dynamical scheme for reconstructing ocean forcing in the Atlantic. Part I: weather regimes as predictors for ocean surface variables. *Clim. Dyn.* 36, 19–39. doi:10.1007/s00382-010-0781-7.

Cassou, C., Terray, L., Hurrell, J. W., and Deser, C. (2004). North Atlantic Winter Climate Regimes: Spatial Asymmetry, Stationarity with Time, and Oceanic Forcing. *J. Clim.* 17, 1055–1068. doi:10.1175/1520-0442(2004)017<1055:NAWCRS>2.0.CO;2.

ACCEPTED VERSION SUBJECT TO FINAL EDITING

Cassou, C., Terray, L., and Phillips, A. S. (2005). Tropical Atlantic Influence on European Heat Waves. *J. Clim.* 18, 2805–2811. doi:10.1175/JCLI3506.1.

Castruccio, F. S., Ruprich-Robert, Y., Yeager, S. G., Danabasoglu, G., Msadek, R., and Delworth, T. L. (2018). Modulation of Arctic Sea Ice Loss by Atmospheric Teleconnections from Atlantic Multidecadal Variability. *J. Clim.* 32, 1419–1441. doi:10.1175/JCLI-D-18-0307.1.

Cattiaux, J., Vautard, R., Cassou, C., Yiou, P., Masson-Delmotte, V., and Codron, F. (2010). Winter 2010 in Europe: A cold extreme in a warming climate. *Geophys. Res. Lett.* 37, L20704. doi:10.1029/2010GL044613.

Cerrone, D., and Fusco, G. (2018). Low-frequency climate modes and Antarctic sea ice variations, 1982-2013. *J. Clim.* 31, 147–175. doi:10.1175/JCLI-D-17-0184.1.

Chang, P., Saravanan, R., Ji, L., and Hegerl, G. C. (2000). The Effect of Local Sea Surface Temperatures on Atmospheric Circulation over the Tropical Atlantic Sector. *J. Clim.* 13, 2195–2216. doi:10.1175/1520-0442(2000)013<2195:TEOLSS>2.0.CO;2.

Chen, X., and Wallace, J. M. (2015). ENSO-Like Variability: 1900–2013. *J. Clim.* 28, 9623–9641. doi:10.1175/JCLI-D-15-0322.1.

Chen, Y., and Zhai, P. (2017). Simultaneous modulations of precipitation and temperature extremes in Southern parts of China by the boreal summer intraseasonal oscillation. *Clim. Dyn.* 49, 3363–3381. doi:10.1007/s00382-016-3518-4.

Chiang, J. C. H., and Sobel, A. H. (2002). Tropical Tropospheric Temperature Variations Caused by ENSO and Their Influence on the Remote Tropical Climate. *J. Clim.* 15, 2616–2631. doi:10.1175/1520-0442(2002)015<2616:TTTVCB>2.0.CO;2.

Chiang, J. C. H., and Vimont, D. J. (2004). Analogous Pacific and Atlantic Meridional Modes of Tropical Atmosphere–Ocean Variability. *J. Clim.* 17, 4143–4158. doi:10.1175/JCLI4953.1.

Chisholm, R. A., Wijedasa, L. S., and Swinfield, T. (2016). The need for long-term remedies for Indonesia's forest fires. *Conserv. Biol.* 30, 5–6. doi:10.1111/cobi.12662.

Choi, K.-Y., Vecchi, G. A., and Wittenberg, A. T. (2015). Nonlinear Zonal Wind Response to ENSO in the CMIP5 Models: Roles of the Zonal and Meridional Shift of the ITCZ/SPCZ and the Simulated Climatological Precipitation. *J. Clim.* 28, 8556–8573. doi:10.1175/JCLI-D-15-0211.1.

Chowdary, J. S., Gnanaseelan, C., and Chakravorty, S. (2013). Impact of Northwest Pacific anticyclone on the Indian summer monsoon region. *Theor. Appl. Climatol.* 113, 329–336. doi:10.1007/s00704-012-0785-9.

Chowdary, J. S., Patekar, D., Srinivas, G., Gnanaseelan, C., and Parekh, A. (2019). Impact of the Indo-Western Pacific Ocean Capacitor mode on South Asian summer monsoon rainfall. *Clim. Dyn.* 53, 2327–2338. doi:10.1007/s00382-019-04850-w.

Chu, P. (2004). "ENSO and tropical cyclone activity," in *Hurricanes and typhoons: past, present and potential*, ed. K. B. Liu (New York, NY, USA: Columbia Press), 297–332.

Chylek, P., Dubey, M. K., Lesins, G., Li, J., and Hengartner, N. (2014). Imprint of the Atlantic multi-decadal oscillation and Pacific decadal oscillation on southwestern US climate: past, present, and future. *Clim. Dyn.* 43, 119–129. doi:10.1007/s00382-013-1933-3.

Chylek, P., Folland, C., Dijkstra, H., Lesins, G., and Dubey, M. (2011). Ice-core data evidence for a prominent near 20 year time-scale of the Atlantic Multidecadal Oscillation. *Geophys. Res. Lett.* 38, L13704. doi:10.1029/2011GL047501.

Ciasto, L. M., Simpkins, G. R., and England, M. H. (2015). Teleconnections between Tropical Pacific SST Anomalies and Extratropical Southern Hemisphere Climate. *J. Clim.* 28, 56–65. doi:10.1175/JCLI-D-14-00438.1.

Cid, A., Menéndez, M., Castanedo, S., Abascal, A. J., Méndez, F. J., and Medina, R. (2016). Long-term changes in the frequency, intensity and duration of extreme storm surge events in southern Europe. *Clim. Dyn.* 46, 1503–1516. doi:10.1007/s00382-015-2659-1.

Clem, K. R., Renwick, J. A., McGregor, J., and Fogt, R. L. (2016). The relative influence of ENSO and SAM on Antarctic Peninsula climate. *J. Geophys. Res. Atmos.* 121, 9324–9341. doi:10.1002/2016JD025305.Received.

Cohen, J., Screen, J. A., Furtado, J. C., Barlow, M., Whittleston, D., Coumou, D., et al. (2014). Recent Arctic amplification and extreme mid-latitude weather. *Nat. Geosci.* 7, 627–637. doi:10.1038/ngeo2234.

Cook, E. R., Kushnir, Y., Smerdon, J. E., Williams, A. P., Anchukaitis, K. J., and Wahl, E. R. (2019). A Euro-Mediterranean tree-ring reconstruction of the winter NAO index since 910 C.E. *Clim. Dyn.* 53, 1567–1580. doi:10.1007/s00382-019-04696-2.

Cornes, R. C., Jones, P. D., Briffa, K. R., and Osborn, T. J. (2013). Estimates of the North Atlantic Oscillation back to 1692 using a Paris-London westerly index. *Int. J. Climatol.* 33, 228–248. doi:10.1002/joc.3416.

Corti, S., Molteni, F., and Palmer, T. N. (1999). Signature of recent climate change in frequencies of natural atmospheric circulation regimes. *Nature* 398, 799–802. doi:10.1038/19745.

ACCEPTED VERSION SUBJECT TO FINAL EDITING

Crétat, J., Terray, P., Masson, S., Sooraj, K. P., and Roxy, M. K. (2017). Indian Ocean and Indian summer monsoon: relationships without ENSO in ocean–atmosphere coupled simulations. *Clim. Dyn.* 49, 1429–1448. doi:10.1007/s00382-016-3387-x.

Cropper, T., Hanna, E., Valente, M. A., and Jónsson, T. (2015). A daily Azores-Iceland North Atlantic Oscillation index back to 1850. *Geosci. Data J.* 2, 12–24. doi:10.1002/gdj3.23.

Crueger, T., Zinke, J., and Pfeiffer, M. (2009). Patterns of Pacific decadal variability recorded by Indian Ocean corals. *Int. J. Earth Sci.* 98, 41–52. doi:10.1007/s00531-008-0324-1.

D'Arrigo, R., and Ummenhofer, C. C. (2015). The climate of Myanmar: evidence for effects of the Pacific Decadal Oscillation. *Int. J. Climatol.* 35, 634–640. doi:10.1002/joc.3995.

D'Arrigo, R., Villalba, R., and Wiles, G. (2001). Tree-ring estimates of Pacific decadal climate variability. *Clim. Dyn.* 18, 219–224. doi:10.1007/s003820100177.

D'Arrigo, R., and Wilson, R. (2006). On the Asian expression of the PDO. *Int. J. Climatol.* 26, 1607–1617. doi:10.1002/joc.1326.

Dai, A. (2013). The influence of the inter-decadal Pacific oscillation on US precipitation during 1923–2010. *Clim. Dyn.* 41, 633–646. doi:10.1007/s00382-012-1446-5.

Dai, A., Fyfe, J. C., Xie, S. P., and Dai, X. (2015). Decadal modulation of global surface temperature by internal climate variability. *Nat. Clim. Chang.* 5, 555–559. doi:10.1038/nclimate2605.

Dätwyler, C., Neukom, R., Abram, N. J., Gallant, A. J. E., Grosjean, M., Jacques-Coper, M., et al. (2018). Teleconnection stationarity, variability and trends of the Southern Annular Mode (SAM) during the last millennium. *Clim. Dyn.* 51, 2321–2339. doi:10.1007/s00382-017-4015-0.

Davini, P., Cagnazzo, C., Neale, R., and Tribbia, J. (2012). Coupling between Greenland blocking and the North Atlantic Oscillation pattern. *Geophys. Res. Lett.* 39, L14701. doi:10.1029/2012GL052315.

Davini, P., Hardenberg, J. von, and Corti, S. (2015). Tropical origin for the impacts of the Atlantic Multidecadal Variability on the Euro-Atlantic climate. *Environ. Res. Lett.* 10, 094010. doi:10.1088/1748-9326/10/9/094010.

Day, J. J., Hargreaves, J. C., Annan, J. D., and Abe-Ouchi, A. (2012). Sources of multi-decadal variability in Arctic sea ice extent. *Environ. Res. Lett.* 7, 34011. doi:10.1088/1748-9326/7/3/034011.

Del Genio, A. D., Chen, Y., Kim, D., and Yao, M.-S. (2012). The MJO Transition from Shallow to Deep Convection in CloudSat /CALIPSO Data and GISS GCM Simulations. *J. Clim.* 25, 3755–3770. doi:10.1175/JCLI-D-11-00384.1.

Delaygue, G., Brönnimann, S., Jones, P. D., Blanchet, J., and Schwander, M. (2019). Reconstruction of Lamb weather type series back to the eighteenth century. *Clim. Dyn.* 52, 6131–6148. doi:10.1007/s00382-018-4506-7.

Delworth, T. L., and Zeng, F. (2016). The Impact of the North Atlantic Oscillation on Climate through Its Influence on the Atlantic Meridional Overturning Circulation. *J. Clim.* 29, 941–962. doi:10.1175/JCLI-D-15-0396.1.

DeMott, C. A., Klingaman, N. P., and Woolnough, S. J. (2015). Atmosphere-ocean coupled processes in the Madden-Julian oscillation. *Rev. Geophys.* 53, 1099–1154. doi:10.1002/2014RG000478.

Deng, K., Yang, S., Ting, M., Zhao, P., and Wang, Z. (2019). Dominant Modes of China Summer Heat Waves Driven by Global Sea Surface Temperature and Atmospheric Internal Variability. *J. Clim.* 32, 3761–3775. doi:10.1175/JCLI-D-18-0256.1.

Deppenmeier, A.-L., Haarsma, R. J., and Hazeleger, W. (2016). The Bjerknes feedback in the tropical Atlantic in CMIP5 models. *Clim. Dyn.* 47, 2691–2707. doi:10.1007/s00382-016-2992-z.

Deser, C. (2000). On the teleconnectivity of the "Arctic Oscillation." *Geophys. Res. Lett.* 27, 779–782. doi:10.1029/1999GL010945.

Deser, C., Alexander, M. A., Xie, S.-P., and Phillips, A. S. (2010). Sea Surface Temperature Variability: Patterns and Mechanisms. *Ann. Rev. Mar. Sci.* 2, 115–143. doi:10.1146/annurev-marine-120408-151453.

Deser, C., Simpson, I. R., McKinnon, K. A., and Phillips, A. S. (2017). The Northern Hemisphere Extratropical Atmospheric Circulation Response to ENSO: How Well Do We Know It and How Do We Evaluate Models Accordingly? *J. Clim.* 30, 5059–5082. doi:10.1175/JCLI-D-16-0844.1.

Deser, C., and Timlin, M. S. (1997). Atmosphere–Ocean Interaction on Weekly Timescales in the North Atlantic and Pacific. *J. Clim.* 10, 393–408. doi:10.1175/1520-0442(1997)010<0393:AOIOWT>2.0.CO;2.

Dezileau, L., Sabatier, P., Blanchemanche, P., Joly, B., Swingedouw, D., Cassou, C., et al. (2011). Intense storm activity during the Little Ice Age on the French Mediterranean coast. *Palaeogeogr. Palaeoclimatol. Palaeoecol.* 299, 289–297. doi:10.1016/j.palaeo.2010.11.009.

Di Lorenzo, E., Schneider, N., Cobb, K. M., Franks, P. J. S., Chhak, K., Miller, A. J., et al. (2008). North Pacific Gyre Oscillation links ocean climate and ecosystem change. *Geophys. Res. Lett.* 35, L08607. doi:10.1029/2007GL032838.

ACCEPTED VERSION SUBJECT TO FINAL EDITING

Diamond, H. J., and Renwick, J. A. (2015). The climatological relationship between tropical cyclones in the southwest pacific and the Madden-Julian Oscillation. *Int. J. Climatol.* 35, 676–686. doi:10.1002/joc.4012.

Diao, Y., Li, T., and Hsu, P. C. (2018). Influence of the Boreal Summer Intraseasonal Oscillation on Extreme Temperature Events in the Northern Hemisphere. *J. Meteorol. Res.* 32, 534–547. doi:10.1007/s13351-018-8031-8.

Ding, H., Keenlyside, N. S., and Latif, M. (2012). Impact of the Equatorial Atlantic on the El Niño Southern Oscillation. *Clim. Dyn.* 38, 1965–1972. doi:10.1007/s00382-011-1097-y.

Dippe, T., Greatbatch, R. J., and Ding, H. (2018). On the relationship between Atlantic Niño variability and ocean dynamics. *Clim. Dyn.* 51, 597–612. doi:10.1007/s00382-017-3943-z.

Domeisen, D. I. V. (2019). Estimating the Frequency of Sudden Stratospheric Warming Events From Surface Observations of the North Atlantic Oscillation. *J. Geophys. Res. Atmos.* 124, 3180–3194. doi:10.1029/2018JD030077.

Domeisen, D. I. V., Butler, A. H., Fröhlich, K., Bittner, M., Müller, W. A., and Baehr, J. (2015). Seasonal Predictability over Europe Arising from El Niño and Stratospheric Variability in the MPI-ESM Seasonal Prediction System. *J. Clim.* 28, 256–271. doi:10.1175/JCLI-D-14-00207.1.

Dong, B., Sutton, R. T., Woollings, T., and Hodges, K. (2013). Variability of the North Atlantic summer storm track: mechanisms and impacts on European climate. *Environ. Res. Lett.* 8, 034037. doi:10.1088/1748-9326/8/3/034037.

Dong, L., and McPhaden, M. J. (2017). Why has the relationship between Indian and Pacific Ocean decadal variability changed in recent decades? *J. Clim.* 30, 1971–1983. doi:10.1175/JCLI-D-16-0313.1.

Dong, L., and Zhou, T. (2014). The formation of the recent cooling in the eastern tropical Pacific Ocean and the associated climate impacts: A competition of global warming, IPO, and AMO. *J. Geophys. Res. Atmos.* 119, 11,272-11,287. doi:10.1002/2013JD021395.

Dong, L., Zhou, T., Dai, A., Song, F., Wu, B., and Chen, X. (2016). The Footprint of the Inter-decadal Pacific Oscillation in Indian Ocean Sea Surface Temperatures. *Sci. Rep.* 6, 21251. doi:10.1038/srep21251.

Douville, H., Peings, Y., and Saint-Martin, D. (2017). Snow-(N)AO relationship revisited over the whole twentieth century. *Geophys. Res. Lett.* 44, 569–577. doi:10.1002/2016GL071584.

Dréevillon, M., Cassou, C., and Terray, L. (2003). Model study of the North Atlantic region atmospheric response to autumn tropical Atlantic sea-surface-temperature anomalies. *Q. J. R. Meteorol. Soc.* 129, 2591–2611. doi:10.1256/qj.02.17.

Drouard, M., and Cassou, C. (2019). A Modeling- and Process-Oriented Study to Investigate the Projected Change of ENSO-Forced Wintertime Teleconnectivity in a Warmer World. *J. Clim.* 32, 8047–8068. doi:10.1175/JCLI-D-18-0803.1.

Drouard, M., Kornhuber, K., and Woollings, T. (2019). Disentangling Dynamic Contributions to Summer 2018 Anomalous Weather Over Europe. *Geophys. Res. Lett.* 46, 12537–12546. doi:10.1029/2019GL084601.

Drouard, M., Rivière, G., and Arbogast, P. (2015). The Link between the North Pacific Climate Variability and the North Atlantic Oscillation via Downstream Propagation of Synoptic Waves. *J. Clim.* 28, 3957–3976. doi:10.1175/JCLI-D-14-00552.1.

Du, Y., Xiao, J., and Yu, K. (2014). Tropical Indian Ocean Basin Mode recorded in coral oxygen isotope data from the Seychelles over the past 148 years. *Sci. China Earth Sci.* 57, 2597–2605. doi:10.1007/s11430-014-4956-7.

Du, Y., Yang, L., and Xie, S.-P. (2011). Tropical Indian Ocean Influence on Northwest Pacific Tropical Cyclones in Summer following Strong El Niño*. *J. Clim.* 24, 315–322. doi:10.1175/2010JCLI3890.1.

Dunstone, N. J., Smith, D. M., and Eade, R. (2011). Multi-year predictability of the tropical Atlantic atmosphere driven by the high latitude North Atlantic Ocean. *Geophys. Res. Lett.* 38, L14701. doi:10.1029/2011GL047949.

Durkee, J. D., Frye, J. D., Fuhrmann, C. M., Lacke, M. C., Jeong, H. G., and Mote, T. L. (2008). Effects of the North Atlantic Oscillation on precipitation-type frequency and distribution in the eastern United States. *Theor. Appl. Climatol.* 94, 51–65. doi:10.1007/s00704-007-0345-x.

Enfield, D. B., Mestas-Nuñez, A. M., and Trimble, P. J. (2001). The Atlantic Multidecadal Oscillation and its relation to rainfall and river flows in the continental U.S. *Geophys. Res. Lett.* 28, 2077–2080. doi:10.1029/2000GL012745.

Farneti, R., Molteni, F., and Kucharski, F. (2014). Pacific interdecadal variability driven by tropical–extratropical interactions. *Clim. Dyn.* 42, 3337–3355. doi:10.1007/s00382-013-1906-6.

Faust, J. C., Fabian, K., Milzer, G., Giraudeau, J., and Knies, J. (2016). Norwegian fjord sediments reveal NAO related winter temperature and precipitation changes of the past 2800 years. *Earth Planet. Sci. Lett.* 435, 84–93. doi:10.1016/j.epsl.2015.12.003.

Feldstein, S. B., and Franzke, C. (2006). Are the North Atlantic Oscillation and the Northern Annular Mode Distinguishable? *J. Atmos. Sci.* 63, 2915–2930. doi:10.1175/JAS3798.1.

ACCEPTED VERSION SUBJECT TO FINAL EDITING

Feldstein, S. B., and Franzke, C. L. E. (2017). "Atmospheric Teleconnection Patterns," in *Nonlinear and Stochastic Climate Dynamics*, eds. C. L. E. Franzke and T. J. OKane (Cambridge: Cambridge University Press), 54–104. doi:10.1017/9781316339251.004.

Ferranti, L., Palmer, T. N., Molteni, F., and Klinker, E. (1990). Tropical-Extratropical Interaction Associated with the 30–60 Day Oscillation and Its Impact on Medium and Extended Range Prediction. *J. Atmos. Sci.* 47, 2177–2199. doi:10.1175/1520-0469(1990)047<2177:TEIAWT>2.0.CO;2.

Ferreira, D., Marshall, J., Bitz, C. M., Solomon, S., and Plumb, A. (2015). Antarctic Ocean and Sea Ice Response to Ozone Depletion: A Two-Time-Scale Problem. *J. Clim.* 28, 1206–1226. doi:10.1175/JCLI-D-14-00313.1.

Fletcher, M.-S., Benson, A., Bowman, D. M. J. S., Gadd, P. S., Heijnis, H., Mariani, M., et al. (2018). Centennial-scale trends in the Southern Annular Mode revealed by hemisphere-wide fire and hydroclimatic trends over the past 2400 years. *Geology* 46, 363–366. doi:10.1130/G39661.1.

Fogt, R. L., Jones, J. M., and Renwick, J. (2012). Seasonal Zonal Asymmetries in the Southern Annular Mode and Their Impact on Regional Temperature Anomalies. *J. Clim.* 25, 6253–6270. doi:10.1175/JCLI-D-11-00474.1.

Folland, C. K., Knight, J., Linderholm, H. W., Fereday, D., Ineson, S., and Hurrell, J. W. (2009). The Summer North Atlantic Oscillation: Past, Present, and Future. *J. Clim.* 22, 1082–1103. doi:10.1175/2008JCLI2459.1.

Folland, C. K., Palmer, T. N., and Parker, D. E. (1986). Sahel rainfall and worldwide sea temperatures, 1901–85. *Nature* 320, 602–607. doi:10.1038/320602a0.

Folland, C. K., Renwick, J. A., Salinger, M. J., and Mullan, A. B. (2002). Relative influences of the Interdecadal Pacific Oscillation and ENSO on the South Pacific Convergence Zone. *Geophys. Res. Lett.* 29, 2–5. doi:10.1029/2001GL014201.

Foltz, G. R., Brandt, P., Richter, I., Rodríguez-Fonseca, B., Hernandez, F., Dengler, M., et al. (2019). The Tropical Atlantic Observing System. *Front. Mar. Sci.* 6, 206. doi:10.3389/fmars.2019.00206.

Foltz, G. R., and McPhaden, M. J. (2010). Interaction between the Atlantic meridional and Niño modes. *Geophys. Res. Lett.* 37, L18604. doi:https://doi.org/10.1029/2010GL044001.

Foltz, G. R., McPhaden, M. J., and Lumpkin, R. (2012). A Strong Atlantic Meridional Mode Event in 2009: The Role of Mixed Layer Dynamics*. *J. Clim.* 25, 363–380. doi:10.1175/JCLI-D-11-00150.1.

Frajka-Williams, E., Beaulieu, C., and Duchez, A. (2017). Emerging negative Atlantic Multidecadal Oscillation index in spite of warm subtropics. *Sci. Rep.* 7, 11224. doi:10.1038/s41598-017-11046-x.

Frank, W. M., and Roundy, P. E. (2006). The Role of Tropical Waves in Tropical Cyclogenesis. *Mon. Weather Rev.* 134, 2397–2417. doi:10.1175/MWR3204.1.

Frankignoul, C., Gastineau, G., and Kwon, Y.-O. (2017). Estimation of the SST Response to Anthropogenic and External Forcing and Its Impact on the Atlantic Multidecadal Oscillation and the Pacific Decadal Oscillation. *J. Clim.* 30, 9871–9895. doi:10.1175/JCLI-D-17-0009.1.

Franzke, C. L. E., Barbosa, S., Blender, R., Fredriksen, H., Laepple, T., Lambert, F., et al. (2020). The Structure of Climate Variability Across Scales. *Rev. Geophys.* 58, e2019RG000657. doi:10.1029/2019RG000657.

Friedman, A. R., Reverdin, G., Khodri, M., and Gastineau, G. (2017). A new record of Atlantic sea surface salinity from 1896 to 2013 reveals the signatures of climate variability and long-term trends. *Geophys. Res. Lett.* 44, 1866–1876. doi:10.1002/2017GL072582.

Fu, Z., Shi, L., Xie, F., and Piao, L. (2016). Nonlinear features of Northern Annular Mode variability. *Phys. A Stat. Mech. its Appl.* 449, 390–394. doi:10.1016/j.physa.2016.01.014.

Gadgil, S., Vinayachandran, P. N., Francis, P. A., and Gadgil, S. (2004). Extremes of the Indian summer monsoon rainfall, ENSO and equatorial Indian Ocean oscillation. *Geophys. Res. Lett.* 31, L12213. doi:10.1029/2004GL019733.

García-Serrano, J., and Haarsma, R. J. (2017). Non-annular, hemispheric signature of the winter North Atlantic Oscillation. *Clim. Dyn.* 48, 3659–3670. doi:10.1007/s00382-016-3292-3.

García-Serrano, J., Losada, T., and Rodríguez-Fonseca, B. (2011). Extratropical Atmospheric Response to the Atlantic Niño Decaying Phase. *J. Clim.* 24, 1613–1625. doi:10.1175/2010JCLI3640.1.

Garfinkel, C. I., and Schwartz, C. (2017). MJO-Related Tropical Convection Anomalies Lead to More Accurate Stratospheric Vortex Variability in Subseasonal Forecast Models. *Geophys. Res. Lett.* 44, 10054–10062. doi:10.1002/2017GL074470.

Gastineau, G., and Frankignoul, C. (2015). Influence of the North Atlantic SST Variability on the Atmospheric Circulation during the Twentieth Century. *J. Clim.* 28, 1396–1416. doi:10.1175/JCLI-D-14-00424.1.

Gedalof, Z., and Smith, D. J. (2001). Interdecadal climate variability and regime-scale shifts in Pacific North America. *Geophys. Res. Lett.* 28, 1515–1518. doi:10.1029/2000GL011779.

ACCEPTED VERSION SUBJECT TO FINAL EDITING

Gerber, E. P., Baldwin, M. P., Akiyoshi, H., Austin, J., Bekki, S., Braesicke, P., et al. (2010). Stratosphere-troposphere coupling and annular mode variability in chemistry-climate models. *J. Geophys. Res.* 115, D00M06. doi:10.1029/2009JD013770.

Gerber, E. P., and Martineau, P. (2018). Quantifying the variability of the annular modes: reanalysis uncertainty vs. sampling uncertainty. *Atmos. Chem. Phys.* 18, 17099–17117. doi:10.5194/acp-18-17099-2018.

Ghil, M., and Lucarini, V. (2020). The physics of climate variability and climate change. *Rev. Mod. Phys.* 92, 035002. doi:10.1103/RevModPhys.92.035002.

Giese, B. S., and Ray, S. (2011). El Niño variability in simple ocean data assimilation (SODA), 1871–2008. *J. Geophys. Res. Ocean.* 116, C02024. doi:10.1029/2010JC006695.

Gill, A. E. (1980). Some simple solutions for heat-induced tropical circulation. *Q. J. R. Meteorol. Soc.* 106, 447–462. doi:10.1002/qj.49710644905.

Gillett, N. P., Graf, H. F., and Osborn, T. J. (2003). "Climate change and the North Atlantic Oscillation," in *The North Atlantic Oscillation: Climatic Significance and Environmental Impact*, eds. J. W. Hurrell, Y. Kushnir, G. Ottersen, and M. Visbeck, 193–209. doi:10.1029/134GM09.

Gong, D., and Wang, S. (1999). Definition of Antarctic Oscillation index. *Geophys. Res. Lett.* 26, 459–462. doi:10.1029/1999GL900003.

Goodwin, I. D., and Harvey, N. (2008). Subtropical sea-level history from coral microatolls in the Southern Cook Islands, since 300 AD. *Mar. Geol.* 253, 14–25. doi:10.1016/j.margeo.2008.04.012.

Goodwin, I. D., van Ommen, T. D., Curran, M. A. J., and Mayewski, P. A. (2004). Mid latitude winter climate variability in the South Indian and southwest Pacific regions since 1300 AD. *Clim. Dyn.* 22, 783–794. doi:10.1007/s00382-004-0403-3.

Grant, A., and Walsh, K. J. E. (2001). Interdecadal variability in north-east Australian tropical cyclone formation. *Atmos. Sci. Lett.* 2, 9–17. doi:10.1006/asle.2001.0029.

Gray, L. J., Woollings, T. J., Andrews, M., and Knight, J. (2016). Eleven-year solar cycle signal in the NAO and Atlantic/European blocking. *Q. J. R. Meteorol. Soc.* 142, 1890–1903. doi:10.1002/qj.2782.

Gray, S. T., Graumlich, L. J., Betancourt, J. L., and Pederson, G. T. (2004). A tree-ring based reconstruction of the Atlantic Multidecadal Oscillation since 1567 A.D. *Geophys. Res. Lett.* 31, L12205. doi:10.1029/2004GL019932.

Green, B., Marshall, J., and Donohoe, A. (2017). Twentieth century correlations between extratropical SST variability and ITCZ shifts. *Geophys. Res. Lett.* 44, 9039–9047. doi:10.1002/2017GL075044.

Grimm, A. M. (2019). Madden–Julian Oscillation impacts on South American summer monsoon season: precipitation anomalies, extreme events, teleconnections, and role in the MJO cycle. *Clim. Dyn.* 53, 907–932. doi:10.1007/s00382-019-04622-6.

Haarsma, R. J., and Hazeleger, W. (2007). Extratropical Atmospheric Response to Equatorial Atlantic Cold Tongue Anomalies. *J. Clim.* 20, 2076–2091. doi:10.1175/JCLI4130.1.

Ham, Y.-G., Kug, J.-S., and Park, J.-Y. (2013a). Two distinct roles of Atlantic SSTs in ENSO variability: North Tropical Atlantic SST and Atlantic Niño. *Geophys. Res. Lett.* 40, 4012–4017. doi:10.1002/grl.50729.

Ham, Y.-G., Kug, J.-S., Park, J.-Y., and Jin, F.-F. (2013b). Sea surface temperature in the north tropical Atlantic as a trigger for El Niño/Southern Oscillation events. *Nat. Geosci.* 6, 112–116. doi:10.1038/ngeo1686.

Han, W., Meehl, G. A., Hu, A., Alexander, M. A., Yamagata, T., Yuan, D., et al. (2014). Intensification of decadal and multi-decadal sea level variability in the western tropical Pacific during recent decades. *Clim. Dyn.* 43, 1357–1379. doi:10.1007/s00382-013-1951-1.

Han, W., Meehl, G. A., Stammer, D., Hu, A., Hamlington, B., Kenigson, J., et al. (2017). Spatial Patterns of Sea Level Variability Associated with Natural Internal Climate Modes. *Surv. Geophys.* 38, 217–250. doi:10.1007/s10712-016-9386-y.

Hannachi, A., Straus, D. M., Franzke, C. L. E., Corti, S., and Woollings, T. (2017). Low-frequency nonlinearity and regime behavior in the Northern Hemisphere extratropical atmosphere. *Rev. Geophys.* 55, 199–234. doi:10.1002/2015RG000509.

Hannah, W. M., Maloney, E. D., and Pritchard, M. S. (2015). Consequences of systematic model drift in DYNAMO MJO hindcasts with SP-CAM and CAM5. *J. Adv. Model. Earth Syst.* 7, 1051–1074. doi:10.1002/2014MS000423.

Hastenrath, S., and Heller, L. (1977). Dynamics of climatic hazards in northeast Brazil. *Q. J. R. Meteorol. Soc.* 103, 77–92. doi:10.1002/qj.49710343505.

Henley, B. J. (2017). Pacific decadal climate variability: Indices, patterns and tropical-extratropical interactions. *Glob. Planet. Change* 155, 42–55. doi:10.1016/j.gloplacha.2017.06.004.

Henley, B. J., Gergis, J., Karoly, D. J., Power, S., Kennedy, J., and Folland, C. K. (2015). A Tripole Index for the Interdecadal Pacific Oscillation. *Clim. Dyn.* 45, 3077–3090. doi:10.1007/s00382-015-2525-1.

ACCEPTED VERSION SUBJECT TO FINAL EDITING

Henley, B. J., Meehl, G., Power, S. B., Folland, C. K., King, A. D., Brown, J. N., et al. (2017). Spatial and temporal agreement in climate model simulations of the Interdecadal Pacific Oscillation. *Environ. Res. Lett.* 12, 044011. doi:10.1088/1748-9326/aa5cc8.

Hermanson, L., Eade, R., Robinson, N. H., Dunstone, N. J., Andrews, M. B., Knight, J. R., et al. (2014). Forecast cooling of the Atlantic subpolar gyre and associated impacts. *Geophys. Res. Lett.* 41, 5167–5174. doi:10.1002/2014GL060420.

Hernández, A., Martin-Puertas, C., Moffa-Sánchez, P., Moreno-Chamarro, E., Ortega, P., Blockley, S., et al. (2020). Modes of climate variability: Synthesis and review of proxy-based reconstructions through the Holocene. *Earth-Science Rev.* 209, 103286. doi:10.1016/j.earscirev.2020.103286.

Hessl, A., Allen, K. J., Vance, T., Abram, N. J., and Saunders, K. M. (2017). Reconstructions of the southern annular mode (SAM) during the last millennium. *Prog. Phys. Geogr. Earth Environ.* 41, 834–849. doi:10.1177/0309133317743165.

Higgins, R. W., and Mo, K. C. (1997). Persistent North Pacific Circulation Anomalies and the Tropical Intraseasonal Oscillation. *J. Clim.* 10, 223–244. doi:10.1175/1520-0442(1997)010<0223:PNPCAA>2.0.CO;2.

Ho, M., Kiem, A. S., and Verdon-Kidd, D. C. (2012). The Southern Annular Mode: a comparison of indices. *Hydrol. Earth Syst. Sci.* 16, 967–982. doi:10.5194/hess-16-967-2012.

Hodgkins, G. A., Whitfield, P. H., Burn, D. H., Hannaford, J., Renard, B., Stahl, K., et al. (2017). Climate-driven variability in the occurrence of major floods across North America and Europe. *J. Hydrol.* 552, 704–717. doi:10.1016/j.jhydrol.2017.07.027.

Hohenegger, C., and Bretherton, C. S. (2011). Simulating deep convection with a shallow convection scheme. *Atmos. Chem. Phys.* 11, 10389–10406. doi:10.5194/acp-11-10389-2011.

Holbrook, N. J., Scannell, H. A., Sen Gupta, A., Benthuysen, J. A., Feng, M., Oliver, E. C. J., et al. (2019). A global assessment of marine heatwaves and their drivers. *Nat. Commun.* 10, 2624. doi:10.1038/s41467-019-10206-z.

Holz, A., Paritsis, J., Mundo, I. A., Veblen, T. T., Kitzberger, T., Williamson, G. J., et al. (2017). Southern Annular Mode drives multicentury wildfire activity in southern South America. *Proc. Natl. Acad. Sci.* 114, 9552–9557. doi:10.1073/pnas.1705168114.

Honda, M., and Nakamura, H. (2001). Interannual Seesaw between the Aleutian and Icelandic Lows. Part II: Its Significance in the Interannual Variability over the Wintertime Northern Hemisphere. *J. Clim.* 14, 4512–4529. doi:10.1175/1520-0442(2001)014<4512:ISBTAA>2.0.CO;2.

Horel, J. D., and Wallace, J. M. (1981). Planetary-Scale Atmospheric Phenomena Associated with the Southern Oscillation. *Mon. Weather Rev.* 109, 813–829. doi:10.1175/1520-0493(1981)109<0813:PSAPAW>2.0.CO;2.

Hoskins, B. J., and Karoly, D. J. (1981). The Steady Linear Response of a Spherical Atmosphere to Thermal and Orographic Forcing. *J. Atmos. Sci.* 38, 1179–1196. doi:10.1175/1520-0469(1981)038<1179:TSLROA>2.0.CO;2.

Hourdin, F., Grandpeix, J.-Y., Rio, C., Bony, S., Jam, A., Cheruy, F., et al. (2013). LMDZ5B: the atmospheric component of the IPSL climate model with revisited parameterizations for clouds and convection. *Clim. Dyn.* 40, 2193–2222. doi:10.1007/s00382-012-1343-y.

Hsu, P.-C., Lee, J.-Y., and Ha, K.-J. (2016). Influence of boreal summer intraseasonal oscillation on rainfall extremes in southern China. *Int. J. Climatol.* 36, 1403–1412. doi:10.1002/joc.4433.

Hsu, P.-C., Lee, J.-Y., Ha, K.-J., and Tsou, C.-H. (2017). Influences of boreal summer intraseasonal oscillation on heat waves in monsoon asia. *J. Clim.* 30, 7191–7211. doi:10.1175/JCLI-D-16-0505.1.

Hu, K., Huang, G., Qu, X., and Huang, R. (2012). The impact of Indian Ocean variability on high temperature extremes across the southern Yangtze River valley in late summer. *Adv. Atmos. Sci.* 29, 91–100. doi:10.1007/s00376-011-0209-2.

Huang, Y., Wu, B., Li, T., Zhou, T., and Liu, B. (2019). Interdecadal Indian Ocean Basin Mode Driven by Interdecadal Pacific Oscillation: A Season-Dependent Growth Mechanism. *J. Clim.* 32, 2057–2073. doi:10.1175/JCLI-D-18-0452.1.

Hung, M.-P., Lin, J.-L., Wang, W., Kim, D., Shinoda, T., and Weaver, S. J. (2013). MJO and Convectively Coupled Equatorial Waves Simulated by CMIP5 Climate Models. *J. Clim.* 26, 6185–6214. doi:10.1175/JCLI-D-12-00541.1.

Hurrell, J. W. (1995). Decadal Trends in the North Atlantic Oscillation: Regional Temperatures and Precipitation. *Science (80-.).* 269, 676–679. doi:10.1126/science.269.5224.676.

Hurrell, J. W., and Deser, C. (2009). North Atlantic climate variability: The role of the North Atlantic Oscillation. *J. Mar. Syst.* 78, 28–41. doi:10.1016/j.jmarsys.2008.11.026.

Hurrell, J. W., Kushnir, Y., Ottersen, G., and Visbeck, M. (2003). "An overview of the North Atlantic Oscillation," in *The North Atlantic Oscillation: Climatic Significance and Environmental Impact*, eds. J. W. Hurrell, Y. Kushnir, G. Ottersen, and M. Visbeck, 1–35. doi:10.1029/134GM01.

ACCEPTED VERSION SUBJECT TO FINAL EDITING

Ineson, S., Scaife, A. A., Knight, J. R., Manners, J. C., Dunstone, N. J., Gray, L. J., et al. (2011). Solar forcing of winter climate variability in the Northern Hemisphere. *Nat. Geosci.* 4, 753–757. doi:10.1038/ngeo1282.

Inness, P. M., Slingo, J. M., Guilyardi, E., and Cole, J. (2003). Simulation of the Madden–Julian Oscillation in a Coupled General Circulation Model. Part II: The Role of the Basic State. *J. Clim.* 16, 365–382. doi:10.1175/1520-0442(2003)016<0365:SOTMJO>2.0.CO;2.

Itoh, H. (2008). Reconsideration of the True versus Apparent Arctic Oscillation. *J. Clim.* 21, 2047–2062. doi:10.1175/2007JCLI2167.1.

Jerez, S., Trigo, R. M., Vicente-Serrano, S. M., Pozo-Vázquez, D., Lorente-Plazas, R., Lorenzo-Lacruz, J., et al. (2013). The Impact of the North Atlantic Oscillation on Renewable Energy Resources in Southwestern Europe. *J. Appl. Meteorol. Climatol.* 52, 2204–2225. doi:10.1175/JAMC-D-12-0257.1.

Jiang, X., Zhao, M., Maloney, E. D., and Waliser, D. E. (2016). Convective moisture adjustment time scale as a key factor in regulating model amplitude of the Madden-Julian Oscillation. *Geophys. Res. Lett.* 43, 10,412-10,419. doi:10.1002/2016GL070898.

Joly, M., and Voldoire, A. (2010). Role of the Gulf of Guinea in the inter-annual variability of the West African monsoon: what do we learn from CMIP3 coupled simulations? *Int. J. Climatol.* 30, 1843–1856. doi:10.1002/joc.2026.

Jones, J. M., Gille, S. T., Goosse, H., Abram, N. J., Canziani, P. O., Charman, D. J., et al. (2016). Assessing recent trends in high-latitude Southern Hemisphere surface climate. *Nat. Clim. Chang.* 6, 917–926. doi:10.1038/nclimate3103.

Jones, P. D., Jonsson, T., and Wheeler, D. (1997). Extension to the North Atlantic oscillation using early instrumental pressure observations from Gibraltar and south-west Iceland. *Int. J. Climatol.* 17, 1433–1450. doi:10.1002/(SICI)1097-0088(19971115)17:13<1433::AID-JOC203>3.0.CO;2-P.

Joseph, S., Sahai, A. K., and Goswami, B. N. (2009). Eastward propagating MJO during boreal summer and Indian monsoon droughts. *Clim. Dyn.* 32, 1139–1153. doi:10.1007/s00382-008-0412-8.

Jouanno, J., Hernandez, O., and Sanchez-Gomez, E. (2017). Equatorial Atlantic interannual variability and its relation to dynamic and thermodynamic processes. *Earth Syst. Dyn.* 8, 1061–1069. doi:10.5194/esd-8-1061-2017.

Kajtar, J. B., Santoso, A., England, M. H., and Cai, W. (2017). Tropical climate variability: interactions across the Pacific, Indian, and Atlantic Oceans. *Clim. Dyn.* 48, 2173–2190. doi:10.1007/s00382-016-3199-z.

Kamae, Y., Mei, W., Xie, S.-P., Naoi, M., and Ueda, H. (2017). Atmospheric Rivers over the Northwestern Pacific: Climatology and Interannual Variability. *J. Clim.* 30, 5605–5619. doi:10.1175/JCLI-D-16-0875.1.

Kang, S. M., Polvani, L. M., Fyfe, J. C., and Sigmond, M. (2011). Impact of Polar Ozone Depletion on Subtropical Precipitation. *Science (80-.).* 332, 951–954. doi:10.1126/science.1202131.

Karoly, D. J. (1989). Southern Hemisphere Circulation Features Associated with El Niño–Southern Oscillation Events. *J. Clim.* 2, 1239–1252. Available at: http://www.jstor.org/stable/26196374.

Karpechko, A. Y., Hitchcock, P., Peters, D. H. W., and Schneidereit, A. (2017). Predictability of downward propagation of major sudden stratospheric warmings. *Q. J. R. Meteorol. Soc.* 143, 1459–1470. doi:10.1002/qj.3017.

Kayanne, H., Iijima, H., Nakamura, N., McClanahan, T. R., Behera, S., and Yamagata, T. (2006). Indian Ocean Dipole index recorded in Kenyan coral annual density bands. *Geophys. Res. Lett.* 33, L19709. doi:10.1029/2006GL027168.

Keenlyside, N. S., Ding, H., and Latif, M. (2013). Potential of equatorial Atlantic variability to enhance El Niño prediction. *Geophys. Res. Lett.* 40, 2278–2283. doi:10.1002/grl.50362.

Keenlyside, N. S., and Latif, M. (2007). Understanding Equatorial Atlantic Interannual Variability. *J. Clim.* 20, 131–142. doi:10.1175/JCLI3992.1.

Kemball-Cook, S., and Wang, B. (2001). Equatorial Waves and Air–Sea Interaction in the Boreal Summer Intraseasonal Oscillation. *J. Clim.* 14, 2923–2942. doi:10.1175/1520-0442(2001)014<2923:EWAASI>2.0.CO;2.

Kennedy, J. J., Rayner, N. A., Atkinson, C. P., and Killick, R. E. (2019). An Ensemble Data Set of Sea Surface Temperature Change From 1850: The Met Office Hadley Centre HadSST.4.0.0.0 Data Set. *J. Geophys. Res. Atmos.* 124, 7719–7763. doi:10.1029/2018JD029867.

Kerr, R. A. (2000). A North Atlantic Climate Pacemaker for the Centuries. *Science (80-.).* 288, 1984–1985. doi:10.1126/science.288.5473.1984.

Kikuchi, K., Wang, B., and Kajikawa, Y. (2012). Bimodal representation of the tropical intraseasonal oscillation. *Clim. Dyn.* 38, 1989–2000. doi:10.1007/s00382-011-1159-1.

Kilbourne, K. H., Alexander, M. A., and Nye, J. A. (2014). A low latitude paleoclimate perspective on Atlantic multidecadal variability. *J. Mar. Syst.* 133, 4–13. doi:https://doi.org/10.1016/j.jmarsys.2013.09.004.

ACCEPTED VERSION SUBJECT TO FINAL EDITING

Kim, D., Sobel, A. H., Del Genio, A. D., Chen, Y., Camargo, S. J., Yao, M.-S., et al. (2012). The Tropical Subseasonal Variability Simulated in the NASA GISS General Circulation Model. *J. Clim.* 25, 4641–4659. doi:10.1175/JCLI-D-11-00447.1.

Kim, D., Sperber, K., Stern, W., Waliser, D., Kang, I.-S., Maloney, E., et al. (2009). Application of MJO Simulation Diagnostics to Climate Models. *J. Clim.* 22, 6413–6436. doi:10.1175/2009JCLI3063.1.

Kim, H.-M. (2017). The impact of the mean moisture bias on the key physics of MJO propagation in the ECMWF reforecast. *J. Geophys. Res. Atmos.* 122, 7772–7784. doi:10.1002/2017JD027005.

Kim, H., Vitart, F., and Waliser, D. E. (2018). Prediction of the Madden–Julian Oscillation: A Review. *J. Clim.* 31, 9425–9443. doi:10.1175/JCLI-D-18-0210.1.

King, A. D., Klingaman, N. P., Alexander, L. V, Donat, M. G., Jourdain, N. C., and Maher, P. (2014). Extreme Rainfall Variability in Australia: Patterns, Drivers, and Predictability. *J. Clim.* 27, 6035–6050. doi:10.1175/JCLI-D-13-00715.1.

Kitzberger, T., Brown, P. M., Heyerdahl, E. K., Swetnam, T. W., and Veblen, T. T. (2007). Contingent Pacific-Atlantic Ocean influence on multicentury wildfire synchrony over western North America. *Proc. Natl. Acad. Sci.* 104, 543–548. doi:10.1073/pnas.0606078104.

Klein, S. A., Soden, B. J., and Lau, N.-C. (1999). Remote Sea Surface Temperature Variations during ENSO: Evidence for a Tropical Atmospheric Bridge. *J. Clim.* 12, 917–932. doi:10.1175/1520-0442(1999)012<0917:RSSTVD>2.0.CO;2.

Klotzbach, P. J., and Oliver, E. C. J. (2015). Modulation of Atlantic Basin Tropical Cyclone Activity by the Madden–Julian Oscillation (MJO) from 1905 to 2011. *J. Clim.* 28, 204–217. doi:10.1175/JCLI-D-14-00509.1.

Knudsen, M. F., Seidenkrantz, M.-S., Jacobsen, B. H., and Kuijpers, A. (2011). Tracking the Atlantic Multidecadal Oscillation through the last 8,000 years. *Nat. Commun.* 2, 178. doi:10.1038/ncomms1186.

Kosaka, Y., Xie, S.-P., Lau, N.-C., and Vecchi, G. A. (2013). Origin of seasonal predictability for summer climate over the Northwestern Pacific. *Proc. Natl. Acad. Sci. U. S. A.* 110, 7574–7579. doi:10.1073/pnas.1215582110.

Kostov, Y., Marshall, J., Hausmann, U., Armour, K. C., Ferreira, D., and Holland, M. M. (2017). Fast and slow responses of Southern Ocean sea surface temperature to SAM in coupled climate models. *Clim. Dyn.* 48, 1595–1609. doi:10.1007/s00382-016-3162-z.

Kucharski, F., Bracco, A., Yoo, J. H., and Molteni, F. (2007). Low-Frequency Variability of the Indian Monsoon–ENSO Relationship and the Tropical Atlantic: The "Weakening" of the 1980s and 1990s. *J. Clim.* 20, 4255–4266. doi:10.1175/JCLI4254.1.

Kucharski, F., Bracco, A., Yoo, J. H., and Molteni, F. (2008). Atlantic forced component of the Indian monsoon interannual variability. *Geophys. Res. Lett.* 35, L04706. doi:10.1029/2007GL033037.

Kucharski, F., Ikram, F., Molteni, F., Farneti, R., Kang, I.-S., No, H.-H., et al. (2016). Atlantic forcing of Pacific decadal variability. *Clim. Dyn.* 46, 2337–2351. doi:10.1007/s00382-015-2705-z.

Kucharski, F., and Joshi, M. K. (2017). Influence of tropical South Atlantic sea-surface temperatures on the Indian summer monsoon in CMIP5 models. *Q. J. R. Meteorol. Soc.* 143, 1351–1363. doi:10.1002/qj.3009.

Kug, J.-S., and Ham, Y.-G. (2011). Are there two types of La Nina? *Geophys. Res. Lett.* 38, L16704. doi:10.1029/2011GL048237.

Kuleshov, Y., Qi, L., Fawcett, R., and Jones, D. (2008). On tropical cyclone activity in the Southern Hemisphere: Trends and the ENSO connection. *Geophys. Res. Lett.* 35. doi:10.1029/2007GL032983.

L'Heureux, M. L., and Higgins, R. W. (2008). Boreal Winter Links between the Madden–Julian Oscillation and the Arctic Oscillation. *J. Clim.* 21, 3040–3050. doi:10.1175/2007JCLI1955.1.

L'Heureux, M. L., Lee, S., and Lyon, B. (2013). Recent multidecadal strengthening of the Walker circulation across the tropical Pacific. *Nat. Clim. Chang.* 3, 571–576. doi:10.1038/nclimate1840.

L'Heureux, M. L., Takahashi, K., Watkins, A. B., Barnston, A. G., Becker, E. J., Di Liberto, T. E., et al. (2017). Observing and Predicting the 2015/16 El Niño. *Bull. Am. Meteorol. Soc.* 98, 1363–1382. doi:10.1175/BAMS-D-16-0009.1.

Lapointe, F., Bradley, R. S., Francus, P., Balascio, N. L., Abbott, M. B., Stoner, J. S., et al. (2020). Annually resolved Atlantic sea surface temperature variability over the past 2,900 y. *Proc. Natl. Acad. Sci.*, 202014166. doi:10.1073/pnas.2014166117.

Latif, M., and Grötzner, A. (2000). The equatorial Atlantic oscillation and its response to ENSO. *Clim. Dyn.* 16, 213–218. doi:10.1007/s003820050014.

Lau, N.-C., and Nath, M. J. (2000). Impact of ENSO on the Variability of the Asian–Australian Monsoons as Simulated in GCM Experiments. *J. Clim.* 13, 4287–4309. doi:10.1175/1520-0442(2000)013<4287:IOEOTV>2.0.CO;2.

Lau, N.-C., and Nath, M. J. (2003). Atmosphere–Ocean Variations in the Indo-Pacific Sector during ENSO Episodes. *J. Clim.* 16, 3–20. doi:10.1175/1520-0442(2003)016<0003:AOVITI>2.0.CO;2.

ACCEPTED VERSION SUBJECT TO FINAL EDITING

Lau, W. K. M., Waliser, D. E., and Tian, B. (2012). "Chemical and biological impacts," in *Intraseasonal Variability in the Atmosphere-Ocean Climate System* (Berlin, Heidelberg: Springer Berlin Heidelberg), 569–585. doi:10.1007/978-3-642-13914-7_18.

Le Mouël, J., Lopes, F., and Courtillot, V. (2019). A Solar Signature in Many Climate Indices. *J. Geophys. Res. Atmos.* 124, 2600–2619. doi:10.1029/2018JD028939.

Lee, J.-Y., Kwon, M. H., Yun, K.-S., Min, S.-K., Park, I.-H., Ham, Y.-G., et al. (2017). The long-term variability of Changma in the East Asian summer monsoon system: A review and revisit. *Asia-Pacific J. Atmos. Sci.* 53, 257–272. doi:10.1007/s13143-017-0032-5.

Lee, J.-Y., Wang, B., Wheeler, M. C., Fu, X., Waliser, D. E., and Kang, I.-S. (2013). Real-time multivariate indices for the boreal summer intraseasonal oscillation over the Asian summer monsoon region. *Clim. Dyn.* 40, 493–509. doi:10.1007/s00382-012-1544-4.

Lee, Y.-Y., and Grotjahn, R. (2019). Evidence of Specific MJO Phase Occurrence with Summertime California Central Valley Extreme Hot Weather. *Adv. Atmos. Sci.* 36, 589–602. doi:10.1007/s00376-019-8167-1.

Lewis, S. C., and LeGrande, A. N. (2015). Stability of ENSO and its tropical Pacific teleconnections over the Last Millennium. *Clim. Past* 11, 1347–1360. doi:10.5194/cp-11-1347-2015.

Li, G., Ren, B., Yang, C., and Zheng, J. (2010a). Indices of El Niño and El Niño Modoki: An improved El Niño Modoki index. *Adv. Atmos. Sci.* 27, 1210–1220. doi:10.1007/s00376-010-9173-5.

Li, J., and Wang, J. X. L. (2003). A new North Atlantic Oscillation index and its variability. *Adv. Atmos. Sci.* 20, 661–676. doi:10.1007/BF02915394.

Li, K.-F., Tian, B., Waliser, D. E., and Yung, Y. L. (2010b). Tropical mid-tropospheric CO2 variability driven by the Madden-Julian oscillation. *Proc. Natl. Acad. Sci.* 107, 19171–19175. doi:10.1073/pnas.1008222107.

Li, T., Liu, P., Fu, X., Wang, B., and Meehl, G. A. (2006). Spatiotemporal Structures and Mechanisms of the Tropospheric Biennial Oscillation in the Indo-Pacific Warm Ocean Regions*. *J. Clim.* 19, 3070–3087. doi:10.1175/JCLI3736.1.

Li, W., Li, L., and Deng, Y. (2015). Impact of the Interdecadal Pacific Oscillation on Tropical Cyclone Activity in the North Atlantic and Eastern North Pacific. *Sci. Rep.* 5, 12358. doi:10.1038/srep12358.

Li, Z., Zhang, W., Jin, F.-F., Stuecker, M. F., Sun, C., Levine, A. F. Z., et al. (2020). A robust relationship between multidecadal global warming rate variations and the Atlantic Multidecadal Variability. *Clim. Dyn.* 55, 1945–1959. doi:10.1007/s00382-020-05362-8.

Lim, E.-P., Hendon, H. H., Boschat, G., Hudson, D., Thompson, D. W. J., Dowdy, A. J., et al. (2019). Australian hot and dry extremes induced by weakenings of the stratospheric polar vortex. *Nat. Geosci.* 12, 896–901. doi:10.1038/s41561-019-0456-x.

Lin, H., Brunet, G., and Derome, J. (2009). An Observed Connection between the North Atlantic Oscillation and the Madden–Julian Oscillation. *J. Clim.* 22, 364–380. doi:10.1175/2008JCLI2515.1.

Lin, J.-L., Kiladis, G. N., Mapes, B. E., Weickmann, K. M., Sperber, K. R., Lin, W., et al. (2006). Tropical Intraseasonal Variability in 14 IPCC AR4 Climate Models. Part I: Convective Signals. *J. Clim.* 19, 2665–2690. doi:10.1175/JCLI3735.1.

Linderholm, H. W., Folland, C. K., and Walther, A. (2009). A multicentury perspective on the summer North Atlantic Oscillation (SNAO) and drought in the eastern Atlantic Region. *J. Quat. Sci.* 24, 415–425. doi:10.1002/jqs.1261.

Linderholm, H. W., Ou, T., Jeong, J.-H., Folland, C. K., Gong, D., Liu, H., et al. (2011). Interannual teleconnections between the summer North Atlantic Oscillation and the East Asian summer monsoon. *J. Geophys. Res.* 116, D13107. doi:10.1029/2010JD015235.

Linsley, B. K., Wu, H. C., Dassié, E. P., and Schrag, D. P. (2015). Decadal changes in South Pacific sea surface temperatures and the relationship to the Pacific decadal oscillation and upper ocean heat content. *Geophys. Res. Lett.* 42, 2358–2366. doi:10.1002/2015GL063045.

Liu, C., Tian, B., Li, K.-F., Manney, G. L., Livesey, N. J., Yung, Y. L., et al. (2014). Northern Hemisphere mid-winter vortex-displacement and vortex-split stratospheric sudden warmings: Influence of the Madden-Julian Oscillation and Quasi-Biennial Oscillation. *J. Geophys. Res. Atmos.* 119, 12,599-12,620. doi:10.1002/2014JD021876.

Liu, K. S., and Chan, J. C. L. (2008). Interdecadal Variability of Western North Pacific Tropical Cyclone Tracks. *J. Clim.* 21, 4464–4476. doi:10.1175/2008JCLI2207.1.

Liu, T., Li, J., Li, Y., Zhao, S., Zheng, F., Zheng, J., et al. (2018). Influence of the May Southern annular mode on the South China Sea summer monsoon. *Clim. Dyn.* 51, 4095–4107. doi:10.1007/s00382-017-3753-3.

Liu, Z., and Di Lorenzo, E. (2018). Mechanisms and Predictability of Pacific Decadal Variability. *Curr. Clim. Chang. Reports* 4, 128–144. doi:10.1007/s40641-018-0090-5.

Lorenz, D. J., and Hartmann, D. L. (2003). Eddy–Zonal Flow Feedback in the Northern Hemisphere Winter. *J. Clim.* 16, 1212–1227. doi:10.1175/1520-0442(2003)16<1212:EFFITN>2.0.CO;2.

ACCEPTED VERSION SUBJECT TO FINAL EDITING

Losada, T., Rodríguez-Fonseca, B., Janicot, S., Gervois, S., Chauvin, F., and Ruti, P. (2010). A multi-model approach to the Atlantic Equatorial mode: impact on the West African monsoon. *Clim. Dyn.* 35, 29–43. doi:10.1007/s00382-009-0625-5.

Losada, T., Rodríguez-Fonseca, B., and Kucharski, F. (2012). Tropical influence on the summer Mediterranean climate. *Atmos. Sci. Lett.* 13, 36–42. doi:10.1002/asl.359.

Lu, Z., Liu, Z., Zhu, J., and Cobb, K. M. (2018). A Review of Paleo El Niño-Southern Oscillation. *Atmosphere (Basel).* 9, 130. doi:10.3390/atmos9040130.

Lübbecke, J. F., Burls, N. J., Reason, C. J. C., and McPhaden, M. J. (2014). Variability in the South Atlantic Anticyclone and the Atlantic Niño Mode. *J. Clim.* 27, 8135–8150. doi:10.1175/JCLI-D-14-00202.1.

Lübbecke, J. F., Rodríguez-Fonseca, B., Richter, I., Martín-Rey, M., Losada, T., Polo, I., et al. (2018). Equatorial Atlantic variability-Modes, mechanisms, and global teleconnections. *Wiley Interdiscip. Rev. Clim. Chang.* 9, e527. doi:10.1002/wcc.527.

Lukens, K. E., Feldstein, S. B., Yoo, C., and Lee, S. (2017). The dynamics of the extratropical response to Madden-Julian Oscillation convection. *Q. J. R. Meteorol. Soc.* 143, 1095–1106. doi:10.1002/qj.2993.

Luo, J.-J., Sasaki, W., and Masumoto, Y. (2012). Indian Ocean warming modulates Pacific climate change. *Proc. Natl. Acad. Sci.* 109, 18701–18706. doi:10.1073/pnas.1210239109.

Luterbacher, J. (2001). Extending North Atlantic Oscillation reconstructions back to 1500. *Atmos. Sci. Lett.* 2, 114–124. doi:10.1006/asle.2001.0044.

MacDonald, G. M., and Case, R. A. (2005). Variations in the Pacific Decadal Oscillation over the past millennium. *Geophys. Res. Lett.* 32, L08703. doi:10.1029/2005GL022478.

Madden, R. A. (1986). Seasonal Variations of the 40-50 Day Oscillation in the Tropics. *J. Atmos. Sci.* 43, 3138–3158. doi:10.1175/1520-0469(1986)043<3138:SVOTDO>2.0.CO;2.

Madden, R. A., and Julian, P. R. (1994). Observations of the 40–50-Day Tropical Oscillation—A Review. *Mon. Weather Rev.* 122, 814–837. doi:10.1175/1520-0493(1994)122<0814:OOTDTO>2.0.CO;2.

Maloney, E. D., and Hartmann, D. L. (2000). Modulation of Eastern North Pacific Hurricanes by the Madden–Julian Oscillation. *J. Clim.* 13, 1451–1460. doi:10.1175/1520-0442(2000)013<1451:MOENPH>2.0.CO;2.

Maloney, E. D., and Shaman, J. (2008). Intraseasonal Variability of the West African Monsoon and Atlantic ITCZ. *J. Clim.* 21, 2898–2918. doi:10.1175/2007JCLI1999.1.

Manatsa, D., Morioka, Y., Behera, S. K., Yamagata, T., and Matarira, C. H. (2013). Link between Antarctic ozone depletion and summer warming over southern Africa. *Nat. Geosci.* 6, 934–939. doi:10.1038/ngeo1968.

Manatsa, D., Mudavanhu, C., Mushore, T. D., and Mavhura, E. (2016). Linking major shifts in East Africa "short rains" to the Southern Annular Mode. *Int. J. Climatol.* 36, 1590–1599. doi:10.1002/joc.4443.

Mann, M. E., Steinman, B. A., and Miller, S. K. (2020). Absence of internal multidecadal and interdecadal oscillations in climate model simulations. *Nat. Commun.* 11, 49. doi:10.1038/s41467-019-13823-w.

Mann, M. E., Zhang, Z., Rutherford, S., Bradley, R. S., Hughes, M. K., Shindell, D., et al. (2009). Global Signatures and Dynamical Origins of the Little Ice Age and Medieval Climate Anomaly. *Science (80-.).* 326, 1256–1260. doi:10.1126/science.1177303.

Mantua, N. J., and Hare, S. R. (2002). The Pacific Decadal Oscillation. *J. Oceanogr.* 58, 35–44. doi:10.1023/A:1015820616384.

Mantua, N. J., Hare, S. R., Zhang, Y., Wallace, J. M., and Francis, R. C. (1997). A Pacific Interdecadal Climate Oscillation with Impacts on Salmon Production*. *Bull. Am. Meteorol. Soc.* 78, 1069–1080. doi:10.1175/1520-0477(1997)078<1069:APICOW>2.0.CO;2.

Mapes, B., and Neale, R. (2011). Parameterizing Convective Organization to Escape the Entrainment Dilemma. *J. Adv. Model. Earth Syst.* 3, M06004. doi:10.1029/2011MS000042.

Mariani, M., and Fletcher, M. S. (2016). The Southern Annular Mode determines interannual and centennial-scale fire activity in temperate southwest Tasmania, Australia. *Geophys. Res. Lett.* 43, 1702–1709. doi:10.1002/2016GL068082.

Marshall, G. J. (2003). Trends in the Southern Annular Mode from Observations and Reanalyses. *J. Clim.* 16, 4134–4143.

Marshall, G. J., Orr, A., and Turner, J. (2013). A Predominant Reversal in the Relationship between the SAM and East Antarctic Temperatures during the Twenty-First Century. *J. Clim.* 26, 5196–5204. doi:10.1175/JCLI-D-12-00671.1.

Marshall, G. J., Thompson, D. W. J., and Broeke, M. R. (2017). The Signature of Southern Hemisphere Atmospheric Circulation Patterns in Antarctic Precipitation. *Geophys. Res. Lett.* 44, 11,580-11,589. doi:10.1002/2017GL075998.

ACCEPTED VERSION SUBJECT TO FINAL EDITING

Martín-Rey, M., Polo, I., Rodríguez-Fonseca, B., Losada, T., and Lazar, A. (2018). Is There Evidence of Changes in Tropical Atlantic Variability Modes under AMO Phases in the Observational Record? *J. Clim.* 31, 515–536. doi:10.1175/JCLI-D-16-0459.1.

Martín-Rey, M., Rodríguez-Fonseca, B., Polo, I., and Kucharski, F. (2014). On the Atlantic–Pacific Niños connection: a multidecadal modulated mode. *Clim. Dyn.* 43, 3163–3178. doi:10.1007/s00382-014-2305-3.

Martín-Rey, M., Rodríguez-Fonseca, B., and Polo, I. (2015). Atlantic opportunities for ENSO prediction. *Geophys. Res. Lett.* 42, 6802–6810. doi:10.1002/2015GL065062.

Martin, E. R., and Thorncroft, C. D. (2014). The impact of the AMO on the West African monsoon annual cycle. *Q. J. R. Meteorol. Soc.* 140, 31–46. doi:10.1002/qj.2107.

Matthews, A. J., Hoskins, B. J., and Masutani, M. (2004). The global response to tropical heating in the Madden–Julian oscillation during the northern winter. *Q. J. R. Meteorol. Soc.* 130, 1991–2011. doi:10.1256/qj.02.123.

Matthews, T., Murphy, C., Wilby, R. L., and Harrigan, S. (2014). Stormiest winter on record for Ireland and UK. *Nat. Clim. Chang.* 4, 738–740. doi:10.1038/nclimate2336.

Mauri, A., Davis, B. A. S., Collins, P. M., and Kaplan, J. O. (2014). The influence of atmospheric circulation on the mid-Holocene climate of Europe: A data-model comparison. *Clim. Past* 10, 1925–1938. doi:10.5194/cp-10-1925-2014.

McGee, D., Donohoe, A., Marshall, J., and Ferreira, D. (2014). Changes in ITCZ location and cross-equatorial heat transport at the Last Glacial Maximum, Heinrich Stadial 1, and the mid-Holocene. *Earth Planet. Sci. Lett.* 390, 69–79. doi:https://doi.org/10.1016/j.epsl.2013.12.043.

McGregor, S., Timmermann, A., Stuecker, M. F., England, M. H., Merrifield, M., Jin, F.-F., et al. (2014). Recent Walker circulation strengthening and Pacific cooling amplified by Atlantic warming. *Nat. Clim. Chang.* 4, 888–892. doi:10.1038/nclimate2330.

McGregor, S., Timmermann, A., and Timm, O. (2010). A unified proxy for ENSO and PDO variability since 1650. *Clim. Past* 6, 1–17. doi:10.5194/cp-6-1-2010.

Meehl, G. A., Arblaster, J. M., and Loschnigg, J. (2003). Coupled Ocean–Atmosphere Dynamical Processes in the Tropical Indian and Pacific Oceans and the TBO. *J. Clim.* 16, 2138–2158. doi:10.1175/2767.1.

Meehl, G. A., and Hu, A. (2006). Megadroughts in the Indian Monsoon Region and Southwest North America and a Mechanism for Associated Multidecadal Pacific Sea Surface Temperature Anomalies. *J. Clim.* 19, 1605–1623. doi:10.1175/JCLI3675.1.

Meehl, G. A., and Teng, H. (2014). Regional precipitation simulations for the mid-1970s shift and early-2000s hiatus. *Geophys. Res. Lett.* 41, 7658–7665. doi:10.1002/2014GL061778.

Mellado-Cano, J., Barriopedro, D., García-Herrera, R., Trigo, R. M., and Hernández, A. (2019). Examining the North Atlantic Oscillation, East Atlantic pattern and jet variability since 1685. *J. Clim.* 32, 6285–6298. doi:10.1175/JCLI-D-18-0135.1.

Meyers, G., McIntosh, P., Pigot, L., and Pook, M. (2007). The Years of El Niño, La Niña, and Interactions with the Tropical Indian Ocean. *J. Clim.* 20, 2872–2880. doi:10.1175/JCLI4152.1.

Michel, S., Swingedouw, D., Chavent, M., Ortega, P., Mignot, J., and Khodri, M. (2020). Reconstructing climatic modes of variability from proxy records using ClimIndRec version 1.0. *Geosci. Model Dev.* 13, 841–858. doi:10.5194/gmd-13-841-2020.

Miyakawa, T., Satoh, M., Miura, H., Tomita, H., Yashiro, H., Noda, A. T., et al. (2014). Madden–Julian Oscillation prediction skill of a new-generation global model demonstrated using a supercomputer. *Nat. Commun.* 5, 3769. doi:10.1038/ncomms4769.

Mizuta, R., Yoshimura, H., Murakami, H., Matsueda, M., Endo, H., Ose, T., et al. (2012). Climate Simulations Using MRI-AGCM3.2 with 20-km Grid. *J. Meteorol. Soc. Japan* 90A, 233–258. doi:10.2151/jmsj.2012-A12.

Mochizuki, T., Kimoto, M., Watanabe, M., Chikamoto, Y., and Ishii, M. (2016). Interbasin effects of the Indian Ocean on Pacific decadal climate change. *Geophys. Res. Lett.* 43, 7168–7175. doi:10.1002/2016GL069940.

Mohino, E., Rodríguez-Fonseca, B., Losada, T., Gervois, S., Janicot, S., Bader, J., et al. (2011). Changes in the interannual SST-forced signals on West African rainfall. AGCM intercomparison. *Clim. Dyn.* 37, 1707–1725. doi:10.1007/s00382-011-1093-2.

Monks, S. A., Arnold, S. R., and Chipperfield, M. P. (2012). Evidence for El Niño-Southern Oscillation (ENSO) influence on Arctic CO interannual variability through biomass burning emissions. *Geophys. Res. Lett.* 39, L14804. doi:10.1029/2012GL052512.

Moon, J.-Y., Wang, B., Ha, K.-J., and Lee, J.-Y. (2013). Teleconnections associated with Northern Hemisphere summer monsoon intraseasonal oscillation. *Clim. Dyn.* 40, 2761–2774. doi:10.1007/s00382-012-1394-0.

Moore, G. W. K., Halfar, J., Majeed, H., Adey, W., and Kronz, A. (2017). Amplification of the Atlantic Multidecadal Oscillation associated with the onset of the industrial-era warming. *Sci. Rep.* 7, 40861. doi:10.1038/srep40861.

ACCEPTED VERSION SUBJECT TO FINAL EDITING

Moreno, P. I., Vilanova, I., Villa-Martínez, R., Dunbar, R. B., Mucciarone, D. A., Kaplan, M. R., et al. (2018). Onset and Evolution of Southern Annular Mode-Like Changes at Centennial Timescale. *Sci. Rep.* 8, 3458. doi:10.1038/s41598-018-21836-6.

Neelin, J. D., Battisti, D. S., Hirst, A. C., Jin, F.-F., Wakata, Y., Yamagata, T., et al. (1998). ENSO theory. *J. Geophys. Res. Ocean.* 103, 14261–14290. doi:10.1029/97JC03424.

Newman, M., Alexander, M. A., Ault, T. R., Cobb, K. M., Deser, C., Di Lorenzo, E., et al. (2016). The Pacific Decadal Oscillation, Revisited. *J. Clim.* 29, 4399–4427. doi:10.1175/JCLI-D-15-0508.1.

Nicolì, D., Bellucci, A., Iovino, D., Ruggieri, P., and Gualdi, S. (2020). The impact of the AMV on Eurasian summer hydrological cycle. *Sci. Rep.* 10, 14444. doi:10.1038/s41598-020-71464-2.

Nidheesh, A. G., Lengaigne, M., Vialard, J., Izumo, T., Unnikrishnan, A. S., and Cassou, C. (2017). Influence of ENSO on the Pacific decadal oscillation in CMIP models. *Clim. Dyn.* 49, 3309–3326. doi:10.1007/s00382-016-3514-8.

Niedermeyer, E. M., Sessions, A. L., Feakins, S. J., and Mohtadi, M. (2014). Hydroclimate of the western Indo-Pacific Warm Pool during the past 24,000 years. *Proc. Natl. Acad. Sci.* 111, 9402–9406. doi:10.1073/pnas.1323585111.

Nnamchi, H. C., Latif, M., Keenlyside, N. S., Kjellsson, J., and Richter, I. (2021). Diabatic heating governs the seasonality of the Atlantic Niño. *Nat. Commun.* 12, 376. doi:10.1038/s41467-020-20452-1.

Nnamchi, H. C., Li, J., Kucharski, F., Kang, I.-S., Keenlyside, N. S., Chang, P., et al. (2015). Thermodynamic controls of the Atlantic Niño. *Nat. Commun.* 6, 8895. doi:10.1038/ncomms9895.

Nobre, P., and Srukla, J. (1996). Variations of Sea Surface Temperature, Wind Stress, and Rainfall over the Tropical Atlantic and South America. *J. Clim.* 9, 2464–2479. doi:10.1175/1520-0442(1996)009<2464:VOSSTW>2.0.CO;2.

O'Reilly, C. H., Minobe, S., Kuwano-Yoshida, A., and Woollings, T. (2017). The Gulf Stream influence on wintertime North Atlantic jet variability. *Q. J. R. Meteorol. Soc.* 143, 173–183. doi:10.1002/qj.2907.

Olsen, J., Anderson, N. J., and Knudsen, M. F. (2012). Variability of the North Atlantic Oscillation over the past 5,200 years. *Nat. Geosci.* 5, 808–812. doi:10.1038/ngeo1589.

Ortega, P., Lehner, F., Swingedouw, D., Masson-Delmotte, V., Raible, C. C., Casado, M., et al. (2015). A model-tested North Atlantic Oscillation reconstruction for the past millennium. *Nature* 523, 71–74. doi:10.1038/nature14518.

Pan, Y. H., and Oort, A. H. (1983). Global Climate Variations Connected with Sea Surface Temperature Anomalies in the Eastern Equatorial Pacific Ocean for the 1958–73 Period. *Mon. Weather Rev.* 111, 1244–1258. doi:10.1175/1520-0493(1983)111<1244:GCVCWS>2.0.CO;2.

Patricola, C. M., Saravanan, R., and Chang, P. (2014). The Impact of the El Niño–Southern Oscillation and Atlantic Meridional Mode on Seasonal Atlantic Tropical Cyclone Activity. *J. Clim.* 27, 5311–5328. doi:10.1175/JCLI-D-13-00687.1.

Peings, Y., and Magnusdottir, G. (2014). Forcing of the wintertime atmospheric circulation by the multidecadal fluctuations of the North Atlantic ocean. *Environ. Res. Lett.* 9, 034018. doi:10.1088/1748-9326/9/3/034018.

Peng, S., Robinson, W. A., Li, S., and Hoerling, M. P. (2005). Tropical Atlantic SST Forcing of Coupled North Atlantic Seasonal Responses. *J. Clim.* 18, 480–496. doi:10.1175/JCLI-3270.1.

Pepler, A. S. (2016). Seasonal climate summary southern hemisphere (summer 2015-16): strong El Niño begins to weaken. *J. South. Hemisph. Earth Syst. Sci.* 66, 361–379. doi:10.22499/3.6604.001.

Pepler, A., Timbal, B., Rakich, C., and Coutts-Smith, A. (2014). Indian Ocean Dipole Overrides ENSO's Influence on Cool Season Rainfall across the Eastern Seaboard of Australia. *J. Clim.* 27, 3816–3826. doi:10.1175/JCLI-D-13-00554.1.

Philander, S. G. (1990). El Niño, La Niña, and the southern oscillation, 293 pp. *San Diego, CA Acad.*

Philander, S. G. H. (1983). El Niño Southern Oscillation phenomena. *Nature* 302, 295–301. doi:10.1038/302295a0.

Pillai, P. A., Nair, R. C., and Vidhya, C. V (2019). Recent changes in the prominent modes of Indian Ocean dipole in response to the tropical Pacific Ocean SST patterns. *Theor. Appl. Climatol.* 138, 941–951. doi:10.1007/s00704-019-02875-z.

Pohl, B., and Camberlin, P. (2006). Influence of the Madden–Julian Oscillation on East African rainfall. I: Intraseasonal variability and regional dependency. *Q. J. R. Meteorol. Soc.* 132, 2521–2539. doi:10.1256/qj.05.104.

Polo, I., Lazar, A., Rodriguez-Fonseca, B., and Mignot, J. (2015). Growth and decay of the equatorial Atlantic SST mode by means of closed heat budget in a coupled general circulation model. *Front. Earth Sci.* 3, 37. doi:10.3389/feart.2015.00037.

Polo, I., Rodríguez-Fonseca, B., Losada, T., and García-Serrano, J. (2008). Tropical Atlantic Variability Modes (1979–2002). Part I: Time-Evolving SST Modes Related to West African Rainfall. *J. Clim.* 21, 6457–6475. doi:10.1175/2008JCLI2607.1.

ACCEPTED VERSION SUBJECT TO FINAL EDITING

Pottapinjara, V., Girishkumar, M. S., Ravichandran, M., and Murtugudde, R. (2014). Influence of the Atlantic zonal mode on monsoon depressions in the Bay of Bengal during boreal summer. *J. Geophys. Res. Atmos.* 119, 6456–6469. doi:10.1002/2014JD021494.

Pottapinjara, V., Girishkumar, M. S., Sivareddy, S., Ravichandran, M., and Murtugudde, R. (2016). Relation between the upper ocean heat content in the equatorial Atlantic during boreal spring and the Indian monsoon rainfall during June-September. *Int. J. Climatol.* 36, 2469–2480. doi:10.1002/joc.4506.

Power, S., Casey, T., Folland, C., Colman, A., and Mehta, V. (1999). Inter-decadal modulation of the impact of ENSO on Australia. *Clim. Dyn.* 15, 319–324. doi:10.1007/s003820050284.

Power, S., and Colman, R. (2006). Multi-year predictability in a coupled general circulation model. *Clim. Dyn.* 26, 247–272. doi:10.1007/s00382-005-0055-y.

Prabhu, A., Kripalani, R., Oh, J., and Preethi, B. (2017). Can the Southern annular mode influence the Korean summer monsoon rainfall? *Asia-Pacific J. Atmos. Sci.* 53, 217–228. doi:10.1007/s13143-017-0029-0.

Qiu, B., Schneider, N., and Chen, S. (2007). Coupled Decadal Variability in the North Pacific: An Observationally Constrained Idealized Model*. *J. Clim.* 20, 3602–3620. doi:10.1175/JCLI4190.1.

Ratnam, J. V, Behera, S. K., Masumoto, Y., and Yamagata, T. (2014). Remote Effects of El Niño and Modoki Events on the Austral Summer Precipitation of Southern Africa. *J. Clim.* 27, 3802–3815. doi:10.1175/JCLI-D-13-00431.1.

Raut, B. A., Jakob, C., and Reeder, M. J. (2014). Rainfall Changes over Southwestern Australia and Their Relationship to the Southern Annular Mode and ENSO. *J. Clim.* 27, 5801–5814. doi:10.1175/JCLI-D-13-00773.1.

Richter, I., Behera, S. K., Doi, T., Taguchi, B., Masumoto, Y., and Xie, S.-P. (2014). What controls equatorial Atlantic winds in boreal spring? *Clim. Dyn.* 43, 3091–3104. doi:10.1007/s00382-014-2170-0.

Richter, I., Behera, S. K., Masumoto, Y., Taguchi, B., Sasaki, H., and Yamagata, T. (2013). Multiple causes of interannual sea surface temperature variability in the equatorial Atlantic Ocean. *Nat. Geosci.* 6, 43–47. doi:10.1038/ngeo1660.

Rimbu, N., Lohmann, G., and Ionita, M. (2014). Interannual to multidecadal Euro-Atlantic blocking variability during winter and its relationship with extreme low temperatures in Europe. *J. Geophys. Res. Atmos.* 119, 13,621-13,636. doi:10.1002/2014JD021983.

Risbey, J. S., Pook, M. J., McIntosh, P. C., Wheeler, M. C., and Hendon, H. H. (2009). On the Remote Drivers of Rainfall Variability in Australia. *Mon. Weather Rev.* 137, 3233–3253. doi:10.1175/2009MWR2861.1.

Rivière, G., and Drouard, M. (2015). Understanding the contrasting North Atlantic Oscillation anomalies of the winters of 2010 and 2014. *Geophys. Res. Lett.* 42, 6868–6875. doi:10.1002/2015GL065493.

Rodrigues, R. R., Campos, E. J. D., and Haarsma, R. (2015). The Impact of ENSO on the South Atlantic Subtropical Dipole Mode. *J. Clim.* 28, 2691–2705. doi:10.1175/JCLI-D-14-00483.1.

Rodríguez-Fonseca, B., Polo, I., García-Serrano, J., Losada, T., Mohino, E., Mechoso, C. R., et al. (2009). Are Atlantic Niños enhancing Pacific ENSO events in recent decades? *Geophys. Res. Lett.* 36, L20705. doi:10.1029/2009GL040048.

Roxy, M. K., Dasgupta, P., McPhaden, M. J., Suematsu, T., Zhang, C., and Kim, D. (2019). Twofold expansion of the Indo-Pacific warm pool warps the MJO life cycle. *Nature* 575, 647–651. doi:10.1038/s41586-019-1764-4.

Ruiz-Barradas, A., Carton, J. A., and Nigam, S. (2000). Structure of Interannual-to-Decadal Climate Variability in the Tropical Atlantic Sector. *J. Clim.* 13, 3285–3297. doi:10.1175/1520-0442(2000)013<3285:SOITDC>2.0.CO;2.

Ruprich-Robert, Y., Msadek, R., Castruccio, F., Yeager, S., Delworth, T., and Danabasoglu, G. (2017). Assessing the Climate Impacts of the Observed Atlantic Multidecadal Variability Using the GFDL CM2.1 and NCAR CESM1 Global Coupled Models. *J. Clim.* 30, 2785–2810. doi:10.1175/JCLI-D-16-0127.1.

Sabeerali, C. T., Ajayamohan, R. S., and Rao, S. A. (2019). Loss of predictive skill of indian summer monsoon rainfall in NCEP CFSv2 due to misrepresentation of Atlantic zonal mode. *Clim. Dyn.* 52, 4599–4619. doi:10.1007/s00382-018-4390-1.

Saji, N. H., Goswami, B. N., Vinayachandran, P. N., and Yamagata, T. (1999). A dipole mode in the tropical Indian Ocean. *Nature* 401, 360–363. doi:10.1038/43854.

Saji, N. H., Xie, S.-P., and Yamagata, T. (2006). Tropical Indian Ocean Variability in the IPCC Twentieth-Century Climate Simulations*. *J. Clim.* 19, 4397–4417. doi:10.1175/JCLI3847.1.

Saji, N. H., and Yamagata, T. (2003a). Structure of SST and Surface Wind Variability during Indian Ocean Dipole Mode Events: COADS Observations*. *J. Clim.* 16, 2735–2751. doi:10.1175/1520-0442(2003)016<2735:SOSASW>2.0.CO;2.

Saji, N., and Yamagata, T. (2003b). Possible impacts of Indian Ocean Dipole mode events on global climate. *Clim. Res.* 25, 151–169. doi:10.3354/cr025151.

ACCEPTED VERSION SUBJECT TO FINAL EDITING

Sanchez-Gomez, E., Terray, L., and Joly, B. (2008). Intra-seasonal atmospheric variability and extreme precipitation events in the European-Mediterranean region. *Geophys. Res. Lett.* 35, L15708. doi:10.1029/2008GL034515.

Schneider, N., and Cornuelle, B. D. (2005). The Forcing of the Pacific Decadal Oscillation. *J. Clim.* 18, 4355–4373. doi:10.1175/JCLI3527.1.

Schott, F. A., Xie, S.-P., and McCreary, J. P. (2009). Indian Ocean circulation and climate variability. *Rev. Geophys.* 47, RG1002. doi:10.1029/2007RG000245.

Screen, J. A., Deser, C., Smith, D. M., Zhang, X., Blackport, R., Kushner, P. J., et al. (2018). Consistency and discrepancy in the atmospheric response to Arctic sea-ice loss across climate models. *Nat. Geosci.* 11, 155–163. doi:10.1038/s41561-018-0059-y.

Seager, R., Kushnir, Y., Visbeck, M., Naik, N., Miller, J., Krahmann, G., et al. (2000). Causes of Atlantic Ocean Climate Variability between 1958 and 1998*. *J. Clim.* 13, 2845–2862. doi:10.1175/1520-0442(2000)013<2845:COAOCV>2.0.CO;2.

Sen Gupta, A., and England, M. H. (2006). Coupled Ocean–Atmosphere–Ice Response to Variations in the Southern Annular Mode. *J. Clim.* 19, 4457–4486. doi:10.1175/JCLI3843.1.

Shakun, J. D., and Shaman, J. (2009). Tropical origins of North and South Pacific decadal variability. *Geophys. Res. Lett.* 36, L19711. doi:10.1029/2009GL040313.

Shen, C., Wang, W.-C., Gong, W., and Hao, Z. (2006). A Pacific Decadal Oscillation record since 1470 AD reconstructed from proxy data of summer rainfall over eastern China. *Geophys. Res. Lett.* 33, L03702. doi:10.1029/2005GL024804.

Silvestri, G. E., and Vera, C. S. (2003). Antarctic Oscillation signal on precipitation anomalies over southeastern South America. *Geophys. Res. Lett.* 30, 2115. doi:10.1029/2003GL018277.

Simpson, I. R., Deser, C., McKinnon, K. A., and Barnes, E. A. (2018). Modeled and Observed Multidecadal Variability in the North Atlantic Jet Stream and Its Connection to Sea Surface Temperatures. *J. Clim.* 31, 8313–8338. doi:10.1175/JCLI-D-18-0168.1.

Singh, H. K. A., Hakim, G. J., Tardif, R., Emile-Geay, J., and Noone, D. C. (2018). Insights into Atlantic multidecadal variability using the Last Millennium Reanalysis framework. *Clim. Past* 14, 157–174. doi:10.5194/cp-14-157-2018.

Sjolte, J., Sturm, C., Adolphi, F., Vinther, B. M., Werner, M., Lohmann, G., et al. (2018). Solar and volcanic forcing of North Atlantic climate inferred from a process-based reconstruction. *Clim. Past* 14, 1179–1194. doi:10.5194/cp-14-1179-2018.

Smith, D. M., Scaife, A. A., and Kirtman, B. P. (2012). What is the current state of scientific knowledge with regard to seasonal and decadal forecasting? *Environ. Res. Lett.* 7, 015602. doi:10.1088/1748-9326/7/1/015602.

Spence, P., Griffies, S. M., England, M. H., Hogg, A. M., Saenko, O. A., and Jourdain, N. C. (2014). Rapid subsurface warming and circulation changes of Antarctic coastal waters by poleward shifting winds. *Geophys. Res. Lett.* 41, 4601–4610. doi:10.1002/2014GL060613.

Spensberger, C., Reeder, M. J., Spengler, T., and Patterson, M. (2020). The Connection between the Southern Annular Mode and a Feature-Based Perspective on Southern Hemisphere Midlatitude Winter Variability. *J. Clim.* 33, 115–129. doi:10.1175/JCLI-D-19-0224.1.

Sperber, K. R., and Annamalai, H. (2008). Coupled model simulations of boreal summer intraseasonal (30–50 day) variability, Part 1: Systematic errors and caution on use of metrics. *Clim. Dyn.* 31, 345–372. doi:10.1007/s00382-008-0367-9.

Sperber, K. R., Annamalai, H., Kang, I.-S., Kitoh, A., Moise, A., Turner, A., et al. (2013). The Asian summer monsoon: an intercomparison of CMIP5 vs. CMIP3 simulations of the late 20th century. *Clim. Dyn.* 41, 2711–2744. doi:10.1007/s00382-012-1607-6.

Stan, C., Straus, D. M., Frederiksen, J. S., Lin, H., Maloney, E. D., and Schumacher, C. (2017). Review of Tropical-Extratropical Teleconnections on Intraseasonal Time Scales. *Rev. Geophys.* 55, 902–937. doi:10.1002/2016RG000538.

Steinman, B. A., Mann, M. E., and Miller, S. K. (2015). Atlantic and Pacific multidecadal oscillations and Northern Hemisphere temperatures. *Science (80-.).* 347, 988–991. doi:10.1126/science.1257856.

Stephenson, D. B., Wanner, H., Brönnimann, S., and Luterbacher, J. (2003). "The history of scientific research on the North Atlantic Oscillation," in *The North Atlantic Oscillation: Climatic Significance and Environmental Impact*, eds. J. W. Hurrell, Y. Kushnir, G. Ottersen, and M. Visbeck, 37–50. doi:10.1029/134GM02.

Stuecker, M. F. (2018). Revisiting the Pacific Meridional Mode. *Sci. Rep.* 8, 3216. doi:10.1038/s41598-018-21537-0.

Stuecker, M. F., Timmermann, A., Jin, F., Chikamoto, Y., Zhang, W., Wittenberg, A. T., et al. (2017). Revisiting ENSO/Indian Ocean Dipole phase relationships. *Geophys. Res. Lett.* 44, 2481–2492. doi:10.1002/2016GL072308.

ACCEPTED VERSION SUBJECT TO FINAL EDITING

Subramanian, A. C., Balmaseda, M. A., Centurioni, L., Chattopadhyay, R., Cornuelle, B. D., DeMott, C., et al. (2019). Ocean Observations to Improve Our Understanding, Modeling, and Forecasting of Subseasonal-to-Seasonal Variability. *Front. Mar. Sci.* 6, 427. doi:10.3389/fmars.2019.00427.

Sutton, R. T., and Dong, B. (2012). Atlantic Ocean influence on a shift in European climate in the 1990s. *Nat. Geosci.* 5, 788–792. doi:10.1038/ngeo1595.

Sutton, R. T., McCarthy, G. D., Robson, J., Sinha, B., Archibald, A. T., and Gray, L. J. (2018). Atlantic Multidecadal Variability and the U.K. ACSIS Program. *Bull. Am. Meteorol. Soc.* 99, 415–425. doi:10.1175/BAMS-D-16-0266.1.

Svendsen, L., Hetzinger, S., Keenlyside, N., and Gao, Y. (2014). Marine-based multiproxy reconstruction of Atlantic multidecadal variability. *Geophys. Res. Lett.* 41, 1295–1300. doi:10.1002/2013GL059076.

Swart, N. C., Fyfe, J. C., Gillett, N., and Marshall, G. J. (2015). Comparing Trends in the Southern Annular Mode and Surface Westerly Jet. *J. Clim.* 28, 8840–8859. doi:10.1175/JCLI-D-15-0334.1.

Swingedouw, D., Mignot, J., Ortega, P., Khodri, M., Menegoz, M., Cassou, C., et al. (2017). Impact of explosive volcanic eruptions on the main climate variability modes. *Glob. Planet. Change* 150, 24–45. doi:10.1016/j.gloplacha.2017.01.006.

Taguchi, B., Xie, S.-P., Schneider, N., Nonaka, M., Sasaki, H., and Sasai, Y. (2007). Decadal Variability of the Kuroshio Extension: Observations and an Eddy-Resolving Model Hindcast*. *J. Clim.* 20, 2357–2377. doi:10.1175/JCLI4142.1.

Tandon, N. F., and Kushner, P. J. (2015). Does External Forcing Interfere with the AMOC's Influence on North Atlantic Sea Surface Temperature? *J. Clim.* 28, 6309–6323. doi:10.1175/JCLI-D-14-00664.1.

Taschetto, A. S., Sen Gupta, A., Hendon, H. H., Ummenhofer, C. C., and England, M. H. (2011). The Contribution of Indian Ocean Sea Surface Temperature Anomalies on Australian Summer Rainfall during El Niño Events. *J. Clim.* 24, 3734–3747. doi:10.1175/2011JCLI3885.1.

Taschetto, A. S., Ummenhofer, C. C., Stuecker, M. F., Dommenget, D., Ashok, K., Rodrigues, R. R., et al. (2020). "ENSO Atmospheric Teleconnections," in *El Niño Southern Oscillation in a Changing Climate*, eds. M. J. McPhaden, A. Santoso, and W. Cai, 309–335. doi:10.1002/9781119548164.ch14.

Terray, L. (2012). Evidence for multiple drivers of North Atlantic multi-decadal climate variability. *Geophys. Res. Lett.* 39, L19712. doi:10.1029/2012GL053046.

Thompson, D. W. J., and Wallace, J. M. (1998). The Arctic oscillation signature in the wintertime geopotential height and temperature fields. *Geophys. Res. Lett.* 25, 1297–1300. doi:10.1029/98GL00950.

Thompson, D. W. J., and Wallace, J. M. (2000a). Annular Modes in the Extratropical Circulation. Part I: Month-to-Month Variability*. *J. Clim.* 13, 1000–1016. doi:10.1175/1520-0442(2000)013<1000:AMITEC>2.0.CO;2.

Thompson, D. W. J., and Wallace, J. M. (2000b). Annular modes in the extratropical circulation. Part II: Trends. *J. Clim.* 13, 1018–1036. doi:10.1175/1520-0442(2000)013<1018:AMITEC>2.0.CO;2.

Tian, B., Waliser, D. E., Kahn, R. A., and Wong, S. (2011). Modulation of Atlantic aerosols by the Madden-Julian Oscillation. *J. Geophys. Res.* 116, D15108. doi:10.1029/2010JD015201.

Tian, B., Yung, Y. L., Waliser, D. E., Tyranowski, T., Kuai, L., Fetzer, E. J., et al. (2007). Intraseasonal variations of the tropical total ozone and their connection to the Madden-Julian Oscillation. *Geophys. Res. Lett.* 34, L08704. doi:10.1029/2007GL029451.

Timmermann, A., An, S.-I., Kug, J.-S., Jin, F.-F., Cai, W., Capotondi, A., et al. (2018). El Niño–Southern Oscillation complexity. *Nature* 559, 535–545. doi:10.1038/s41586-018-0252-6.

Ting, M., Kushnir, Y., Seager, R., and Li, C. (2009). Forced and Internal Twentieth-Century SST Trends in the North Atlantic. *J. Clim.* 22, 1469–1481. doi:10.1175/2008JCLI2561.1.

Tokinaga, H., Richter, I., and Kosaka, Y. (2019). ENSO Influence on the Atlantic Niño, Revisited: Multi-Year versus Single-Year ENSO Events. *J. Clim.* 32, 4585–4600. doi:10.1175/JCLI-D-18-0683.1.

Tokinaga, H., and Tanimoto, Y. (2004). Seasonal transition of SST anomalies in the tropical Indian Ocean during El Niño and Indian Ocean dipole years. *J. Meteorol. Soc. Japan* 82, 1007–1018. doi:10.2151/jmsj.2004.1007.

Torralba, V., Rodríguez-Fonseca, B., Mohino, E., and Losada, T. (2015). The non-stationary influence of the Atlantic and Pacific Niños on North Eastern South American rainfall. *Front. Earth Sci.* 3, 55. doi:10.3389/feart.2015.00055.

Tozuka, T., Luo, J.-J., Masson, S., and Yamagata, T. (2007). Decadal Modulations of the Indian Ocean Dipole in the SINTEX-F1 Coupled GCM. *J. Clim.* 20, 2881–2894. doi:10.1175/JCLI4168.1.

Trenberth, K. E., Caron, J. M., Stepaniak, D. P., and Worley, S. (2002). Evolution of El Niño–Southern Oscillation and global atmospheric surface temperatures. *J. Geophys. Res.* 107, 4065. doi:10.1029/2000JD000298.

Trenberth, K. E., and Shea, D. J. (2006). Atlantic hurricanes and natural variability in 2005. *Geophys. Res. Lett.* 33, L12704. doi:10.1029/2006GL026894.

ACCEPTED VERSION SUBJECT TO FINAL EDITING

Trenberth, K. E., and Stepaniak, D. P. (2001). Indices of El Niño Evolution. *J. Clim.* 14, 1697–1701. doi:10.1175/1520-0442(2001)014<1697:LIOENO>2.0.CO;2.
Troup, A. J. (1965). The 'southern oscillation.' *Q. J. R. Meteorol. Soc.* 91, 490–506. doi:10.1002/qj.49709139009.
Tung, K.-K., Chen, X., Zhou, J., and Li, K.-F. (2019). Interdecadal variability in pan-Pacific and global SST, revisited. *Clim. Dyn.* 52, 2145–2157. doi:10.1007/s00382-018-4240-1.
Tung, K.-K., and Zhou, J. (2013). Using data to attribute episodes of warming and cooling in instrumental records. *Proc. Natl. Acad. Sci.* 110, 2058–2063. doi:10.1073/pnas.1212471110.
Ueda, H., Miwa, K., and Kamae, Y. (2018). Seasonal Modulation of Tropical Cyclone Occurrence Associated with Coherent Indo-Pacific Variability during Decaying Phase of El Niño. *J. Meteorol. Soc. Japan. Ser. II* 96, 381–390. doi:10.2151/jmsj.2018-044.
Ulbrich, U., and Christoph, M. (1999). A shift of the NAO and increasing storm track activity over Europe due to anthropogenic greenhouse gas forcing. *Clim. Dyn.* 15, 551–559. doi:10.1007/s003820050299.
Vance, T. R., Roberts, J. L., Plummer, C. T., Kiem, A. S., and van Ommen, T. D. (2015). Interdecadal Pacific variability and eastern Australian megadroughts over the last millennium. *Geophys. Res. Lett.* 42, 129–137. doi:10.1002/2014GL062447.
Vera, C. S., and Osman, M. (2018). Activity of the Southern Annular Mode during 2015 – 2016 El Niño event and its impact on Southern Hemisphere climate. 38, 1288–1295. doi:10.1002/joc.5419.
Verdon, D. C., and Franks, S. W. (2006). Long-term behaviour of ENSO: Interactions with the PDO over the past 400 years inferred from paleoclimate records. *Geophys. Res. Lett.* 33, L06712. doi:10.1029/2005GL025052.
Villalba, R., Lara, A., Masiokas, M. H., Urrutia, R., Luckman, B. H., Marshall, G. J., et al. (2012). Unusual Southern Hemisphere tree growth patterns induced by changes in the Southern Annular Mode. *Nat. Geosci.* 5, 793–798. doi:10.1038/ngeo1613.
Vimont, D. J., and Kossin, J. P. (2007). The Atlantic Meridional Mode and hurricane activity. *Geophys. Res. Lett.* 34, L07709. doi:10.1029/2007GL029683.
Vitart, F. (2014). Evolution of ECMWF sub-seasonal forecast skill scores. *Q. J. R. Meteorol. Soc.* 140, 1889–1899. doi:10.1002/qj.2256.
Vitart, F. (2017). Madden-Julian Oscillation prediction and teleconnections in the S2S database. *Q. J. R. Meteorol. Soc.* 143, 2210–2220. doi:10.1002/qj.3079.
Vitart, F., and Robertson, A. W. (2018). The sub-seasonal to seasonal prediction project (S2S) and the prediction of extreme events. *npj Clim. Atmos. Sci.* 1, 3. doi:10.1038/s41612-018-0013-0.
Vittal, H., Villarini, G., and Zhang, W. (2020). Early prediction of the Indian summer monsoon rainfall by the Atlantic Meridional Mode. *Clim. Dyn.* 54, 2337–2346. doi:10.1007/s00382-019-05117-0.
Wainer, I., Prado, L. F., Khodri, M., and Otto-Bliesner, B. (2014). Reconstruction of the South Atlantic Subtropical Dipole index for the past 12,000 years from surface temperature proxy. *Sci. Rep.* 4, 5291. doi:10.1038/srep05291.
Waliser, D. E., Jin, K., Kang, I.-S., Stern, W. F., Schubert, S. D., Wu, M. L. C., et al. (2003). AGCM simulations of intraseasonal variability associated with the Asian summer monsoon. *Clim. Dyn.* 21, 423–446. doi:10.1007/s00382-003-0337-1.
Waliser, D., Sperber, K., Hendon, H., Kim, D., Maloney, E., Wheeler, M., et al. (2009). MJO Simulation Diagnostics. *J. Clim.* 22, 3006–3030. doi:10.1175/2008JCLI2731.1.
Wang, B., and Chan, J. C. L. (2002). How Strong ENSO Events Affect Tropical Storm Activity over the Western North Pacific*. *J. Clim.* 15, 1643–1658. doi:10.1175/1520-0442(2002)015<1643:HSEEAT>2.0.CO;2.
Wang, B., Wu, R., and Fu, X. (2000). Pacific–East Asian Teleconnection: How Does ENSO Affect East Asian Climate? *J. Clim.* 13, 1517–1536. doi:10.1175/1520-0442(2000)013<1517:PEATHD>2.0.CO;2.
Wang, B., Xiang, B., and Lee, J.-Y. (2013). Subtropical High predictability establishes a promising way for monsoon and tropical storm predictions. *Proc. Natl. Acad. Sci.* 110, 2718–2722. doi:10.1073/pnas.1214626110.
Wang, C. (2018). A review of ENSO theories. *Natl. Sci. Rev.* 5, 813–825. doi:10.1093/nsr/nwy104.
Wang, C., Kucharski, F., Barimalala, R., and Bracco, A. (2009). Teleconnections of the tropical Atlantic to the tropical Indian and Pacific Oceans: A review of recent findings. *Meteorol. Zeitschrift* 18, 445–454. doi:10.1127/0941-2948/2009/0394.
Wang, J., Yang, B., Ljungqvist, F. C., Luterbacher, J., Osborn, T. J., Briffa, K. R., et al. (2017a). Internal and external forcing of multidecadal Atlantic climate variability over the past 1,200 years. *Nat. Geosci.* 10, 512–517. doi:10.1038/ngeo2962.
Wang, L., Yu, J.-Y., and Paek, H. (2017b). Enhanced biennial variability in the Pacific due to Atlantic capacitor effect. *Nat. Commun.* 8, 14887. doi:10.1038/ncomms14887.

ACCEPTED VERSION SUBJECT TO FINAL EDITING

Ward, D. S., Shevliakova, E., Malyshev, S., Lamarque, J.-F., and Wittenberg, A. T. (2016). Variability of fire emissions on interannual to multi-decadal timescales in two Earth System models. *Environ. Res. Lett.* 11, 125008. doi:10.1088/1748-9326/11/12/125008.

Watanabe, M., and Jin, F. (2002). Role of Indian Ocean warming in the development of Philippine Sea anticyclone during ENSO. *Geophys. Res. Lett.* 29, 1478. doi:10.1029/2001GL014318.

Waugh, D. W., Primeau, F., DeVries, T., and Holzer, M. (2013). Recent Changes in the Ventilation of the Southern Oceans. *Science (80-.).* 339, 568–570. doi:10.1126/science.1225411.

Weare, B. C. (1979). A Statistical Study of the Relationships between Ocean Surface Temperatures and the Indian Monsoon. *J. Atmos. Sci.* 36, 2279–2291. doi:10.1175/1520-0469(1979)036<2279:ASSOTR>2.0.CO;2.

Webster, P. J., and Hoyos, C. D. (2010). Beyond the spring barrier? *Nat. Geosci.* 3, 152–153. doi:10.1038/ngeo800.

Whan, K., and Zwiers, F. (2017). The impact of ENSO and the NAO on extreme winter precipitation in North America in observations and regional climate models. *Clim. Dyn.* 48, 1401–1411. doi:10.1007/s00382-016-3148-x.

Wheeler, M. C., and Hendon, H. H. (2004). An All-Season Real-Time Multivariate MJO Index: Development of an Index for Monitoring and Prediction. *Mon. Weather Rev.* 132, 1917–1932. doi:10.1175/1520-0493(2004)132<1917:AARMMI>2.0.CO;2.

Wheeler, M. C., Hendon, H. H., Cleland, S., Meinke, H., and Donald, A. (2009). Impacts of the Madden–Julian Oscillation on Australian Rainfall and Circulation. *J. Clim.* 22, 1482–1498. doi:10.1175/2008JCLI2595.1.

Wheeler, M. C., Kim, H.-J., Lee, J.-Y., and Gottschalck, J. C. (2017). "Real-Time Forecasting of Modes of Tropical Intraseasonal Variability: The Madden-Julian and Boreal Summer Intraseasonal Oscillations," in *World Scientific Series on Asia-Pacific Weather and Climate*, 131–138. doi:10.1142/9789813200913_0010.

Wiedermann, M., Radebach, A., Donges, J. F., Kurths, J., and Donner, R. V (2016). A climate network-based index to discriminate different types of El Niño and La Niña. *Geophys. Res. Lett.* 43, 7176–7185. doi:10.1002/2016GL069119.

Williams, B., Halfar, J., Delong, K. L., Smith, E., Steneck, R., Lebednik, P. A., et al. (2017). North Pacific twentieth century decadal-scale variability is unique for the past 342 years. *Geophys. Res. Lett.* 44, 3761–3769. doi:10.1002/2017GL073138.

Wills, R. C. J., Battisti, D. S., Proistosescu, C., Thompson, L., Hartmann, D. L., and Armour, K. C. (2019). Ocean Circulation Signatures of North Pacific Decadal Variability. *Geophys. Res. Lett.* 46, 1690–1701. doi:10.1029/2018GL080716.

Wills, R. C., Schneider, T., Wallace, J. M., Battisti, D. S., and Hartmann, D. L. (2018). Disentangling Global Warming, Multidecadal Variability, and El Niño in Pacific Temperatures. *Geophys. Res. Lett.* 45, 2487–2496. doi:10.1002/2017GL076327.

Wittenberg, A. T. (2009). Are historical records sufficient to constrain ENSO simulations? *Geophys. Res. Lett.* 36, L12702. doi:10.1029/2009GL038710.

Woollings, T., Czuchnicki, C., and Franzke, C. (2014). Twentieth century North Atlantic jet variability. *Q. J. R. Meteorol. Soc.* 140, 783–791. doi:10.1002/qj.2197.

Woollings, T., Franzke, C., Hodson, D. L. R., Dong, B., Barnes, E. A., Raible, C. C., et al. (2015). Contrasting interannual and multidecadal NAO variability. *Clim. Dyn.* 45, 539–556. doi:10.1007/s00382-014-2237-y.

Woollings, T., Hannachi, A., Hoskins, B., and Turner, A. (2010). A Regime View of the North Atlantic Oscillation and Its Response to Anthropogenic Forcing. *J. Clim.* 23, 1291–1307. doi:10.1175/2009JCLI3087.1.

Wu, L., He, F., Liu, Z., and Li, C. (2007). Atmospheric Teleconnections of Tropical Atlantic Variability: Interhemispheric, Tropical–Extratropical, and Cross-Basin Interactions. *J. Clim.* 20, 856–870. doi:10.1175/JCLI4019.1.

Wu, T., Hu, A., Gao, F., Zhang, J., and Meehl, G. A. (2019). New insights into natural variability and anthropogenic forcing of global/regional climate evolution. *npj Clim. Atmos. Sci.* 2, 18. doi:10.1038/s41612-019-0075-7.

Xavier, P. K. (2012). Intraseasonal Convective Moistening in CMIP3 Models. *J. Clim.* 25, 2569–2577. doi:10.1175/JCLI-D-11-00427.1.

Xavier, P. K., Duvel, J.-P., Braconnot, P., and Doblas-Reyes, F. J. (2010). An Evaluation Metric for Intraseasonal Variability and its Application to CMIP3 Twentieth-Century Simulations. *J. Clim.* 23, 3497–3508. doi:10.1175/2010JCLI3260.1.

Xie, S.-P., Hu, K., Hafner, J., Tokinaga, H., Du, Y., Huang, G., et al. (2009). Indian Ocean Capacitor Effect on Indo–Western Pacific Climate during the Summer following El Niño. *J. Clim.* 22, 730–747. doi:10.1175/2008JCLI2544.1.

Yan, X., Zhang, R., and Knutson, T. R. (2019). A Multivariate AMV Index and Associated Discrepancies Between Observed and CMIP5 Externally Forced AMV. *Geophys. Res. Lett.* 46, 4421–4431. doi:10.1029/2019GL082787.

ACCEPTED VERSION SUBJECT TO FINAL EDITING

Yang, Y., Li, J., Wu, L., Kosaka, Y., Du, Y., Sun, C., et al. (2017). Decadal Indian Ocean dipolar variability and its relationship with the tropical Pacific. *Adv. Atmos. Sci.* 34, 1282–1289. doi:10.1007/s00376-017-7009-2.

Yasunari, T. (1980). A Quasi-Stationary Appearance of 30 to 40 Day Period in the Cloudiness Fluctuations during the Summer Monsoon over India. *J. Meteorol. Soc. Japan. Ser. II* 58, 225–229. doi:10.2151/jmsj1965.58.3_225.

Yeager, S., and Danabasoglu, G. (2014). The Origins of Late-Twentieth-Century Variations in the Large-Scale North Atlantic Circulation. *J. Clim.* 27, 3222–3247. doi:10.1175/JCLI-D-13-00125.1.

Yeh, S.-W., Cai, W., Min, S.-K., McPhaden, M. J., Dommenget, D., Dewitte, B., et al. (2018). ENSO Atmospheric Teleconnections and Their Response to Greenhouse Gas Forcing. *Rev. Geophys.*, 77–117. doi:110.1002/2017RG000568.

Yiou, P., Jézéquel, A., Naveau, P., Otto, F. E. L., Vautard, R., and Vrac, M. (2017). A statistical framework for conditional extreme event attribution. *Adv. Stat. Climatol. Meteorol. Oceanogr.* 3, 17–31. doi:10.5194/ascmo-3-17-2017.

Yoo, C., Feldstein, S., and Lee, S. (2011). The impact of the Madden-Julian Oscillation trend on the Arctic amplification of surface air temperature during the 1979-2008 boreal winter. *Geophys. Res. Lett.* 38, L24804. doi:10.1029/2011GL049881.

Yoo, C., Lee, S., and Feldstein, S. B. (2012). Mechanisms of Arctic Surface Air Temperature Change in Response to the Madden–Julian Oscillation. *J. Clim.* 25, 5777–5790. doi:10.1175/JCLI-D-11-00566.1.

Yu, J.-Y., Paek, H., Saltzman, E. S., and Lee, T. (2015). The Early 1990s Change in ENSO – PSA – SAM Relationships and Its Impact on Southern Hemisphere Climate. *J. Clim.* 28, 9393–9408. doi:10.1175/JCLI-D-15-0335.1.

Yu, L., Zhong, S., Winkler, J. A., Zhou, M., Lenschow, D. H., Li, B., et al. (2017). Possible connections of the opposite trends in Arctic and Antarctic sea-ice cover. *Sci. Rep.* 7, 45804. doi:10.1038/srep45804.

Zebiak, S. E. (1993). Air–Sea Interaction in the Equatorial Atlantic Region. *J. Clim.* 6, 1567–1586. doi:10.1175/1520-0442(1993)006<1567:AIITEA>2.0.CO;2.

Zhang, C. (2005). Madden-Julian Oscillation. *Rev. Geophys.* 43, RG2003. doi:10.1029/2004RG000158.

Zhang, C. (2013). Madden–Julian Oscillation: Bridging Weather and Climate. *Bull. Am. Meteorol. Soc.* 94, 1849–1870. doi:10.1175/BAMS-D-12-00026.1.

Zhang, R. (2017). On the persistence and coherence of subpolar sea surface temperature and salinity anomalies associated with the Atlantic multidecadal variability. *Geophys. Res. Lett.* 44, 7865–7875. doi:10.1002/2017GL074342.

Zhang, W., Vecchi, G. A., Villarini, G., Murakami, H., Rosati, A., Yang, X., et al. (2017). Modulation of western North Pacific tropical cyclone activity by the Atlantic Meridional Mode. *Clim. Dyn.* 48, 631–647. doi:10.1007/s00382-016-3099-2.

Zhang, Y., Wallace, J. M., and Battisti, D. S. (1997). ENSO-like Interdecadal Variability: 1900–93. *J. Clim.* 10, 1004–1020. doi:10.1175/1520-0442(1997)010<1004:ELIV>2.0.CO;2.

Zhang, Y., Xie, S.-P., Kosaka, Y., and Yang, J.-C. (2018). Pacific Decadal Oscillation: Tropical Pacific Forcing versus Internal Variability. *J. Clim.* 31, 8265–8279. doi:10.1175/JCLI-D-18-0164.1.

Zhao, H., Wu, L., Wang, C., and Klotzbach, P. J. (2019). Consistent Late Onset of the Western North Pacific Tropical Cyclone Season Following major El Niño Events. *J. Meteorol. Soc. Japan. Ser. II* 97, 673–688. doi:10.2151/jmsj.2019-039.

Zhao, H., Yoshida, R., and Raga, G. B. (2015). Impact of the Madden–Julian Oscillation on Western North Pacific Tropical Cyclogenesis Associated with Large-Scale Patterns. *J. Appl. Meteorol. Climatol.* 54, 1413–1429. doi:10.1175/JAMC-D-14-0254.1.

Zhao, J., Zhan, R., Wang, Y., Xie, S.-P., and Wu, Q. (2020). Untangling impacts of global warming and Interdecadal Pacific Oscillation on long-term variability of North Pacific tropical cyclone track density. *Sci. Adv.* 6, eaba6813. doi:10.1126/sciadv.aba6813.

Zhao, J., Zhan, R., Wang, Y., and Xu, H. (2018). Contribution of the Interdecadal Pacific Oscillation to the Recent Abrupt Decrease in Tropical Cyclone Genesis Frequency over the Western North Pacific since 1998. *J. Clim.* 31, 8211–8224. doi:10.1175/JCLI-D-18-0202.1.

Zhou, J., Tung, K.-K., and Li, K.-F. (2016). Multi-decadal variability in the Greenland ice core records obtained using intrinsic timescale decomposition. *Clim. Dyn.* 47, 739–752. doi:10.1007/s00382-015-2866-9.

Zhou, S., and Miller, A. J. (2005). The Interaction of the Madden–Julian Oscillation and the Arctic Oscillation. *J. Clim.* 18, 143–159. doi:10.1175/JCLI3251.1.

Zinke, J., Pfeiffer, M., Timm, O., Dullo, W.-C., and Brummer, G. J. A. (2009). Western Indian Ocean marine and terrestrial records of climate variability: a review and new concepts on land–ocean interactions since AD 1660. *Int. J. Earth Sci.* 98, 115–133. doi:10.1007/s00531-008-0365-5.

ACCEPTED VERSION SUBJECT TO FINAL EDITING

Zinke, J., Pfeiffer, M., Timm, O., Dullo, W. –C., and Davies, G. R. (2005). Atmosphere–ocean dynamics in the Western Indian Ocean recorded in corals. *Philos. Trans. R. Soc. A Math. Phys. Eng. Sci.* 363, 121–142. doi:10.1098/rsta.2004.1482.

Zubiate, L., McDermott, F., Sweeney, C., and O'Malley, M. (2017). Spatial variability in winter NAO-wind speed relationships in western Europe linked to concomitant states of the East Atlantic and Scandinavian patterns. *Q. J. R. Meteorol. Soc.* 143, 552–562. doi:10.1002/qj.2943.

ACCEPTED VERSION SUBJECT TO FINAL EDITING

Figures

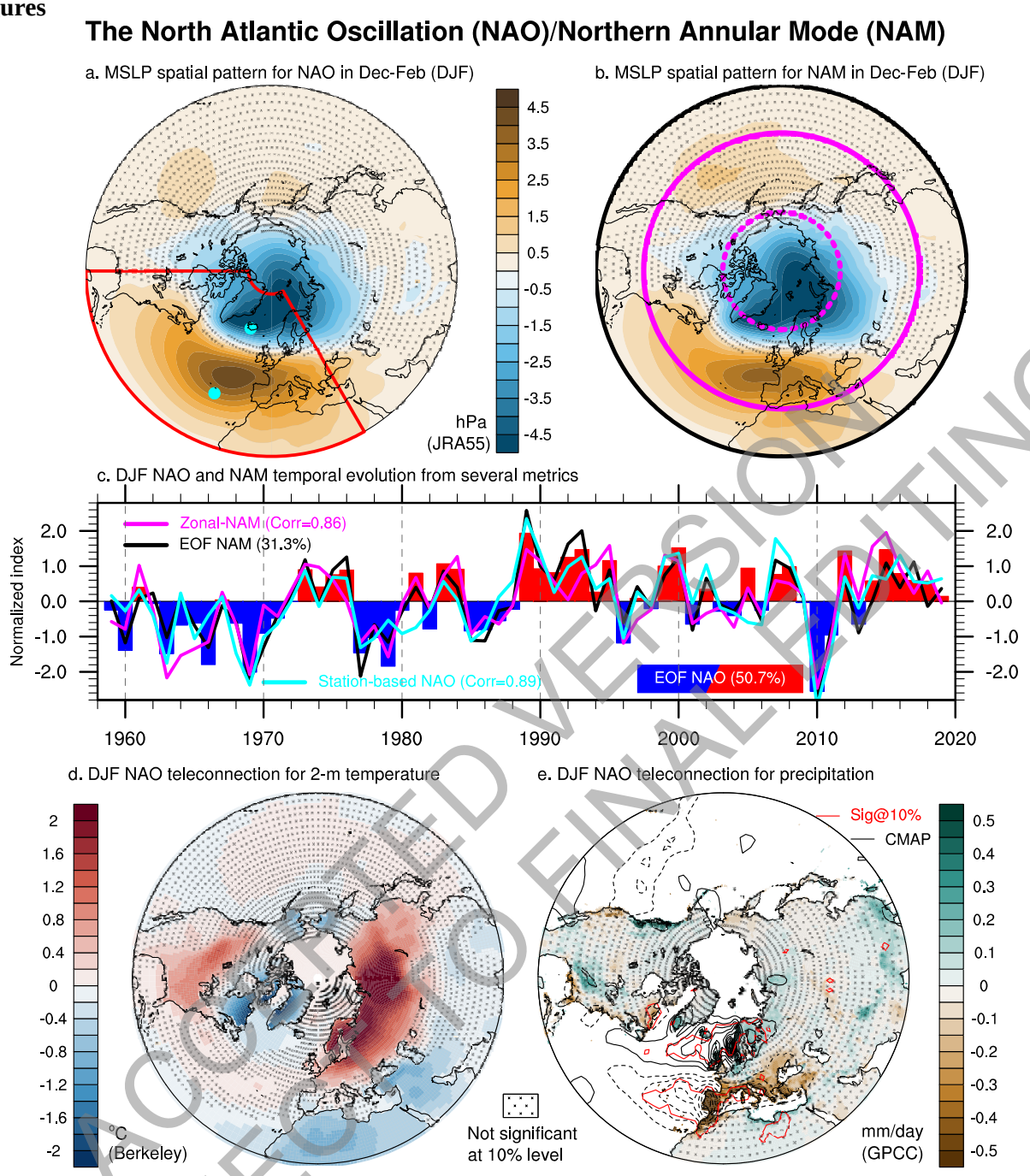

Figure AIV.1: The boreal wintertime NAO and NAM modes extracted as the leading EOF of December-January-February SLP anomalies over the North Atlantic-Europe Sector (20ºN-80ºN, 90ºW-30ºE, materialized by the red box, a) and the Northern Hemisphere (north of 20ºN, black domain, b), respectively, based on JRA-55 reanalysis over 1959-2019. (a,b) SLP anomalies regressed onto the leading principal component (PC) time series shown in (c). The NAO-PC is represented by red and blue bars, the NAM-PC by the black curve in (c); their variance explained is given in the legend. The NAO index based on weather stations (cyan dots in a) is given in cyan and the zonal-NAM index (latitude circles in b) is given in magenta. Correlation between each index and the NAO-PC timeseries is given in the legend. (d,e) Regression maps of blended SST and SAT over land from ERSST and BerkeleyEarth dataset, respectively, over for 1959-2019 (d) and of precipitation anomalies (e, shading based on GPCC for 1959-2016 and contours based on CMAP for 1979-2019 for every 0.1 mm/day). On maps, no-overlay indicates regions where the regressions are significant based on t-test accounting for false detection rate at 10% and crosses indicates no significance. Significance for CMAP precipitation is materialized by red contours in (e). All fields have been linearly detrended prior to computation.

ACCEPTED VERSION SUBJECT TO FINAL EDITING

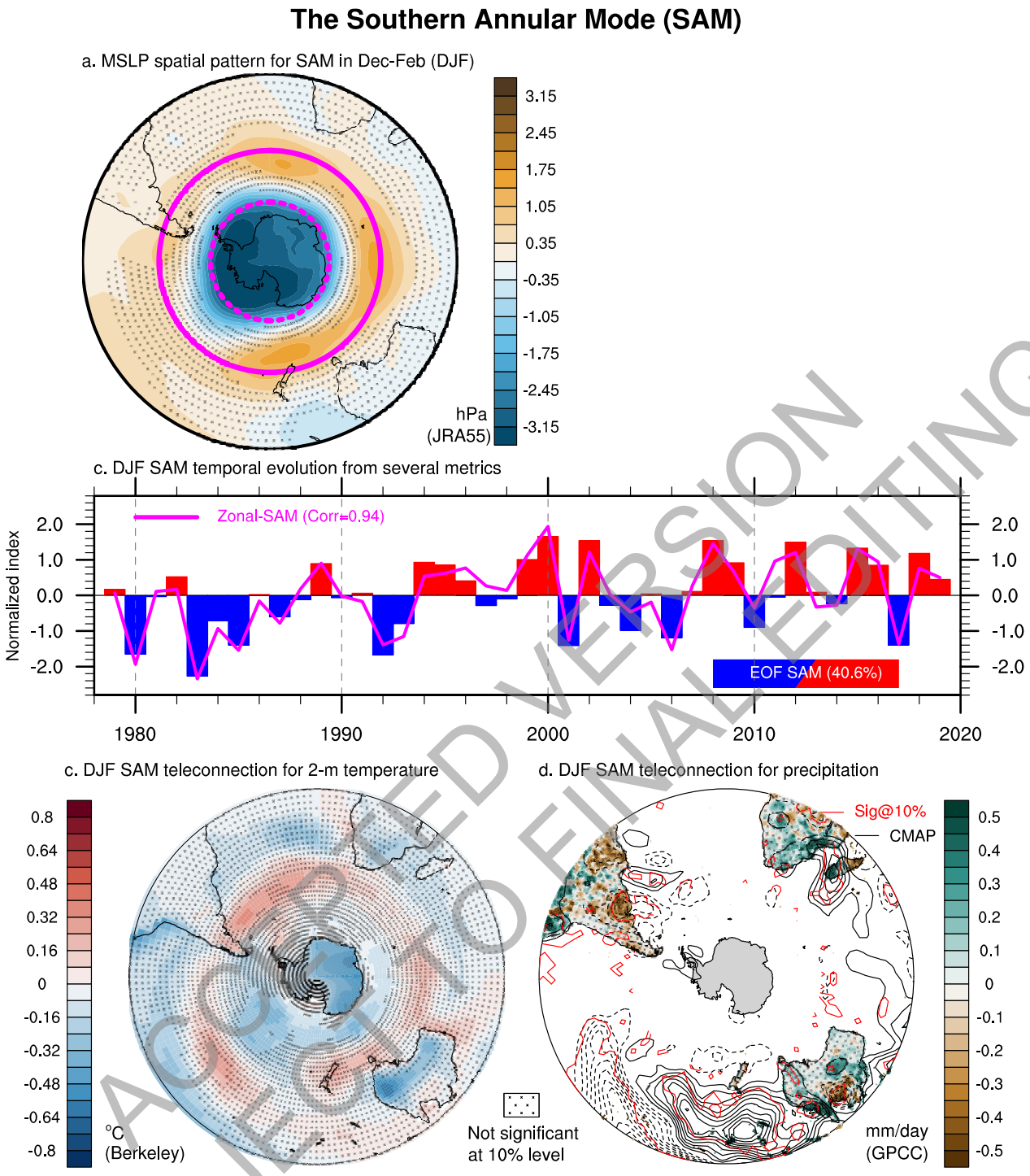

ACCEPTED VERSION SUBJECT TO FINAL EDITING

Figure AIV.2: The austral summertime SAM extracted as the leading EOF of December-January-February SLP anomalies over the Southern Hemisphere (south of 20ºS, a) based on JRA-55 reanalysis over 1979-2019. (a) SLP anomalies regressed onto the leading principal component (PC) time series shown in (b); the variance explained is given in the legend in (b). The SAM-PC is represented by red and blue bars and the zonal-SAM index (latitude circles in a) is given in magenta. Correlation between the zonal SAM index and the SAM PC timeseries is given in the legend. (c, d) Regression maps of SST and SAT over land from ERSST and BerkeleyEarth dataset, respectively, over for 1979-2019 (d) and of precipitation anomalies (e, shading based on CMAP for 1979-2016 and contours based on GPCP for 1979-2019 for every 0.1 mm/day). On maps, no-overlay indicates regions where the regressions are significant based on t-test accounting for false detection rate at 10% and crosses indicates no significance. Significance for CMAP precipitation is materialized by red contours in (d). All fields have been linearly detrended prior computation.

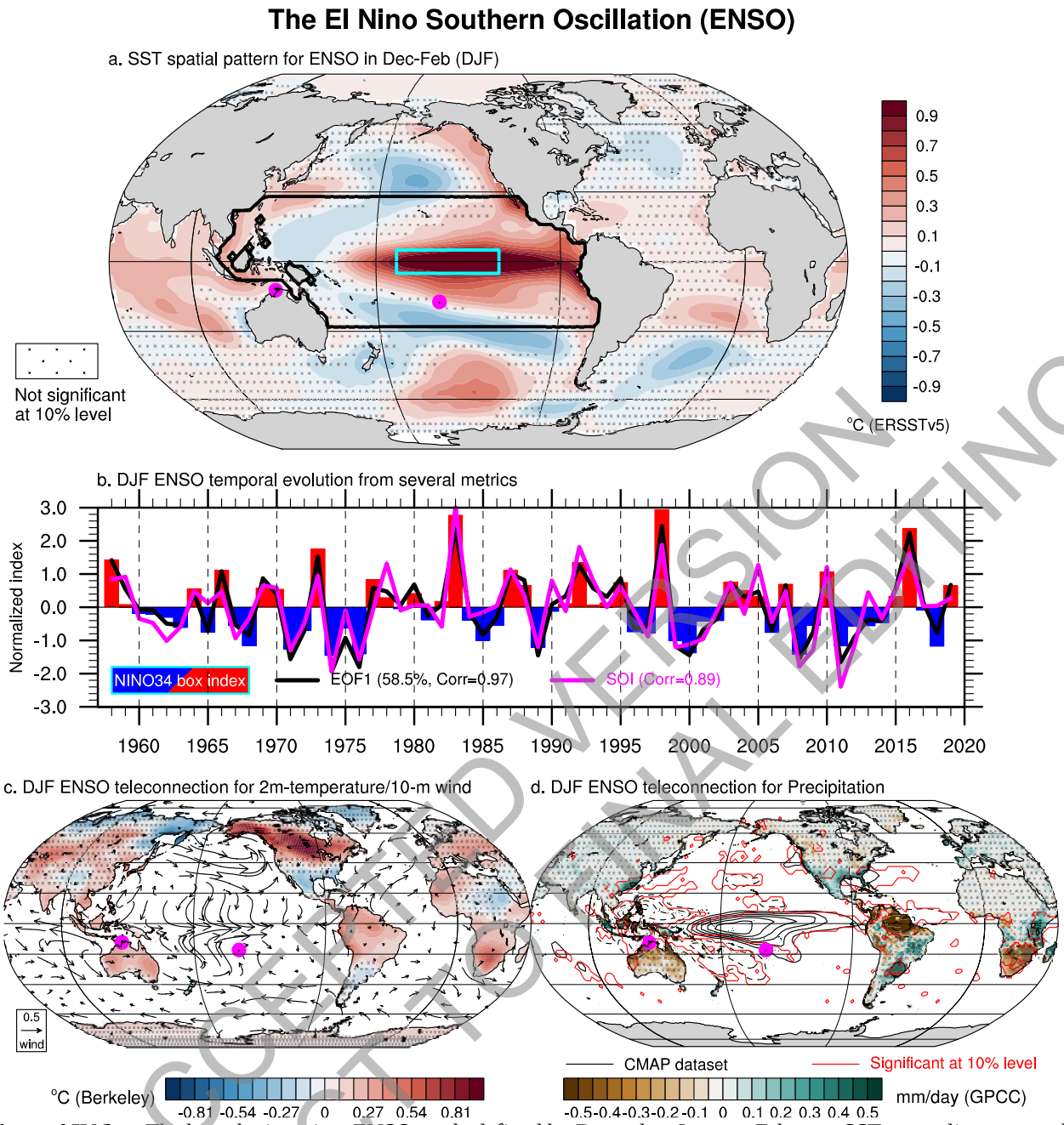

Figure AIV.3: The boreal wintertime ENSO mode defined by December-January-February SST anomalies averaged over the NINO34 region (5ºS-5ºN, 170ºW-120ºW, cyan box) or extracted as the leading EOF mode over the Tropical Pacific Ocean (the region denoted by the black box in a) for 1958-2019 using ERSSTv5. (a) SST anomalies regressed onto the NINO34 time series, which is shown in (b) as red and blue bars. Black curve in (b) represents the standardized leading principal component and the magenta curve stands for the SOI index. The percentage of explained variance of the leading EOF is given in the legend as well as the correlation between all indices and the NINO34 timeseries. (c) Same as (a) but for land SAT (shading; based on BerkeleyEarth) and 10-m level wind (arrows; based on JRA-55) anomalies over 1958-2018. (d) Same as (a) but for precipitation anomalies (shading based on GPCC for 1958-2016 and contours based on CMAP for 1979-2019 for every 0.5 mm/day). Magenta dots in (c,d) stands for the Darwin and Tahiti weather station used for the SOI computation. On maps, no-overlay indicates regions where the regressions are significant based on t-test accounting for false detection rate at 10% and crosses indicates no significance. Significance for CMAP precipitation is materialized by red contours in (d). All fields have been linearly detrended prior to computation.

ACCEPTED VERSION SUBJECT TO FINAL EDITING

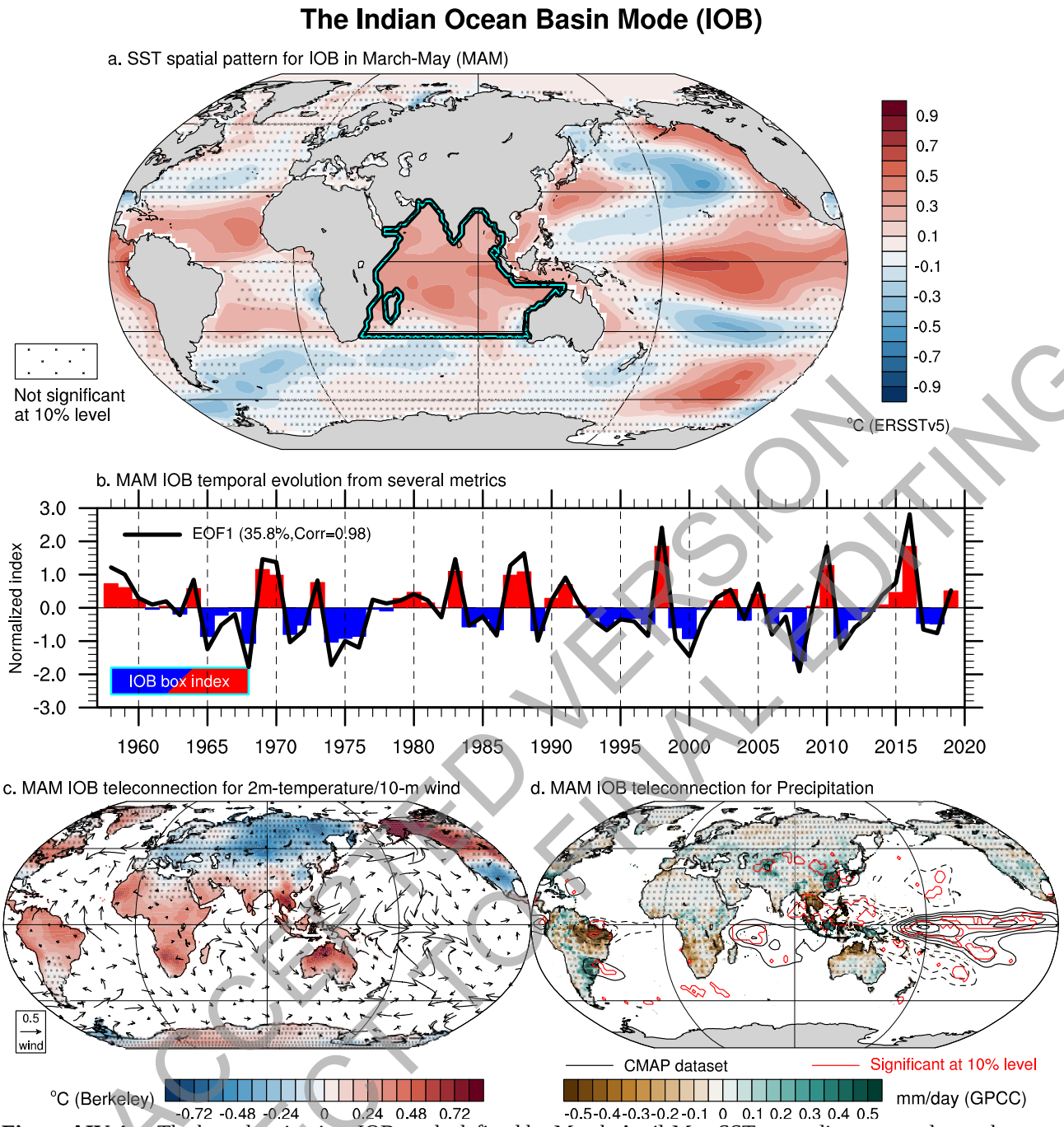

Figure AIV.4: The boreal springtime IOB mode defined by March-April-May SST anomalies averaged over the Indian Ocean (the region denoted by the cyan box in a) or extracted as the leading EOF mode over the same domain (black contour) for 1958-2019 using ERSSTv5. (a) SST anomalies regressed onto the IOB index timeseries shown in (b) in red and blue bars, while the black curve in (b) represents the leading principal component timeseries. Explained variance and correlation between indices are given in the legend in (b). (c) Same as (a) but for land SAT (shading; based on BerkeleyEarth) and 10-m level wind (arrows; based on JRA-55) anomalies for 1958-2018. (d) Same as (a) but for precipitation anomalies (shading based on GPCC for 1958-2016 and contours based on CMAP for 1979-2019 for every 0.3 mm/day). On maps, no-overlay indicates regions where the regressions are significant based on t-test accounting for false detection rate at 10% and crosses indicates no significance. Significance for CMAP precipitation is materialized by red contours in (d). All fields have been linearly detrended prior to computation.

ACCEPTED VERSION SUBJECT TO FINAL EDITING

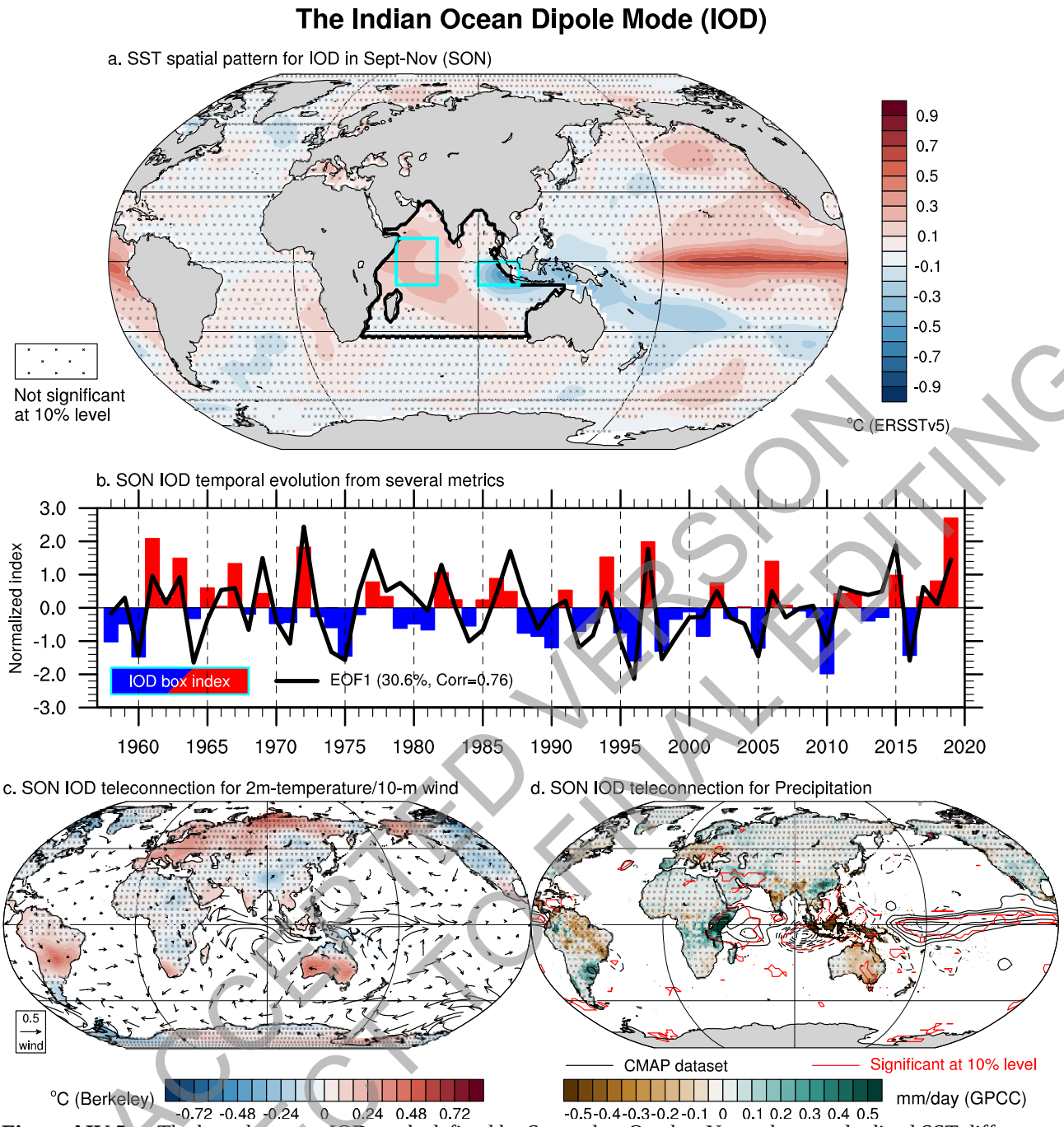

Figure AIV.5: The boreal autumn IOD mode defined by September-October-November standardized SST difference between the western (10ºS-10ºN, 50ºE-70ºE) and eastern (10ºS-0º, 90ºE-110ºE) equatorial Indian Ocean denoted by cyan boxes in (a) or extracted as the leading EOF mode over the Indian Ocean (the region denoted by black contour in a) over 1958-2019 using ERSSTv5. (a) SST anomalies regressed onto the IOD index timeseries shown in (b) in red and blue bars while the black curve represents the leading principal component timeseries. Explained variance and correlation between indices are given in the legend in (b). (c) Same as (a) but for land SAT (shading; based on BerkeleyEarth) and 10-m level wind (arrows; based on JRA-55) anomalies for 1958-2018. (d) Same as (a) but for precipitation anomalies (shading based on GPCC for 1958-2016 and contours based on CMAP for 1979-2019 for every 0.3 mm/day. On maps, no-overlay indicates regions where the regressions are significant based on t-test accounting for false detection rate at 10% and crosses indicates no significance. Significance for CMAP precipitation is materialized by red contours in (d). All fields have been linearly detrended prior to computation.

ACCEPTED VERSION SUBJECT TO FINAL EDITING

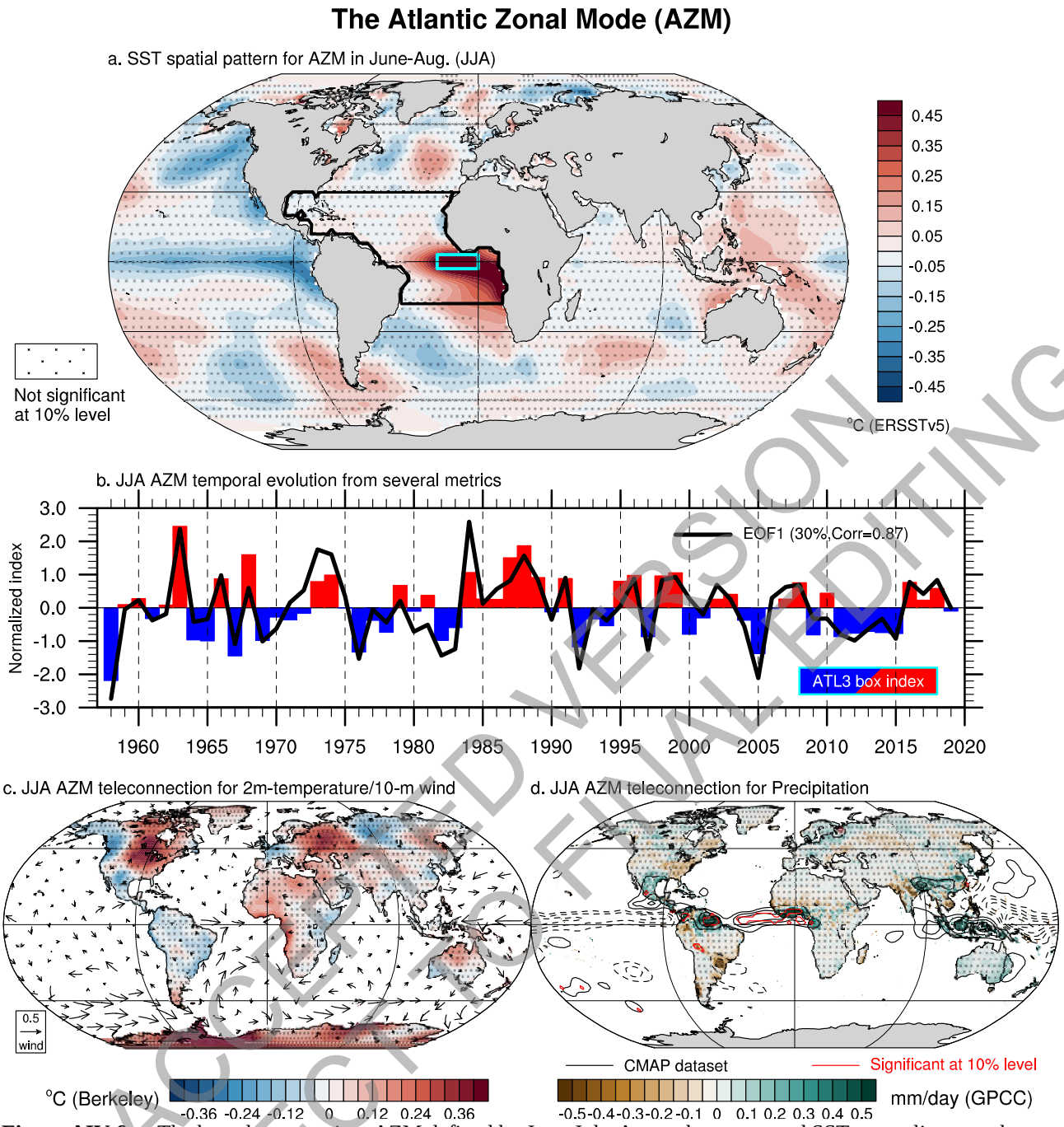

Figure AIV.6: The boreal summertime AZM defined by June-July-August box-averaged SST anomalies over the ATL3 region (3ºS-3ºN, 0º-20ºW, cyan box in a) or estimated as the leading EOF over the tropical Atlantic Ocean (the region denoted by the black box in a) for 1958-2019 using ERSSTv5. (a) SST anomalies regressed onto the ATL3 time series, which is shown in (b) as red and blue bars, while the black curve represents the leading principal component timeseries. Explained variance and correlation between indices are given in the legend in (b). (c) Same as (a) but for land SAT and 10-m level wind (arrows; based on JRA-55 for 1958-2019) anomalies. (d) Same as (a) but for precipitation anomalies (shading based on GPCC for 1958-2016 and contours based on CMAP for 1979-2019 for every 0.2 mm/day). On maps, no-overlay indicates regions where the regressions are significant based on t-test accounting for false detection rate at 10% and crosses indicates no significance. Significance for CMAP precipitation is materialized by red contours in (d). All fields have been linearly detrended prior to computation.

ACCEPTED VERSION SUBJECT TO FINAL EDITING

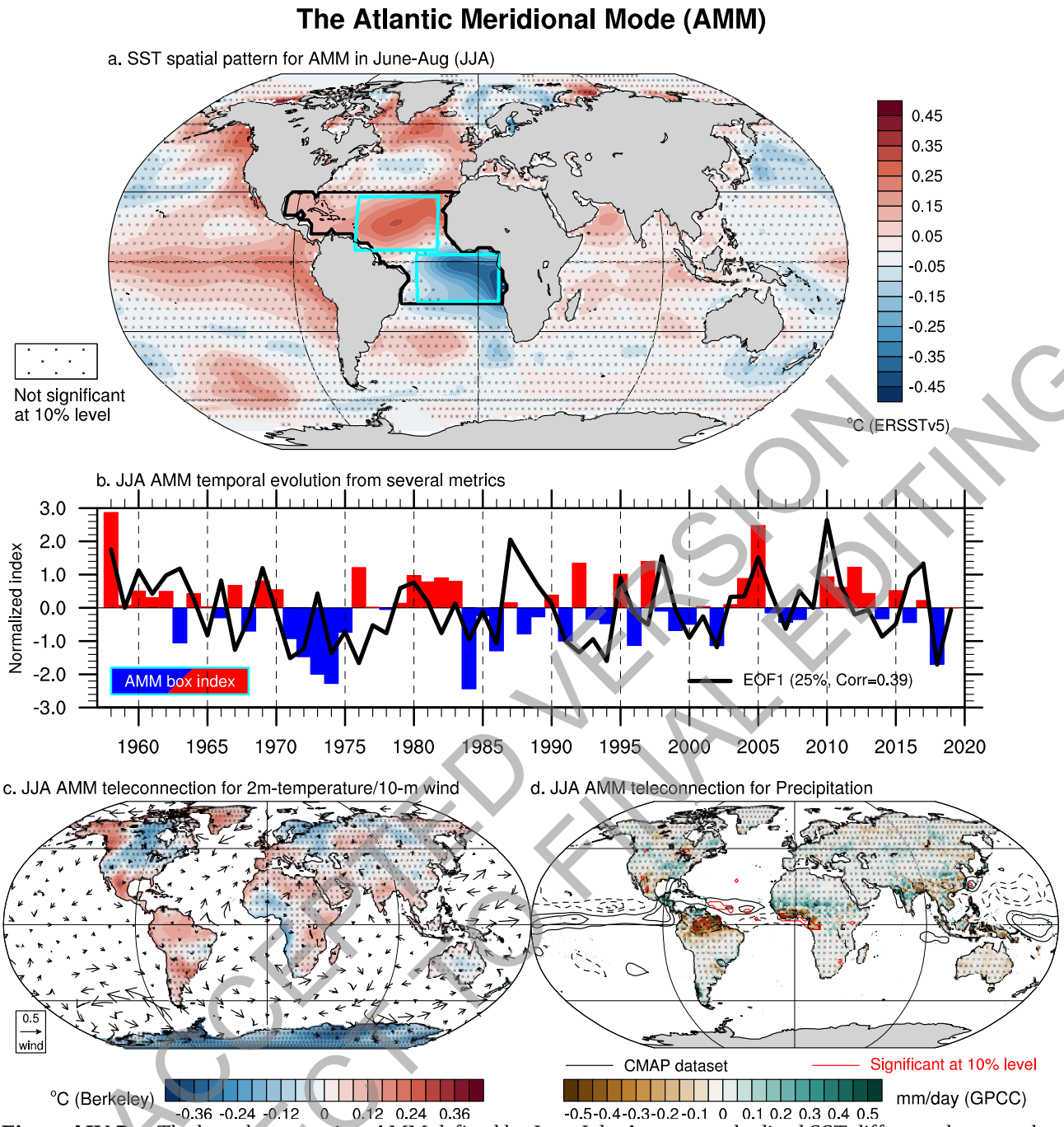

Figure AIV.7: The boreal summertime AMM defined by June-July-August standardized SST difference between the north (5ºN-30ºN, 20ºW-60ºW) and south (5ºN-20ºS, 5ºE-25ºW) tropical Atlantic Ocean shown by the cyan boxes in (a) or estimated as the leading EOF over the tropical Atlantic Ocean (the region denoted by the black box in a) for 1958-2019 using ERSSTv5. (a) SST anomalies regressed onto the AMM time series, which is shown in (b) as red and blue bars, while the black curve represents the leading principal component timeseries. Explained variance and correlation between indices are given in the legend in (b). (c) Same as (a) but for land SAT and 10-m level wind (arrows; based on JRA-55 for 1958-2019) anomalies. (d) Same as (a) but for precipitation anomalies (shading based on GPCC for 1958-2016 and contours based on CMAP for 1979-2019 for every 0.2 mm/day). On maps, no-overlay indicates regions where the regressions are significant based on t-test accounting for false detection rate at 10% and crosses indicates no significance. Significance for CMAP precipitation is materialized by red contours in (d). All fields have been linearly detrended prior to computation.

ACCEPTED VERSION SUBJECT TO FINAL EDITING

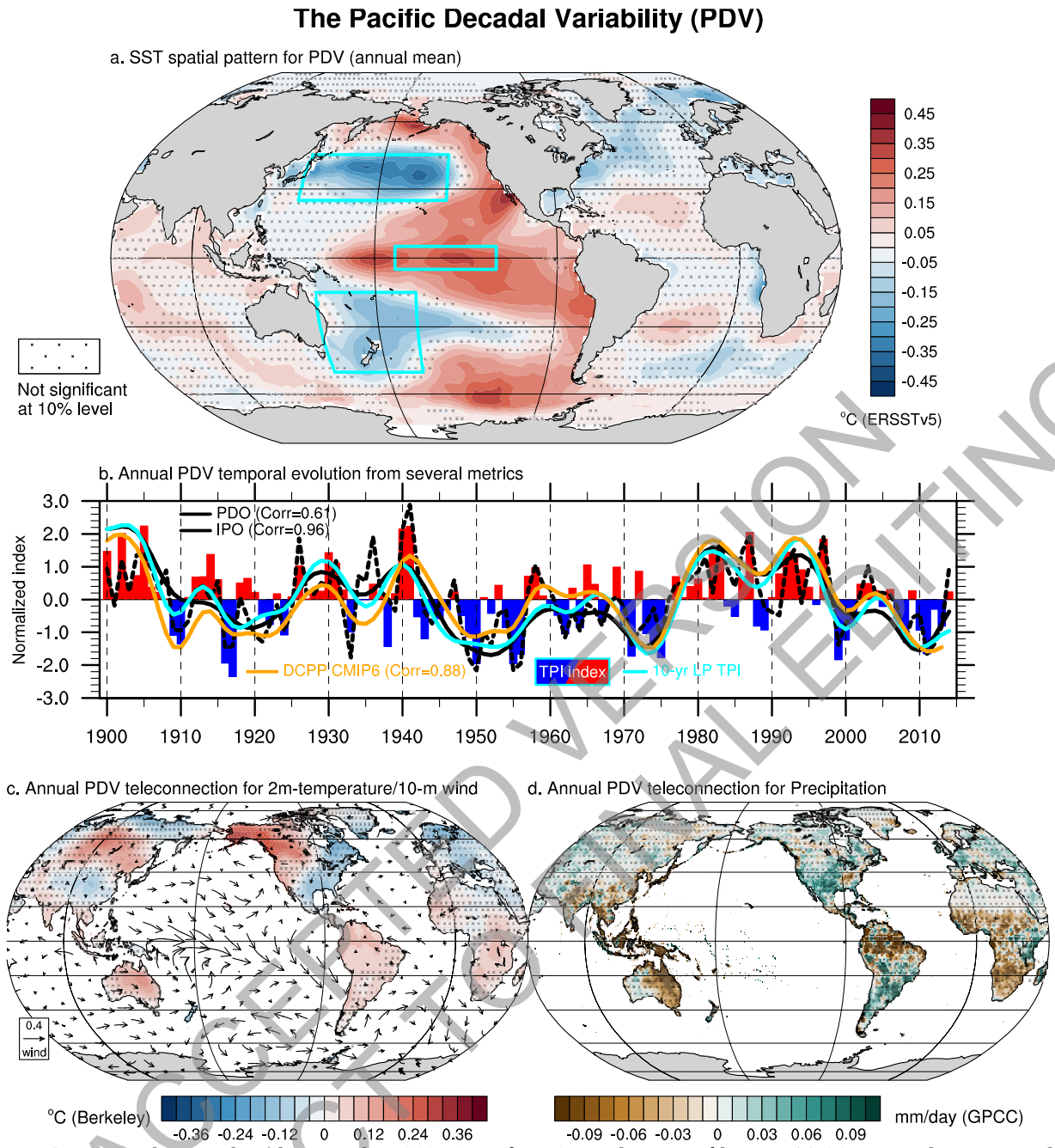

Figure AIV.8: The PDV based on TPI for 1900-2014 after 10-year low-pass filtering. (a) SST anomalies regressed onto TPI based on ERSSTv5. The cyan boxes indicate regions for the TPI definition. (b) Temporal evolution of the raw TPI (bars), the 10-year low-pass filtered TPI (cyan curve), the EOF-based PDO index (dashed black) and two estimations of the IPO EOF-based indices. In solid black, linear detrending is applied to annual data prior to the computation of the EOF of the low-pass filtered SST to remove the forced component in the SST field. In orange, the forced signal is estimated from CMIP5 historical simulations following Ting et al. (2009). The latter metric is used in CMIP6 DCPP-C sensitivity experiments (Boer et al. 2016). The correlation between the low-pass filtered TPI and all PDV indices is given in the legend. (c) Same as (a) but for land SAT (shading; based on BerkeleyEarth for 1900-2014) and 10-m level wind (arrows; based on JRA-55 for 1958-2014) anomalies. (d) Same as (a) but for precipitation anomalies (shading based on GPCC for 1900-2014). All are based on annual mean. On maps, no-overlay indicates regions where the regressions are significant based on t-test accounting for false detection rate at 10% and crosses indicates no significance.

ACCEPTED VERSION SUBJECT TO FINAL EDITING

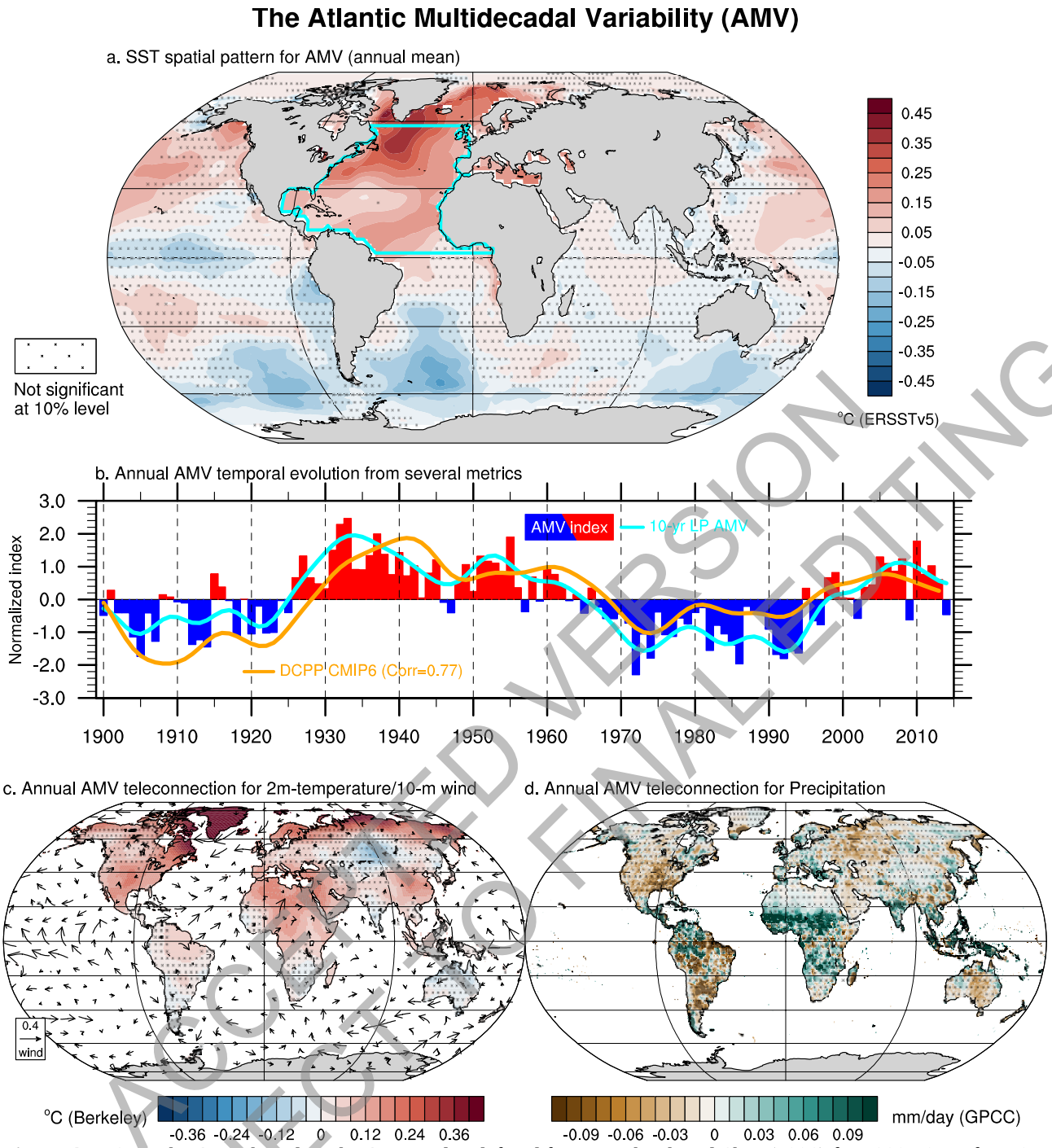

Figure AIV.9: The AMV based on the AMV index defined from Trenberth and Shea (2006) for 1900-2014 after 10-year low-pass filtering. The index corresponds to the annual SST averaged over the North Atlantic domain (cyan box) minus near-global average [60ºN-60ºS]. (a) SST anomalies regressed onto the AMV index based on ERSSTv5. (b) The cyan curve indicates the 10-year low-pass filtered AMV index shown in bars. The orange curve stands for the AMV index used for the CMIP6 DCPP-C sensitivity experiments (Boer et al. 2016). (c) Same as (a) but for land SAT (shading; based on BerkeleyEarth for 1900-2014) and 10-m level wind (arrows; based on JRA-55 for 1958-2014) anomalies. (d) Same as (a) but for precipitation anomalies (shading based on GPCC for 1900-2014). All is based on annual mean. On maps, no-overlay indicates regions where the regressions are significant based on t-test accounting for false detection rate at 10% and crosses indicates no significance.

ACCEPTED VERSION SUBJECT TO FINAL EDITING

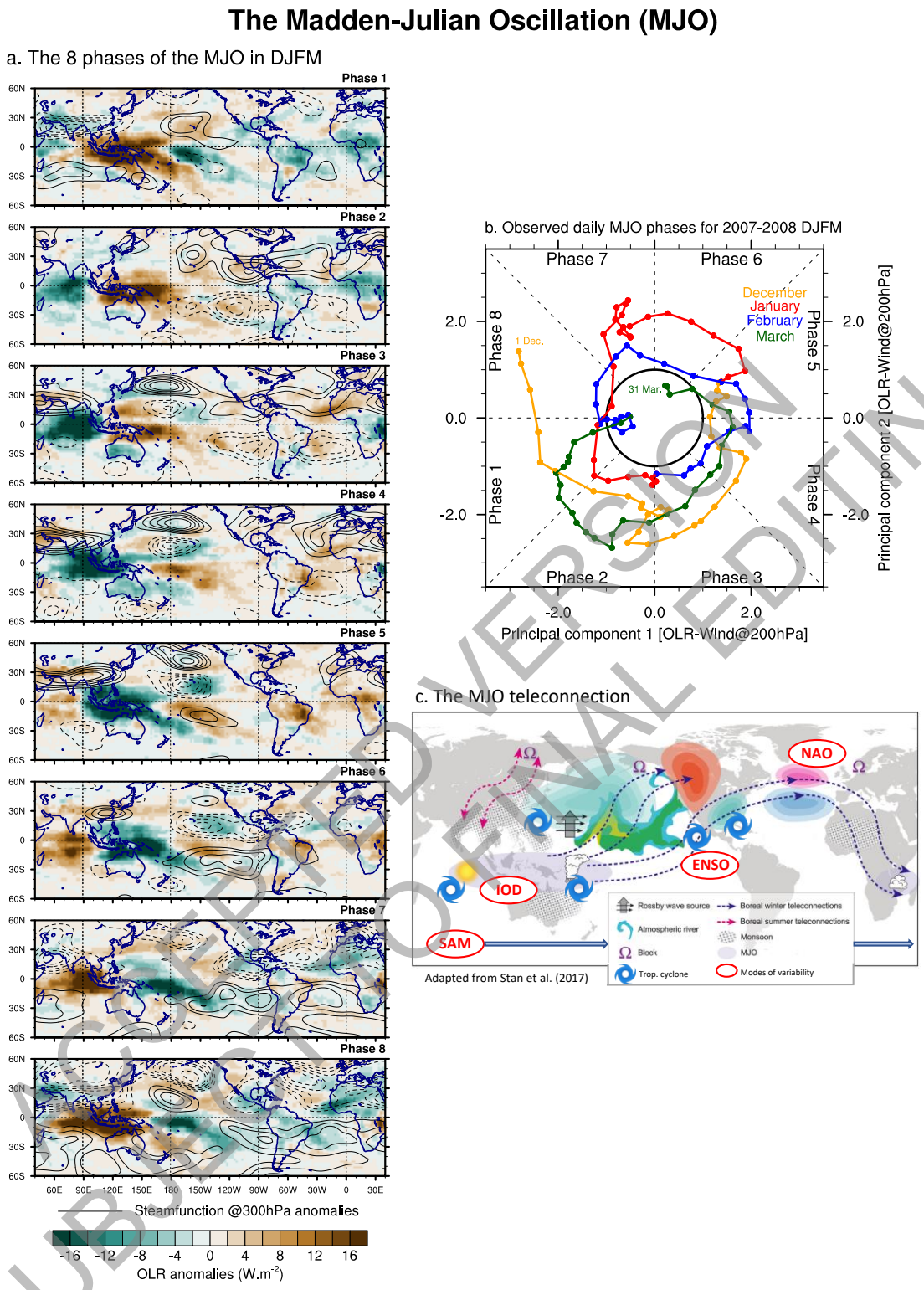

ACCEPTED VERSION SUBJECT TO FINAL EDITING

Figure AIV.10: (a) The spatio-temporal properties of the MJO. Daily composites of Outgoing Longwave Radiation (OLR, W m^{-2}, shaded) anomalies and streamfunction anomalies at 300 hPa (STF, contours every 0.5 10^6 m^2 s^{-1}) for the 8 MJO phases in boreal winter (1st Dec. -31st March) based on NOAA interpolated satellite products and NCEP-NCAR reanalyzes over 1979-2019, respectively. Greenish (brownish) colours indicate enhanced (reduced) convective activity associated with wet (dry) conditions. Solid

(dashed) contours show for positive (negative) STF anomalies which stand for anomalous anticyclonic circulation in the Northern (Southern) Hemisphere. (b) Phase diagram of the MJO constructed from the two leading principal components drawn from empirical orthogonal decomposition of combined wind@300hPa+OLR fields following Wheeler and Hendon (2004) for the winter 2007-2008 chosen as an example of active MJO years. (c) Schematic representation of MJO-related tropical—Northern Hemisphere interactions and teleconnections inferred from observational and numerical studies (adapted from Stan et al.(2017)). Because the interactions and teleconnections of the Southern Hemisphere are not as well understood but SAM, they are not included in the current schematic.

ACCEPTED VERSION SUBJECT TO FINAL EDITING